Thesis for the degree of Doctor of Philosophy

Chiral Effective Field Theory with Partly Perturbative Pions Applied to the Few-Nucleon Sector

Oliver Thim

Department of Physics and Astronomy
Chalmers University of Technology
Gothenburg, Sweden 2026

Chiral Effective Field Theory with Partly Perturbative Pions Applied to the Few-Nucleon Sector

Oliver Thim

ISBN 978-91-8103-434-9

Acknowledgements, dedications, and similar personal statements in this thesis, reflect the author's own views.

Doktorsavhandlingar vid Chalmers tekniska högskola
Ny serie nr 5891
ISSN 0346-718X
https://doi.org/10.63959/chalmers.dt/5891

Department of Physics and Astronomy
Chalmers University of Technology
SE-412 96 Gothenburg
Sweden
Telephone +46 (0)31-772 1000

This thesis has been prepared using LaTeX.

Cover: Artistic interpretation of the connection between high- and low-energy descriptions of the strong nuclear force facilitated by effective field theory interactions. (By Alma Blombäck)

Printed by Chalmers digitaltryck
Gothenburg, Sweden 2026

Chiral Effective Field Theory with Partly Perturbative Pions Applied to the Few-Nucleon Sector

Oliver Thim
Department of Physics and Astronomy
Chalmers University of Technology

Abstract

Chiral effective field theory (χEFT) provides a framework for deriving systematically improvable models of the strong nuclear interaction that are consistent with quantum chromodynamics (QCD). This enables first-principles predictions of nuclear properties relevant for studying the stability of visible matter and for precision tests of physics within and beyond the Standard Model. A power counting scheme facilitates the organization of interaction diagrams contributing to the nuclear force according to their importance. Most existing χEFT calculations of nuclear systems rely on Weinberg power counting; however, it has been shown that this approach yields observables that depend on the regulator cutoff. In this thesis, I investigate an alternative power counting scheme that is designed to produce cutoff-independent, i.e., renormalization-group invariant, observables. A key difference compared to Weinberg power counting is that all subleading parts of the interaction are treated perturbatively. I analyze the two-nucleon system by studying scattering observables as well as spin entanglement in connection with accidental symmetries. Low-energy theorems are also investigated as a consistency check for the partly perturbative treatment of pion exchanges. These studies are performed for a wide range of cutoffs, demonstrating cutoff independence in the two-nucleon system. Furthermore, I implement and validate numerical algorithms for perturbatively computing ground-state energies in light nuclei within the no-core shell model. A total of 33 low-energy constants are calibrated, and the constructed interactions are employed to predict ground-state properties of ^{2,3}H, ^{4}He, and ^{6}Li up to fourth order in the power counting. Accurate predictions are obtained for these light nuclei at low cutoffs ($\Lambda \approx 500$ MeV), where numerical convergence can reliably be achieved. The studied power counting can be used to construct nuclear interaction models that possess predictive power for few-nucleon systems. The inclusion of three-nucleon forces, the extension of the perturbative framework to other many-body methods, and further study of so-called exceptional cutoffs are important directions for future work.

Keywords: Nuclear forces, chiral effective field theory, power counting, few-nucleon systems.

List of Publications

This thesis is based on the work contained in the following papers:

I "Bayesian analysis of chiral effective field theory at leading order in a modified Weinberg power counting approach"
O. Thim, E. May, A. Ekström, and C. Forssén
Phys. Rev. C **108**, 054002 (2023)
Preprint: arXiv:2302.12624 [nucl-th]

II "Perturbative computations of neutron-proton scattering observables using renormalization-group invariant chiral effective field theory up to N^3LO"
O. Thim, A. Ekström, and C. Forssén
Phys. Rev. C **109**, 064001 (2024)
Preprint: arXiv:2402.15325 [nucl-th]

III "Low-Energy Theorems for Neutron–Proton Scattering in χEFT Using a Perturbative Power Counting"
O. Thim
Few Body Syst. **65**, 69 (2024)
Preprint: arXiv:2403.10292 [nucl-th]

IV "Perturbative χEFT calculations of the deuteron and triton up to N^2LO"
O. Thim, A. Ekström, and C. Forssén
Phys. Rev. C **112**, 064008 (2025)
Preprint: arXiv:2510.12207 [nucl-th]

V "Entanglement and accidental symmetries in the nucleon-nucleon system"
A. L. Cavallin, O. Thim, and C. Forssén
Phys. Rev. C **113**, 014005 (2026)
Preprint: arXiv:2510.09466 [nucl-th]

VI "Perturbative χEFT calculations of light nuclei up to N^3LO"
O. Thim, A. Ekström, and C. Forssén
Preprint: arXiv:2604.14985 [nucl-th]
(*under review*)

This thesis is also based on the following research software:

I "`nn-mwpc`" – An open-source research code for perturbatively computing nucleon-nucleon scattering observables.
O. Thim
License: GPLv3
https://github.com/othim/nn_mwpc

II "`py-ncsm`" – An open-source research code for perturbatively computing three-nucleon ground-state energies in the Jacobi no-core shell model.
O. Thim
License: GPLv3
https://github.com/othim/py-ncsm

In addition, the author has also been involved in the work leading to the following publications. These are not included in the thesis.

I "Effective field theory analysis of the Coulomb breakup of the one-neutron halo nucleus ^{19}C"
P. Capel, et al.
Eur. Phys. J. A **59**, 273 (2023)
Preprint: arXiv:2301.06444 [nucl-th]

II "Correlated effective field theory truncation errors: from nucleon-nucleon scattering amplitudes to observables"
L. I. G. B. Abrahamsson, O. Thim, A. Ekström, and C. Forssén
(*in manuscript*)

Statement of contributions

My contributions to the included papers were:

I I wrote the code to compute *np* scattering observables and analyzed the limit-cycle-like behavior. I also performed the Bayesian inference using MCMC and wrote the first draft of the manuscript, which I refined together with my co-authors.

II I contributed to the formulation of the project. I derived the formulas for implementing the distorted-wave perturbation series, and wrote and benchmarked the code. I produced and interpreted the results and wrote the manuscript together with my co-authors.

III I formulated the project, performed the computations, interpreted the results, and wrote the manuscript.

IV I contributed to formulating the project and implemented the Jacobi coordinate no-core shell model code used for the perturbative computations. I produced and analyzed the results and wrote the manuscript together with my co-authors.

V I formulated the original idea of the project and aided in benchmarking the nucleon-nucleon scattering computations. I contributed to derivations, interpretation of results, and to writing the manuscript.

VI I contributed to formulating the project. I performed the computations, analyzed the results, and wrote the manuscript together with my co-authors.

Acknowledgements

I want to take this opportunity to mention and thank the many people in my life, without whom my PhD journey would not have been possible.

First and foremost, I would like to extend my most sincere gratitude to my supervisor Andreas Ekström, and to my assistant supervisor, Christian Forssén. Thank you for all the guidance, support, and time you have devoted to me during these almost five years as a PhD student. It has been a pleasure to learn from you and to work together on many interesting research projects.

Additionally, I am grateful to my former and current colleagues at Chalmers, in particular, Sean, Isak, Weiguang, Alexandra, Håkan, Eleanor, Joanna, Alberto, Michal, Anna, Mavi, Taylor, Salma, Ida, Hirepan, Eli, Theresa, Hampus, Immo, Ulf, Martin, Gaute, and Daniel, for many helpful discussions and for providing an enjoyable workplace. A special thanks to Simone, Alma C, and Lucas for reading and spotting mistakes in a draft version of my thesis. I also want to thank my examiner, Gabriele, for always showing an interest in my work.

A big thanks to Chieh-Jen "Jerry" Yang, Bingwei Long, and Rui Peng, for many helpful conversations regarding their work. Your detailed answers have been valuable for the work in my thesis. I also want to thank all other physics colleagues that I have had the pleasure to interact with over the years at conferences, workshops, and schools. A special thanks to Harald and Nathan for an enjoyable collaboration.

From my time in high school, I want to specifically thank my eminent teacher and mentor, Stefan, for spurring my interest in programming and science. From my time as an undergraduate student at Chalmers, I want to mention and thank my friends Jack, Rickard, Fredrik, and my long-time friend and PhD-office-neighbor, Eric.

Last but not least, to all my friends and family: thank you for always being there for me, and for providing warmth and joy. Alma, if it were not for you, I would not be complete. Thank you for standing beside me every day.

Oliver Thim
Göteborg, May 2026

List of acronyms

Symbols

χEFT	chiral effective field theory
χPT	chiral perturbation theory
πN	pion-nucleon
nn	neutron-neutron
np	neutron-proton

C

c.m.	center of mass
CIB	charge-independence breaking

E

EFT	effective field theory
ERE	effective range expansion

F

FD	finite-difference

H

HO	harmonic oscillator

J

J-NCSM	Jacobi-coordinate NCSM

L

LECs	low-energy constants
LETs	low-energy theorems
LO	leading order
LS	Lippmann-Schwinger

M

M-NCSM	M-scheme NCSM
MCMC	Markov chain Monte Carlo

N

NCSM	no-core shell model
NN	nucleon-nucleon

O

OPE	one-pion exchange

P

PC	power counting
pdf	probability density function

Q

QCD	quantum chromodynamics

R

RG	renormalization group

W

WPC	Weinberg power counting

Contents

Chapter 1

Introduction

Neutrons and protons account for more than 99% of the visible matter in our universe. A large fraction of these particles is bound in atomic nuclei by the strong nuclear force. Advancing our understanding of the emergent many-body dynamics of nuclei, as well as their interactions with surrounding matter and fields, remains at the frontier of modern physics research. A quantitative understanding of nuclei and their properties is essential for both basic and applied sciences, ranging from astrophysics and particle physics to medical physics. The work in this thesis focuses on developing and analyzing first-principles models of the strong nuclear force based on the fundamental theory of quantum chromodynamics (QCD), and using these models to predict properties of nuclei.

A quantum system of neutrons and protons, collectively referred to as nucleons, is governed by the Schrödinger equation

$$\hat{H} \left|\Psi\right\rangle = i\hbar \frac{\partial}{\partial t} \left|\Psi\right\rangle \tag{1.1}$$

where $\left|\Psi\right\rangle$ is the wave function of the quantum state, $\hat{H}$ is the Hamiltonian operator consisting of the kinetic- and potential-energy operators, and $\hbar$ is the reduced Planck constant. Determining the quantum state $\left|\Psi\right\rangle$ requires two key ingredients: a potential model describing the nuclear interaction, and a method for solving the Schrödinger equation. In the first part of this thesis, we will study how to construct potential models for the nuclear interaction from first principles. We will then use these potentials to study and predict observable quantities in nuclei consisting of up to $A = 6$ nucleons by solving Eq. (1.1) in its time-independent formulation for both bound and scattering states.

Before delving into the details, we will take a step back and look at how the nuclear interaction has been modeled historically, and what ideas have led up to the present descriptions. Modeling the atomic nucleus began with its discovery by Rutherford in 1911 [1]. Following Chadwick's discovery of the

neutron in 1932 [2], it was suggested that both the proton and the neutron were fundamental constituents of nuclei. The coexistence of neutrons and electrically charged protons in the nucleus prompted the compelling assumption that some attractive force, albeit unknown at the time, must act between them — the nuclear force.

From known experimental data on binding energies of a variety of nuclei, Wigner [3] inferred that the nuclear force must be of relatively short range, and rather strong within that range. In 1935, Yukawa [4] proposed that a new elementary particle could be responsible for mediating this strong interaction. This particle was suggested to have a mass somewhere in between that of the electron and the proton. Since 1947 we have known this particle as the pion (π), and it indeed plays an important role in understanding the strong nuclear force.

It was soon understood that the nuclear force carried a complicated structure compared to the other known forces at the time. Building on the ideas of Yukawa, meson-exchange models were constructed. In these models, the nuclear force is described by the exchange of pions, as well as heavier mesons, which impart different force characteristics. Following the progress of nucleon-nucleon (NN) scattering experiments and the development of effective range theory by Bethe [5], more could be learned about the structure of the nuclear force. Despite the phenomenological success of meson-exchange models, a solid theoretical understanding was still lacking.

A deeper theoretical understanding of the strong nuclear force emerged in the 1960s and 1970s with the formulation of QCD [6–8], in which both nucleons and mesons can be described as composite particles of more fundamental constituents, quarks. Following the discovery of QCD, efforts to understand how the strong force between composite particles emerges from quark-level interactions began. Developing this understanding is challenging because QCD is highly non-perturbative in the low-energy regime relevant to nuclear physics.

A breakthrough came when Weinberg applied the ideas of effective field theory (EFT) to model the nuclear force [9–11]. Even though the underlying theory, QCD, describes interactions among quarks and gluons, a low-energy effective theory can be formulated in terms of the effective degrees of freedom — in this case, nucleons and pions. As dictated by the so-called *folk theorem* [9], the dynamics of the effective degrees of freedom is described by the most general effective Lagrangian consistent with the underlying symmetries of QCD. Besides the spacetime symmetries, the approximate chiral symmetry of low-energy QCD plays an important role in constraining pion-nucleon (πN) interactions, since the pion can be described as a pseudo Nambu-Goldstone boson of the spontaneously (and explicitly) broken chiral symmetry.

The EFT principles can be applied to construct an effective Lagrangian that contains an infinite number of pion-pion, πN, and nucleon-contact interaction terms. To achieve predictive power, the emerging interactions must be sys-

tematically truncated, using some principle to assess their relative importance. This kind of organizational principle is known as power counting (PC). Since the EFT is a low-energy effective description of QCD, it is expected to be accurate below a certain momentum scale, referred to as the breakdown scale (Λ_b). The exact value of the breakdown scale is a priori unknown. However, it can be estimated to be of the order where effects from neglected degrees of freedom become important, such as heavier mesons, e.g., the $\rho(770)$, or the $\Delta(1232)$ nucleon excitation.

The Feynman diagrams describing the πN interactions in the EFT can be assigned a scaling $(Q/\Lambda_b)^\nu$, where Q denotes the low-energy scale of interest. In the case of NN scattering, Q is the modulus of the center of mass (c.m.) external momenta. The chiral orders $\nu = 0, 1, 2, ...$ will be denoted as leading order (LO), next-to-leading order (NLO), next-to-next-to-leading order ($\mathrm{N^2LO}$) and so on. Crucially, the success of the EFT framework relies on sufficient separation between the low-energy scales and the breakdown scale. Consequently, the EFT is only expected to accurately describe low-energy phenomena.

Following Weinberg's EFT idea, Gasser et al. [12, 13] worked out pion-pion and πN scattering in perturbation theory up to one loop. This EFT, including at most one nucleon, is referred to as chiral perturbation theory (χPT) and has enjoyed great success in the past decades, see, e.g., Ref. [14]. In the multi-nucleon sector, the EFT is referred to as chiral effective field theory (χEFT), where the theoretical description is more challenging due to the non-perturbative nature of the NN force, a feature that leads to shallow bound and virtual states. Weinberg [10, 11] proposed a scheme to calculate nuclear amplitudes in χEFT by perturbatively calculating two- or many-nucleon potentials from the πN interactions described in χPT, followed by iterating the potentials in the Schrödinger equation to generate the non-perturbative phenomena. This approach is referred to as Weinberg power counting (WPC) and will be described in more detail in Chapter 2.

Ordonez et al. [15–17] applied WPC to derive two- and three-nucleon potentials up to $(Q/\Lambda_b)^3$ in time-ordered perturbation theory in the early '90s. These works started the era of constructing quantitative nuclear forces from χEFT. Kaiser et al. [18–22] applied covariant perturbation theory and dimensional regularization to study NN amplitudes up to $(Q/\Lambda_b)^3$, and also worked out higher-order loop corrections. Epelbaum et al. [23–25] constructed NN potentials with the method of unitary transformations up to $(Q/\Lambda_b)^4$. Furthermore, Epelbaum et al. [26] also performed computations that include three-nucleon forces, which arise naturally in χEFT. The unified description of two- and many-nucleon forces together with interaction currents is one of the great strengths of χEFT. In 2003, Entem et al. [27] constructed potentials up to $(Q/\Lambda_b)^4$ and demonstrated that NN forces from χEFT can reach comparable precision to earlier phenomenological models [28, 29].

Although χEFT strongly constrains interactions through symmetries, the

strength of the interaction terms is parameterized by so-called low-energy constants (LECs) whose values are a priori undetermined. The LECs can be calibrated using experimental πN and NN scattering data, or with other relevant observables [27, 30–33]. A key advantage of an EFT model is that theoretical uncertainties due to truncation of the EFT expansion emerge naturally, and can be estimated from the expansion in $(Q/\Lambda_b)^\nu$. Early progress to utilize this in the calibration of LECs was made in Refs. [34–36]. In the past decade, Bayesian inference methods have been increasingly employed for calibrating the LECs in WPC-based χEFT interactions [35, 37–44]. The probabilistic interpretation of uncertainties in the Bayesian framework is well-suited for systematically incorporating experimental and EFT uncertainties as well as prior information. An appropriate modeling of uncertainties is vital for enabling precision studies of nuclear observables from first principles.

To date, WPC is the dominant approach to construct two- and three-nucleon forces, where NN interactions up to fifth order have been constructed $(Q/\Lambda_b)^5$ [45, 46]. Combining χEFT with many-body methods to solve the Schrödinger equation, such as the no-core shell model (NCSM) [47], coupled cluster [48], many-body perturbation theory [49], or lattice EFT [50] has over the last decades enabled first-principles (*ab initio*) studies of nuclei [51, 52]. *Ab initio* computations have gradually advanced to heavier systems and more complex observables [53–58]. As a specific example, the neutron skin thickness of heavy nuclei is linked to the structure and size of neutron stars via the neutron-matter equation of state [59–61]. This means that predictions in finite nuclei provide a controlled link between astrophysical observables and the microscopic description of the nuclear force [57, 62, 63]. Precision calculations of nuclear observables are also important for studying fundamental symmetries and physics beyond the Standard Model. One example is the study of the unitarity of the Cabibbo-Kobayashi-Maskawa quark mixing matrix, which requires electroweak radiative corrections from nuclear theory [64–66]. Another is neutrinoless double beta decay, which is a hypothetical radioactive process that, if observed, would be a first signal of lepton number violation, and have implications for the observed matter-antimatter asymmetry in the universe [67, 68].

An essential ingredient in all *ab initio* studies is the model for the nuclear interaction, for which χEFT based on WPC is almost exclusively employed. However, theoretical investigations of WPC have shown that the amplitudes are not renormalized order by order [69–71]. This means that the physical predictions depend on the specific regularization procedure used to separate short- and long-range physics in the process of renormalization. This violation of renormalization group (RG) invariance has thus motivated the exploration of modified PC schemes constructed to satisfy RG invariance [72].

Insights from pionless EFT [73, 74], where only nucleons are considered as degrees of freedom, led Kaplan et al. [75, 76] to propose a PC for χEFT where effects from pions are included perturbatively, which removes the renormaliza-

tion problems. However, this scheme did not improve the range of convergence in momenta beyond what was achievable in pionless EFT [77] while also showing inconsistencies in so-called low-energy theorems (LETs) [78, 79].

The renormalization issues in χEFT can be traced to the singular short-distance behavior of the pion-exchange contributions to the NN potential [80, 81]. However, singular potentials can still produce RG-invariant amplitudes provided that divergence-absorbing counterterms are included [70]. The centrifugal barrier guarantees that these counterterms are only needed for partial waves with angular momentum quantum number $\ell < \ell_c$, for $\ell_c \approx 2$ [82, 83]. The increased singularity of higher-order pion-exchanges can be successfully tamed by treating all subleading interactions perturbatively, as shown by Long and van Kolck [84]. Based on these findings, several modifications of WPC have been proposed and studied [71, 83, 85–93]. For recent overviews see Refs. [72, 94]. However, there is still a discussion in the literature on how renormalization should be performed in χEFT, and whether or not cutoffs well beyond the breakdown scale should be considered, see, e.g., Refs. [83, 87, 95–102].

Nogga et al. [70] proposed to modify the PC by Kaplan et al. and treat pions perturbatively only in partial waves with $\ell \geq \ell_c$. They argue that the one-pion exchange (OPE) interaction is strong enough to warrant a non-perturbative treatment only in the lowest-ℓ partial waves. This approach of including pions *partly perturbatively* was further developed by Long and Yang in Refs. [90–92]. They analyzed partial-wave amplitudes in detail to determine at which order certain counterterms with associated LECs should appear to retain RG invariance at each chiral order. They computed neutron-proton (np) scattering phase shifts up to N^{3}LO in selected channels, and demonstrated an adequate and RG-invariant description of empirical scattering phase shifts [103]. With the development of this new PC, the perturbative investigations of NN scattering initiated in Ref. [83] were further extended in Refs. [82, 104] to include higher-order NN potentials from χEFT. This PC by Long and Yang exists in a few different flavors depending on the choice of ℓ_c and how subleading pion exchanges are treated for $\ell \geq \ell_c$. The specific construction that is employed in this thesis will be described in detail in Chapter 3. It is interesting to see how the role and understanding of the pion in the nuclear interaction have evolved. It was first proposed as a hypothetical particle by Yukawa, later reborn as a pseudo Nambu-Goldstone boson of the spontaneously broken chiral symmetry and, in the PC investigated in this thesis, reshaped with its partly perturbative treatment.

Previous studies of PCs with partly perturbative pions have only investigated a limited set of nuclear observables. Besides np phase shifts, Song et al. [105] studied ^{3}H up to NLO, and Yang et al. [106] studied ground-state energies for ^{3}H, ^{3,4}He, ^{6}Li and ^{16}O up to NLO. The observed under-binding rendered ^{16}O prone to decay to four α-particles, and ^{6}Li to an α-particle plus a deuteron. Overfitting in the employed NN interaction, and the lack of many-nucleon forces

[107] were discussed as two possible culprits.

The extent to which modified PC schemes, such as the Long and Yang PC with partly perturbative pions, can achieve the predictive power required for nuclear structure and reaction studies remains largely untested. A systematic analysis of nuclei based on an RG-invariant power counting scheme will deepen our understanding of the nuclear force and reinforce its connection to QCD. The aim of this thesis is to study the predictive power of a version of the Long and Yang PC by:

(i) Constructing interactions with partly perturbative pions up to chiral order N^3LO.

(ii) Developing frameworks for perturbative computations of nuclear observables up to N^3LO in both NN and few-nucleon systems.

We limit the studies to consider only two-nucleon forces, and also neglect Coulomb interactions. Isospin breaking in the nuclear force will for the most part also be neglected, except for the study in Paper III.

The thesis is organized as follows. In Chapter 2, the essential elements of EFTs are introduced, and it is demonstrated how to construct NN interaction potentials from χEFT. The specific PC with partly perturbative pions that is studied in this thesis is introduced in Chapter 3, together with its theoretical underpinnings. This PC is used in all works contained in this thesis, except for Paper V. Papers I – III present studies of the NN system in this PC, and their results are summarized in Chapter 3. Chapter 4 presents the results from Paper V, where we study the connection between Wigner SU(4) symmetry and spin entanglement in NN scattering and discuss possible implications for PCs. Chapter 5 presents the application of our version of the PC with partly perturbative pions in computations of light nuclei, and the results of Papers IV and VI are summarized. Finally, in Chapter 6 the results and conclusions of the thesis are summarized, and various directions of further research are outlined.

Key outcomes

This thesis is based on six papers (I – VI), and the key outcomes of these are listed below.

Paper I: We use Bayesian inference to determine the values of the LECs at LO in our PC and demonstrate a robust inference across a wide range of cutoffs. By taking experimental and EFT uncertainties into account, we obtain a LO interaction that is substantially different from interactions where the LECs are calibrated using phase shifts. This confirm the suspected fine-tuning of LECs discussed in Ref. [106].

Paper II: In this study, we predict *np* scattering observables up to N^{3}LO, where all subleading interactions are treated strictly perturbatively. We demonstrate accurate predictions for *np* scattering observables for a wide range of momentum cutoffs. The implementation in this study enabled the first study of scattering observables beyond NLO in this type of PC with partly perturbative pions.

Paper III: In this paper, I study the LETs for effective range parameters in our PC with partly perturbative pions. An excellent agreement of LETs in S-wave channels is demonstrated, where the mass difference between charged and neutral pions was important to incorporate in the OPE potential in the spin-singlet channel. The results in this study provide a consistency check for the partly perturbative treatment of pion exchanges in this PC.

Paper IV: We extend the studies of the PC with partly perturbative pions to N^{2}LO for ^{3}H and demonstrate the first perturbative computation to this order within the NCSM. We encounter divergences in predicted observables at exceptional values of the cutoff, previously only studied in the NN system. We partly demonstrate how these divergences can be tamed.

Paper V: In this paper, we study symmetries in the nuclear interaction, and in particular the emergent Wigner SU(4) symmetry. We employ realistic NN potentials to quantify the connection between SU(4) symmetry spin entanglement suppression in NN scattering. Our results advance the understanding of the effects of symmetries in the nuclear interaction and can provide valuable guidance for developing symmetry-guided PC schemes.

Paper VI: We employ the PC with partly perturbative pions to predict ground-state energies of ^{3}H, ^{4}He, and ^{6}Li up to N^{3}LO by performing perturbative computations within the NCSM. We present results for interactions calibrated to both *np* phase shifts and ^{2,3}H binding energies. This study demonstrates that it is possible to obtain quantitatively accurate predictions for light nuclei up to ^{6}Li in our employed PC.

Chapter 2

Nuclear forces from chiral effective field theory

This chapter introduces how to construct models of the strong nuclear force using EFTs. We first review the key principles of an EFT, which is then used to establish a connection between the nuclear force and the underlying theory of strong interactions, QCD. We then specifically show how to construct nuclear forces from χEFT using WPC. There are known problems regarding renormalizability that arise in this framework. Possible solutions to this using modified PC schemes will be the subject of Chapter 3. Natural units in which $\hbar = c = 1$ will be used in this chapter and throughout the thesis.

2.1 What is an effective field theory?

The EFT approach rests on the principle that details of high-energy dynamics should not affect observables at much lower energies. This principle has implicitly been used throughout history to model physical phenomena without knowledge of the underlying processes at higher-energy scales. The goal of an EFT is thus to describe the general dynamics among low-energy degrees of freedom in a way that is consistent with an underlying (possibly unknown) theory [9, 108, 109].

The highly successful Standard Model of particle physics describes the known constituents of matter to an astounding precision [110, 111]. However, there are still several unsolved questions regarding neutrino masses, the strong CP problem, and the nature of dark matter — to name a few [112, 113]. The modern view is that the Standard Model should be interpreted as an EFT, where the energy scale Λ_{SM} associated with new physics, described by non-renormalizable interactions, is much larger than the energy scale at which the theory has been

tested. In fact, from the precision achieved by current experimental and theoretical calculations, one can estimate the scale $\Lambda_{\rm SM}$ [114], since the couplings of the suppressed non-renormalizable interactions are expected to take the form $c_n \Lambda_{\rm SM}^{4-n}$ with dimensionless c_n and $n > 4$ [115]. When probing a physical process at a characteristic momentum scale $p \ll \Lambda_{\rm SM}$, a non-renormalizable interaction will introduce a factor $\propto \Lambda_{\rm SM}^{4-n}$. On dimensional grounds, this factor needs to be accompanied by p^{n-4}, which leads to a suppression $(p/\Lambda_{\rm SM})^{n-4} \ll 1$. This argument can be made more precise in the language of quantum field theory, where high-energy degrees of freedom can be explicitly eliminated (integrated out) [108].

As a more concrete example, Fermi's theory of weak interactions [116] can be seen as an EFT of the Standard Model below the mass scale of the $W^{\pm}$ ($m_W \approx 80$ GeV) and Z^0 ($m_Z \approx 91$ GeV) bosons. The amplitude describing β-decay involves an exchange of a W-boson where typical momentum transfers are limited to a few tens of MeV [110], and therefore much less than m_W [117]. This small momentum transfer implies that the exchanged W-boson must be highly virtual and thus short-lived. The short lifetime means that the interaction approximately appears local, which can be made formal by expanding the Feynman propagator entering the amplitude as $(q^2 - m_W^2)^{-1} = -m_W^{-2} + \mathcal{O}(q^2/m_W^2)$, where q^μ is the four-momentum transfer. The effect of $W^{\pm}$ exchange at low energies will, to first order, appear as a four-fermion contact interaction, with a coupling $G_F \propto m_W^{-2}$, which is recognized as the Fermi interaction with G_F being the Fermi constant. The physical picture to have in mind is that processes at high-energy scales can be approximated with local interactions at low energies.

One key aspect to highlight is that recasting Fermi's theory as an EFT enables an estimate of the truncation error relative to the full Standard Model amplitude, since the leading omitted terms are parametrically of order $\mathcal{O}(q^2/m_W^2)$. This type of error estimate is, of course, particularly useful when the underlying theory is not known, *but* a systematic EFT expansion can be constructed. This is the case in the coming sections when we describe the low-energy dynamics of hadrons using an EFT of QCD.

2.2 Chiral effective field theory — a bridge from quarks to nucleons

We seek to describe properties of atomic nuclei starting from the underlying theory of the strong interaction, QCD, which governs the dynamics of quarks and gluons. The non-Abelian nature of QCD gives that its interaction strength, α_S, weakens when probed at high-energy scales, which enables the use of perturbation theory. This is known as asymptotic freedom [6]. On the contrary, the interaction becomes stronger and highly non-perturbative in the low-energy regime ($\sim$ MeV) relevant to nuclear physics, which is manifested by the confine-

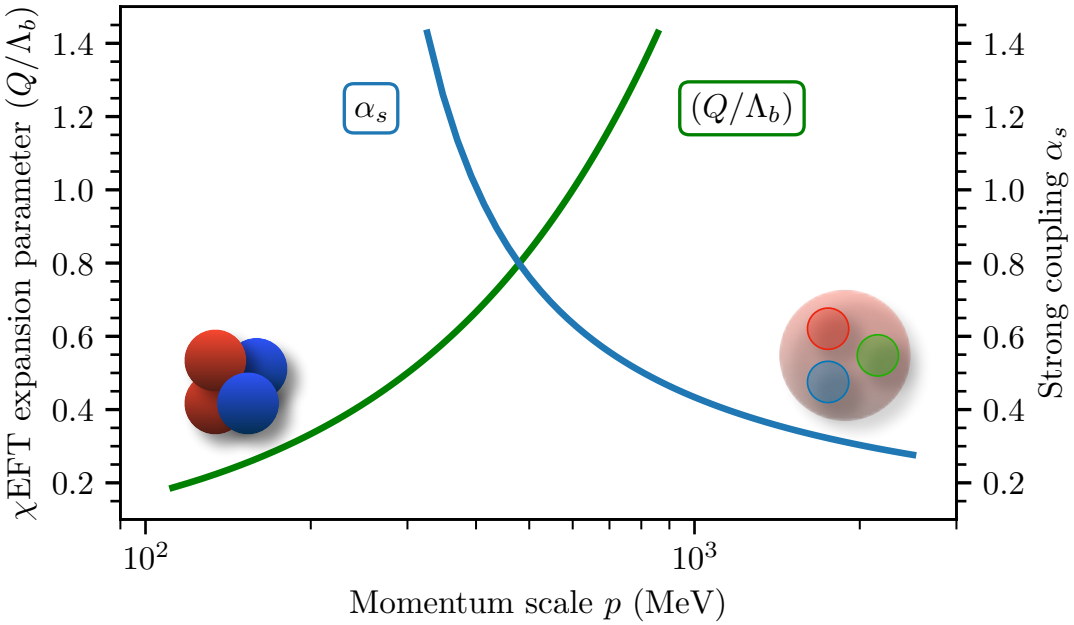

Figure 2.1: Illustration of momentum regimes where QCD and χEFT are perturbative. The blue line shows the approximate running of the strong coupling, α_s, revealing a non-perturbative behavior at low energies [122]. The χEFT expansion parameter (Q/Λ_b) shown in green is, on the contrary, small in the low-energy regime relevant to nuclear physics. Here, $\Lambda_b = 600$ in accordance with a recent analysis [39].

ment of quarks and gluons into hadrons. To study this regime, non-perturbative numerical techniques must be applied. Lattice QCD is one such example where the quark and gluon fields are discretized on an Euclidean space-time lattice [118]. Several successful studies of hadron masses and coupling constants have been made, see, e.g., Refs. [119–121]. However, the high computational complexity and the challenging fermionic sign problem make large-scale lattice simulations exceedingly challenging. Thus, starting from quarks and gluons as degrees of freedom does not currently present a practical avenue to analyze the properties of atomic nuclei.

Another approach to tackling the non-perturbative nature of QCD is by constructing an EFT which utilizes an effective (approximate) low-energy description in terms of effective degrees of freedom, trading quarks and gluons for nucleons and pions while neglecting heavier known mesons such as the ρ meson ($m_\rho \sim 770$ MeV) and nucleon excitations such as the $\Delta(1232)$.[1] As a result, the EFT is only expected to be accurate for energies where the effects of neglected degrees of freedom can be represented as local, which naturally introduces a scale $\Lambda_b \sim 1$ GeV where the effective description breaks down. The

[1]The $\Delta(1232)$ isobar can also be included in the EFT description [123], but will not be considered in this work.

EFT description remains connected to QCD by incorporating its low-energy symmetries [9], which will be discussed more in the coming sections. Beyond the space-time symmetries, the approximate chiral symmetry plays a particularly important role. This symmetry guarantees an expansion of the emerging πN interactions in the low-energy scale, Q, set by the external momentum and pion mass $Q \sim p,\ m_\pi$.

The advantage of shifting to an EFT description for the low-energy regime of QCD is illustrated in Fig. 2.1. The strong coupling constant, α_s, governs where QCD can be treated perturbatively, namely when $\alpha_s \ll 1$, which is fulfilled in the high-energy regime $p \gtrsim 1$ GeV. This regime is relevant in, for example, high-energy accelerator experiments probing the quark-structure of hadrons [122]. On the contrary, an EFT description of interactions among hadrons is organized in powers of Q/Λ_b, and a systematic expansion of πN interactions is possible in the low-energy ($\sim$ MeV) regime relevant to nuclear physics. In the meson and single-baryon sector, this is known as χPT [12, 13], which is one of the prime examples of a successful EFT. The extension of χPT to the many-nucleon sector is known as χEFT [10, 11]. This EFT lays the foundation for systematically improvable descriptions of nuclear observables according to the expansion

$$\mathcal{O} = \sum_{n=0}^{\infty} \mathcal{O}_n \left(\frac{Q}{\Lambda_b}\right)^n, \tag{2.1}$$

that are rooted in QCD and enable quantitative studies of atomic nuclei. In the following sections, the foundations of χEFT are presented, starting from the approximate chiral symmetry of QCD.

2.2.1 Low-energy QCD and chiral symmetry

The Lagrangian of QCD is obtained from the free-quark Lagrangian by applying the principle of gauge invariance with respect to the color gauge group $\mathrm{SU}(3)_c$ and reads[2] [122]

$$\mathcal{L}_{\mathrm{QCD}} = \bar{q} i \not{D} q - \frac{1}{4} \mathcal{G}^a_{\mu\nu} \mathcal{G}_a^{\mu\nu} - \bar{q} \mathcal{M} q. \tag{2.2}$$

The quark Dirac fields for N_f flavors are denoted q, and $\mathcal{G}^a_{\mu\nu}$ is the gluon field strength tensor. The gauge covariant derivative associated with the gluon fields A^a_μ reads $D_\mu = \partial_\mu - i g A^a_\mu \lambda_a/2$, for coupling constant g, and $\mathrm{SU}(3)_c$ generators $\lambda_a/2$ [122]. The Lagrangian for massless quarks is given by the first two terms in Eq. (2.2), and $-\bar{q}\mathcal{M}q$ is the mass term, with mass matrix $\mathcal{M}$. The quark masses follow a clear hierarchy $\{m_u, m_d, m_s\} \ll 1\ \mathrm{GeV} \leq \{m_c, m_b, m_t\}$, where

[2] The so-called θ-term is also allowed by the space-time and gauge symmetries and would explicitly induce strong P and CP violation (related to the strong CP problem). It is excluded from our discussion. We also exclude possible gauge-fixing terms, and ghosts needed for quantization [122, 124].

the GeV scale is associated with the lightest hadrons (excluding the pions), which we will come back to shortly.

The division of the QCD Lagrangian into its massless and massive parts will become apparent when we consider the chiral left- and right-handed quark fields $q_L = P_L q$ and $q_R = P_R q$, for chiral projectors $P_L = (1 - \gamma_5)/2$ and $P_R = (1+\gamma_5)/2$, respectively. The quark field can be decomposed into left- and right-handed parts $q = q_L + q_R$, and the QCD Lagrangian reads

$$\mathcal{L}_{\text{QCD}} = \left[\bar{q}_R i \not{D} \bar{q}_R + \bar{q}_L i \not{D} \bar{q}_L - \frac{1}{4}\mathcal{G}^a_{\mu\nu}\mathcal{G}^{\mu\nu}_a\right] + \left[- \bar{q}_L \mathcal{M} q_R - \bar{q}_R \mathcal{M} q_L\right]. \quad (2.3)$$

The Lagrangian for massless quarks enjoys a global symmetry under the flavor rotations

$$\text{SU}(N_f)_L \times \text{SU}(N_f)_R \times \text{U}(1)_V \times \text{U}(1)_A, \quad (2.4)$$

where $\text{U}(1)_V$ corresponds to baryon number conservation, while $\text{U}(1)_A$ is broken at the quantum level by the axial anomaly [125]. We focus on the remaining chiral symmetry, and we also restrict the discussion to the two-flavor case[3] ($N_f = 2$), only considering u and d quarks, since we are only interested in low-energy properties of QCD. The transformations of the left- and right-handed fields under the chiral $\text{SU}(2)_L \times \text{SU}(2)_R$ symmetry are

$$q_L = \begin{pmatrix} u_L \\ d_L \end{pmatrix} \mapsto \exp\Big(-i\alpha^a_L \frac{\tau_a}{2}\Big) \begin{pmatrix} u_L \\ d_L \end{pmatrix}, \quad q_R = \begin{pmatrix} u_R \\ d_R \end{pmatrix} \mapsto \exp\Big(-i\alpha^a_R \frac{\tau_a}{2}\Big) \begin{pmatrix} u_R \\ d_R \end{pmatrix}, \quad (2.5)$$

where τ_a denotes the Pauli matrices. An alternative parameterization of the chiral symmetry group can be obtained by considering either $\alpha^a_L = \alpha^a_R$ or $\alpha^a_L = -\alpha^a_R$ in Eq. (2.5), corresponding to the vector and axial rotations $\text{SU}(2)_V \times \text{SU}(2)_A$, respectively. Here, $\text{SU}(2)_V$ is the well-known isospin symmetry. Note, however, that the mass term in Eq. (2.3) explicitly breaks the chiral symmetry by the mixing of left- and right-handed fields.

Noether's theorem [126, 127] states that global symmetries correspond to conserved currents and charges. An expected consequence of chiral symmetry is that the hadron states form degenerate multiplets of opposite parity, so-called parity doubling [128]. A crucial assumption for arriving at this conclusion is that the conserved charges associated with $\text{SU}(2)_A$ annihilate the vacuum, meaning that chiral symmetry is realized in a so-called Wigner-Weyl mode. Parity doubling is not observed in nature, which leads to the natural conclusion that the $\text{SU}(2)_A$ symmetry is not realized in the ground state of the quantized theory. This means that the symmetry is spontaneously broken [128], and realized as a Nambu-Goldstone mode. Goldstone's theorem [129] states that each generator of $\text{SU}(2)_A$ which does not annihilate the vacuum will give rise to

[3] More general treatments also include strangeness (the s quark), see, e.g., Ref. [14].

a massless scalar field, a *Goldstone boson*, whose symmetries are inherited from the broken generator. In particular, the Goldstone bosons of the spontaneously broken axial group are expected to be $N_f^2 - 1$ massless pseudo-scalar fields.

There are no known massless bosons that fit this description in nature, but there are *massive* pseudo-scalar bosons; the pions (π^0, π^-, π^+), which are light ($m_\pi \approx 140$ MeV) compared to typical hadron masses of ~ 1 GeV. The non-zero pion masses can be understood as the result of the quark mass term in Eq. (2.3), which explicitly breaks chiral symmetry. The two-flavor mass matrix can be expressed as

$$\mathcal{M} = \begin{pmatrix} m_u & 0 \\ 0 & m_d \end{pmatrix} = \frac{1}{2}\left(m_u + m_d\right)\mathbb{1} + \frac{1}{2}\left(m_u - m_d\right)\tau_3, \tag{2.6}$$

where $m_u \approx 2.5$ MeV, $m_d \approx 5$ MeV, and $\mathbb{1}$ is the identity. We note that the mass term $-\bar{q}\mathcal{M}q$ is invariant under $\mathrm{SU}(2)_V$ (isospin symmetry) if $m_u = m_d$, where a small explicit isospin breaking is caused by the mass difference $m_u - m_d \ll 1$ GeV. To first order, the three pions have the same mass, which is linear in the quark masses and does not break isospin symmetry $m_\pi^2 = -(m_u + m_d)\langle \bar{u}u \rangle / f_\pi^2$. The mass is also proportional to the scalar quark condensate, and $f_\pi = 92.1$ MeV is the pion decay constant [130].

We have seen that chiral symmetry is an approximate symmetry of low-energy QCD, which is both spontaneously and explicitly broken. This has consequences for the hadron spectrum, with no parity doubling, an approximate isospin symmetry, and the interpretation of pions as light pseudo-Goldstone bosons. In the next sections, we explore how these facts can be incorporated when constructing an EFT for NN interactions.

2.2.2 Pion interactions from chiral symmetry

We seek to construct an EFT of QCD, where nucleons and pions are the dynamical degrees of freedom instead of quarks and gluons. This is not the same situation as keeping the degrees of freedom and constructing an EFT by integrating out the high-energy modes. In the latter case, the connection between the underlying and effective theory is direct. The question is how the effective theory in terms of the different degrees of freedom has any connection to QCD. Weinberg addresses this in one of his seminal papers [9] and argues that: *if one writes down the most general possible Lagrangian, including all terms consistent with assumed symmetry principles, and then calculates matrix elements with this Lagrangian to any given order of perturbation theory, the result will simply be the most general possible S-matrix consistent with analyticity, perturbative unitarity, cluster decomposition and the assumed symmetry principles.* Although no formal proof of this statement exists, it is commonly referred to as Weinberg's theorem and has been a backbone of the construction of EFTs for the past half century.

The three pion fields $\boldsymbol{\pi}(x)$ are Goldstone bosons of the spontaneously broken chiral symmetry $G \equiv \mathrm{SU}(2)_L \times \mathrm{SU}(2)_R \to \mathrm{SU}(2)_V \equiv H$. By Weinberg's theorem, the effective Lagrangian describing low-energy pion dynamics should be invariant under both G and space-time symmetries, while the ground state (vacuum) is only invariant under H. One can formally show that there is an isomorphism between the Goldstone boson fields $\boldsymbol{\pi}(x)$ and the quotient space G/H, and that the Goldstone modes parameterize the symmetry in the spontaneously broken directions [14]. The pion fields can be written in the exponential parameterization $U(x) = \exp(i\boldsymbol{\pi}(x) \cdot \boldsymbol{\tau}/f_\pi)$, which transforms as $U \mapsto g_R U g_L^\dagger$ under $(g_L, g_R) \in G$ where $\boldsymbol{\tau} = (\tau_1, \tau_2, \tau_3)$. This representation of the pion fields makes it clear that the pions transform linearly under H in the adjoint representation, but in general non-linearly under G. This is sometimes referred to as a non-linear realization of chiral symmetry, which is necessary by the fact that G is isomorphic to SO(4), where the smallest faithful representation is four-dimensional, while there are only three pion fields. The formalism for constructing the most general Lagrangians consistent with broken symmetries was developed in Refs. [131, 132] and is known as the CCWS formalism, see also [128].

The most general pion Lagrangian can be constructed from $U(x)$, where explicit chiral symmetry breaking can be included by the method of external fields [12]. The resulting lowest-order Lagrangian with minimal number of derivatives reads

$$\mathcal{L}_{\pi\pi}^{(2)} = \frac{f_\pi^2}{4} \mathrm{Tr}\left[\partial_\mu U \partial^\mu U^\dagger + m_\pi^2 \left(U + U^\dagger\right)\right] = \frac{1}{2}\partial_\mu \boldsymbol{\pi} \partial^\mu \boldsymbol{\pi} - \frac{1}{2} m_\pi^2 \boldsymbol{\pi}^2 + \mathcal{O}(\boldsymbol{\pi}^4), \quad (2.7)$$

where interactions among four or more pions are omitted. The superscripts of the Lagrangians will indicate the number of derivatives/pion mass insertions. One important consequence to notice is that pion interactions always come with at least one derivative (from the chirally symmetric part) or with powers of the pion mass, m_π (from the explicit symmetry breaking part). This means that all interactions from the infinite set of invariant terms will carry powers of external momentum, k, or pion mass m_π. Thus, for low-energy processes with $k \sim m_\pi$, a consistent truncation in powers of $\{k, m_\pi\}/\Lambda_\chi$ can be made, where $\Lambda_\chi \approx 4\pi f_\pi$ is the expected breakdown scale of the EFT description in the pion sector. Another consequence of chiral symmetry is that the infinite number of possible interaction terms in Eq. (2.7) are parameterized in terms of only *two* constants: f_π and m_π.

2.2.3 Pion-nucleon and nucleon-nucleon interactions

Neutrons and protons can be collected as a nucleon isospin doublet of relativistic Dirac fields $\Psi = (\Psi_p, \Psi_n)^T$, and its Lagrangian can be constructed by considering chiral transformation properties of nucleons similar to the case of

pions. The leading-order Lagrangian reads

$$\mathcal{L}^{(1)}_{\pi\mathrm{N}} = \bar{\Psi}\left(i\not{D} - m_N + \frac{g_A}{2}\gamma^\mu\gamma_5 u_\mu\right)\Psi, \tag{2.8}$$

where g_A is the axial coupling, $D_\mu = \partial_\mu + \Gamma_\mu$ the chirally covariant derivative with $\Gamma_\mu = [\xi^\dagger, \partial_\mu\xi]/2$, and $u_\mu = i\{\xi^\dagger, \partial_\mu\xi\}$ for $\xi = \sqrt{U}$ [14]. The inclusion of nucleons inevitably introduces their mass $m_N \approx 940$ MeV, as an additional scale that cannot be considered small with respect to Λ_χ, and does not vanish in the chiral limit. However, we are interested in describing processes where the external three momenta are of order $k \sim m_\pi$, or at the order of typical Fermi momenta in nuclei, which both are much smaller than the nucleon mass. This means that nucleons can be treated non-relativistically.

A non-relativistic reduction of the nucleon field, known as the heavy-baryon formalism [133, 134], will eliminate the problems associated with a large nucleon mass. Let the nucleon momentum be parameterized as $p^\mu = m_N v^\mu + k^\mu$, where $v^2 = 1$ and $v_\mu k^\mu \ll m_N$ is proportional to the amount the nucleon is off-shell. Velocity-dependent fields are defined as

$$N = P_v^+ e^{i m_N v^\mu x_\mu}\Psi, \quad h = P_v^- e^{i m_N v^\mu x_\mu}\Psi, \tag{2.9}$$

for $P_v^\pm \equiv (\mathbb{1} \pm \not{v})/2$ such that $\Psi = \exp(-i m_N v^\mu x_\mu)(N + h)$. For the nucleon rest frame $v^\mu = (1, \mathbf{0})$, the projection in Eq. (2.9) is onto the upper (light) and lower (heavy) two components of the Dirac spinor Ψ. The Lagrangian in Eq. (2.8) can be expressed in terms of the fields N and h, where the latter can be eliminated systematically using the equations of motion (or the path integral formalism [135]), and the *nucleon field*, N, obeys the free equation of motion $v^\mu\partial_\mu N = 0$ up to m_N^{-1} corrections. This transformation is analogous to the Foldy–Wouthuysen transformation [136], and generates an effective Lagrangian for the nucleon field. The leading order Lagrangian in Eq. (2.8) can be expressed in terms of the nucleon field as

$$\mathcal{L}^{(1)}_{\pi\mathrm{N}} = \bar{N}\left(i\partial_0 - \frac{g_A}{2f_\pi}\boldsymbol{\tau}\cdot(\boldsymbol{\sigma}\cdot\boldsymbol{\nabla})\boldsymbol{\pi}\right)N + \mathcal{O}(\boldsymbol{\pi}^2) + \sum_{n=1}^{\infty}\frac{1}{(2m_N)^n}\mathcal{L}_{\mathrm{eff},n}, \tag{2.10}$$

where interactions involving more than two pion fields have been neglected. The remaining terms $\mathcal{L}_{\mathrm{eff},n}$ systematically parameterize the effects from antiparticles and relativistic corrections, which appear with factors of m_N^{-1} [14].

Manifest Lorentz invariance is lost in this non-relativistic Lagrangian where the explicit direction $v\cdot\partial = \partial_0$ is present. However, the Lorentz invariance is intact to all orders in the m_N^{-1} expansion, which manifests in relations among the effective interactions in $\mathcal{L}_{\mathrm{eff},n}$. These constraints can systematically be derived using reparameterization invariance [137].

The last piece to include for describing low-energy NN interactions is pure contact interactions. These are not constrained by chiral symmetry and read

to lowest order [10]

$$\mathcal{L}_{\rm NN}^{(0)} = -\frac{1}{2}C_S\bar{N}N\bar{N}N - \frac{1}{2}C_T\bar{N}\boldsymbol{\sigma}N\bar{N}\boldsymbol{\sigma}N, \tag{2.11}$$

where C_S and C_T are LECs, and parameterize unresolved short-distance dynamics. The values of the LECs are not predicted by the theory, but must be inferred from experimental data. This will be discussed primarily in Papers I and II. Parity invariance constrains contact interactions to contain an even number of derivatives.

Effective Lagrangians with a certain number of low-energy scales (superscripts) can be derived to obtain the expansions [123]

$$\mathcal{L}_{\pi\pi} = \mathcal{L}_{\pi\pi}^{(2)} + \mathcal{L}_{\pi\pi}^{(4)} + \mathcal{L}_{\pi\pi}^{(6)} + \ldots \tag{2.12}$$

$$\mathcal{L}_{\pi\rm N} = \mathcal{L}_{\pi\rm N}^{(1)} + \mathcal{L}_{\pi\rm N}^{(2)} + \mathcal{L}_{\pi\rm N}^{(3)} + \ldots \tag{2.13}$$

$$\mathcal{L}_{\rm NN} = \mathcal{L}_{\rm NN}^{(0)} + \mathcal{L}_{\rm NN}^{(2)} + \mathcal{L}_{\rm NN}^{(4)} + \ldots \tag{2.14}$$

where the full effective NN Lagrangian reads

$$\mathcal{L}_{\rm eff} = \mathcal{L}_{\pi\pi} + \mathcal{L}_{\pi\rm N} + \mathcal{L}_{\rm NN}. \tag{2.15}$$

Note that three- and many-nucleon interactions are also predicted and can be included in the effective Lagrangian. We will see that these are suppressed compared to the NN interaction, and are excluded from Eq. (2.15) since we only consider NN interactions in this thesis.

We have now explored the concept of an EFT, and seen how an effective Lagrangian for NN interactions can be constructed. Weinberg's theorem prescribes that the obtained description is consistent with QCD by including not only space-time symmetries, but also the spontaneously and explicitly broken chiral symmetry. In the next section, we will explore how to construct nuclear interaction potentials by developing a power counting to systematically truncate the infinite number of possible NN interactions given by Eq. (2.15).

2.3 Power counting and the nuclear potential

Nuclear force models can now be constructed from the effective Lagrangian in Eq. (2.15). This is done by considering NN scattering in the c.m. frame and computing the scattering amplitude, $\mathcal{A}$, from the effective Lagrangian in Eq. (2.15) and matching it to the non-relativistic amplitude from a quantum mechanical potential in the Born approximation, giving $V = i\mathcal{A}$. The definition of a quantum mechanical potential can also be made more formal using a non-relativistic reduction of the Bethe-Salpeter equation to properly account for the non-perturbative case, see, e.g., Ref [138].

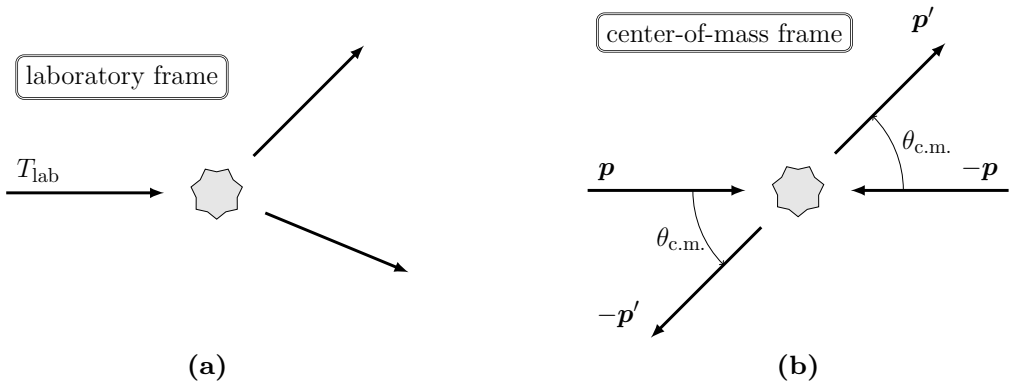

Figure 2.2: Illustration of NN scattering in the laboratory frame **(a)** and c.m. frame **(b)**. $T_{\rm lab}$ denotes the laboratory scattering energy and $\boldsymbol{p}$ ($\boldsymbol{p}'$) the ingoing (outgoing) scattering momentum in the c.m. frame.

2.3.1 Non-relativistic two-nucleon scattering

Two-nucleon scattering is illustrated in Fig. 2.2, and NN states can be described in the relative momentum basis

$$|\boldsymbol{p} s m_s t m_t\rangle\,, \tag{2.16}$$

where $\boldsymbol{p}$ is the NN relative momentum in the c.m. frame. Note that $\boldsymbol{p}$ is equal to the c.m. momentum, shown in Fig. 2.2. The quantum numbers of NN isospin ($\boldsymbol{T}$), angular momentum ($\boldsymbol{L}$) and spin ($\boldsymbol{S}$) are denoted t, ℓ, and s, respectively. The NN spin and isospin projections are denoted m_s and m_t. We employ the normalization

$$\langle \boldsymbol{p}' s' m_s' t' m_t' | \boldsymbol{p} s m_s t m_t\rangle = (2\pi)^3\,\delta^{(3)}\left(\boldsymbol{p}'-\boldsymbol{p}\right)\delta_{s's}\delta_{m_s' m_s}\delta_{t't}\delta_{m_t' m_t}. \tag{2.17}$$

The S-matrix describes how an incoming NN state is transformed by the scattering process and reads [139]

$$S = \mathbb{1} - 2\pi i \delta(E - H_0) T(E). \tag{2.18}$$

Here, $H_0 = \boldsymbol{p}^2/m_N$ is the free Hamiltonian, E is the c.m. energy of the incoming NN state, and T is the off-shell T-matrix that satisfies the Lippmann-Schwinger (LS) equation for a given potential V,

$$T(E) = V + V\frac{1}{E - H_0 + i\epsilon}T(E). \tag{2.19}$$

The amplitude of non-forward scattering is conventionally parameterized in terms of the spin scattering matrix, which reads [140]

$$M^{st}_{m_s' m_s}(\boldsymbol{p}', \boldsymbol{p}) = -\frac{m_N}{4\pi}\,\langle \boldsymbol{p}' s m_s' t m_t | T(E)\,(\mathbb{1} - P_{12})\,|\boldsymbol{p} s m_s t m_t\rangle\,. \tag{2.20}$$

The isospin projection (m_t) is conserved since it measures the charge of the two nucleons, while isospin (t) conservation is assumed. The conservation of isospin and parity, together with the Pauli principle, implies that total spin (s) is also conserved. Note that the antisymmetrization procedure in Eq. (2.20) performed with the two-nucleon permutation operator P_{12} is equivalent to considering matrix elements of $T(E)$ between two normalized antisymmetrized states. We will mainly consider np scattering, for which the M-matrix equivalently can be parameterized in terms of the laboratory kinetic energy of the impinging neutron, $T_{\rm lab}$, and the c.m. scattering angle $\theta_{\rm c.m.}$ for $|\boldsymbol{p}'| = |\boldsymbol{p}| = k$, where

$$k = \sqrt{\frac{m_p^2 T_{\rm lab}(2m_n + T_{\rm lab})}{(m_n + m_p)^2 + 2m_p T_{\rm lab}}}. \tag{2.21}$$

An np state has $m_t = 0$ and both $t = 0, 1$ are possible. The Pauli principle constrains the quantum numbers, ℓ, s, and t to obey $(-1)^{\ell+s+t} = -1$. This means that t is implicitly given by ℓ and s, and can be omitted from the notation. Antisymmetric np partial-wave states are characterized by $|p\ell sj\rangle$ where $p = |\boldsymbol{p}|$ and j is the quantum number associated with the total angular momentum operator, $\boldsymbol{J} = \boldsymbol{L} + \boldsymbol{S}$. Spectroscopic notation ${}^{2s+1}\ell_j$, where $\ell = 0, 1, 2, 3, \ldots$ is denoted $S, P, D, F, \ldots$, will be used to label partial waves. An np scattering channel is characterized by the conserved quantum numbers j, s, and parity $\Pi = (-1)^\ell$. This leads to the constraint that ℓ can change by 0 or ± 2.

2.3.2 Power counting

We want to consider NN scattering in the c.m. frame and compute the scattering amplitude using the effective Lagrangian in Eq. (2.15). There are formally an infinite number of Feynman diagrams that contribute to the scattering amplitude, but the EFT construction generally guarantees that only a finite number of diagrams are relevant for studying processes at scales $Q \sim k, m_\pi$. To find a consistent truncation of diagrams in orders $(Q/\Lambda_b)^\nu$, we must evaluate their scaling in powers of external c.m. momenta and pion masses [10]. Note that the breakdown scale for χEFT, denoted Λ_b, differs from the breakdown scale of χPT [39, 141].

The propagator for a nucleon with four momentum $p^\mu = mv^\mu + l^\mu$ can be extracted from Eq. (2.10) as $(l^0 + i\epsilon)^{-1}$, and each nucleon propagator will thus contribute a factor Q^{-1}. Pion propagators contribute the usual Q^{-2} (as seen from Eq. (2.7)), each derivative or pion mass contributes a factor Q, and four-momentum integration Q^4. The total power of a diagram (also referred to as chiral order) is thus [10, 11]

$$\nu = 4L - 2I_\pi - I_N + \sum_i d_i V_i, \tag{2.22}$$

Figure 2.3: Feynman diagrams of order $(Q/\Lambda_b)^0$; nucleon contact interaction **(a)**, and OPE **(b)**. Solid lines show nucleons (N) and dashed lines show pions (π). We omit the fermion arrows since the effective theory does not contain any propagating anti-nucleons, and no ambiguities arise.

where L is the number of loops, I_π (I_N) is the number of pion (nucleon) propagators, and d_i is the number of derivatives/pion masses for vertex type i, and V_i is the number of vertices of type i. Determining the scaling of diagrams to systematically assess their importance has thus become known as PC. We will later use the term PC in a slightly wider context.

The expression in Eq. (2.22) can be simplified using topological relations, and for two nucleons in the initial and final state it reads[4] [11]

$$\nu = 2L + \sum_i V_i \left[d_i + \frac{n_i}{2} - 2 \right]. \tag{2.23}$$

Here, n_i denotes the number of nucleon fields in an interaction of type i. Any interaction in Eq. (2.15) must either have no nucleon fields and at least two derivatives or pion masses ($\mathcal{L}_{\pi\pi}$), or two nucleon fields and at least one derivative ($\mathcal{L}_{\pi\mathrm{N}}$), or at least four nucleon fields and any number of derivatives ($\mathcal{L}_{\mathrm{NN}}$). Hence, $\Delta_i \equiv d_i + n_i/2 - 2 \geq 0$ is guaranteed by chiral symmetry. The expression in Eq. (2.23) shows that the leading diagrams will be those without loops and with interaction index $\Delta_i = 0$. Two diagrams can be constructed for $\nu = 0$; a nucleon contact without derivatives and the OPE, as shown in Fig. 2.3. The momentum space expressions for the resulting potentials read [10]

$$V_{\mathrm{ct}}^{(0)}(\boldsymbol{p}', \boldsymbol{p}) \equiv \langle \boldsymbol{p}' | V_{\mathrm{ct}}^{(0)} | \boldsymbol{p} \rangle = C_S + C_T \boldsymbol{\sigma}_1 \cdot \boldsymbol{\sigma}_2, \tag{2.24}$$

$$V_{1\pi}^{(0)}(\boldsymbol{p}', \boldsymbol{p}) = -\frac{g_A^2}{4 f_\pi^2} \frac{(\boldsymbol{\sigma}_1 \cdot \boldsymbol{q})(\boldsymbol{\sigma}_2 \cdot \boldsymbol{q})}{\boldsymbol{q}^2 + m_\pi^2} (\boldsymbol{\tau}_1 \cdot \boldsymbol{\tau}_2), \tag{2.25}$$

where $\boldsymbol{q} = \boldsymbol{p}' - \boldsymbol{p}$. Note that diagrams where the outgoing nucleons are exchanged are not considered, even though the nucleons are identical. This can

[4] This relation can be generalized to any number of nucleons [11] where it can be shown that A-nucleon forces arise first at order $\nu = 2A - 4$ (note that the three-nucleon force at $\nu = 2$ exactly cancel). Here, we restrict the discussion to the case of two nucleons.

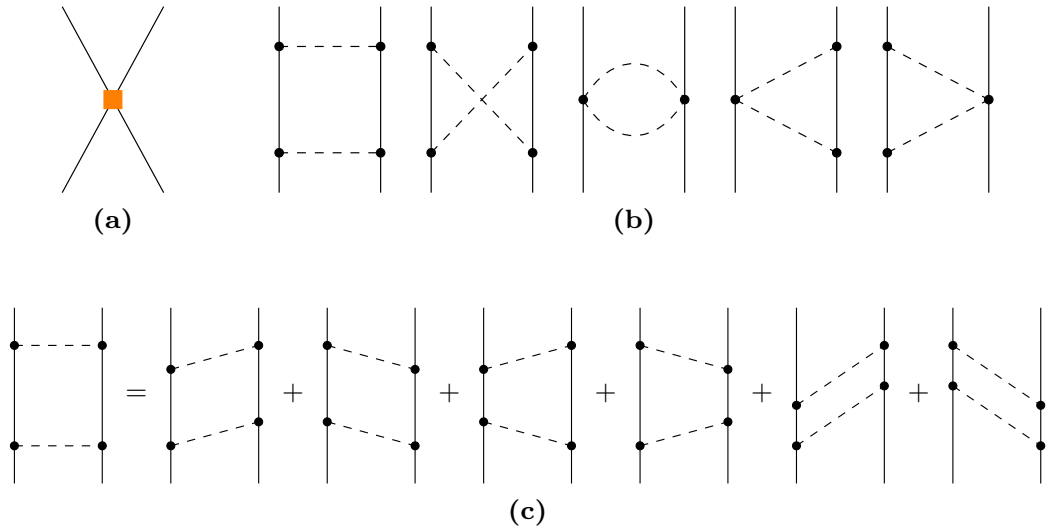

Figure 2.4: **(a)** Nucleon contact diagram of order $(Q/\Lambda_b)^2$. **(b)** Two-pion-exchange diagrams of order $(Q/\Lambda_b)^2$. **(c)** The two-pion-exchange box diagram expanded in time-ordered graphs. The last two time-ordered diagrams are two-nucleon irreducible, while the first four contain purely nucleonic intermediate states and are reducible. Solid lines represent nucleons and dashed lines represent pions.

be understood from Eq. (2.20), where the exchange diagrams are automatically accounted for by considering scattering matrix elements between properly anti-symmetrized NN states. Note that two more contact-interaction structures are consistent with the given symmetries and can be added to Eq. (2.24). However, these are redundant which can be shown by applying a Fierz transformation [10], or by considering antisymmetrization of the potential [142].

The PC in Eq. (2.22) prescribes that only two diagrams contribute to the NN amplitude at LO. This is clearly somewhat suspicious, since the NN spectrum contains a bound state (the deuteron), which can only be generated non-perturbatively. The PC clearly needs some additional ingredient to properly describe NN amplitudes, which will be explored in the next section. However, in the one-nucleon sector, the PC defined by Eq. (2.22) can successfully be applied in χPT.

2.3.3 Infrared enhancement for two-nucleon states

To describe the non-perturbative nature of the NN force from this EFT of nucleons and pions, some contributions that are assigned $\nu > 0$ according to Eq. (2.23) must contain some enhancement to necessitate promotion to LO. No diagrams with $\nu = 1$ exist due to parity- and time-reversal symmetry, and the first subleading diagrams at $\nu = 2$ are shown in Fig. 2.4a and Fig. 2.4b. Weinberg identified an enhancement in subleading diagrams that contain purely

nucleonic intermediate states. The two-pion-exchange box diagram is an example of such a diagram, and is shown in Fig. 2.4c together with its expansion into time-ordered graphs. The diagrams with purely nucleonic intermediate states contain so-called pinch-singularities when treated in covariant perturbation theory using the heavy-baryon formalism [10, 11], since they contain two nucleon propagators $(q^0+i\epsilon)^{-1}(-q^0+i\epsilon)^{-1}$ that pinch the dq^0 loop integration between poles $q^0 \pm i\epsilon$, causing an infrared divergence. This singularity is, however, an artifact of the heavy-baryon formalism, and including the nucleon kinetic term $\mathcal{L}_{\rm kin} = \bar{N}\nabla^2/(2m_N)N$ moves the poles, removing the divergence. However, the fact remains that purely nucleonic intermediate states have propagators that are enhanced compared to the Q^{-1} scaling assumed in Eq. (2.22).

The infrared enhancement in diagrams with purely nucleonic intermediate states is most easily analyzed in old-fashioned time-ordered perturbation theory, since the energy integration dq^0 is already performed [11]. The time-ordered expansion of the two-pion-exchange box is displayed in Fig. 2.4c, and in these diagrams the energies of the intermediate states explicitly show up in energy denominators [115]. Two classes of diagrams can be identified. The first are irreducible ones, in which intermediate states at any given time contain at least one pion, which guarantees that the energy denominators contain factors of $\sqrt{\boldsymbol{q}^2+m_\pi^2}$, for some pion momentum transfer $\boldsymbol{q}$. These are the last two diagrams in Fig. 2.4c. The other class is reducible diagrams, which contain purely nucleonic intermediate states that produce energy denominators

$$\frac{1}{E-E_{\boldsymbol{l}}} = \frac{1}{\boldsymbol{p}^2/m_N - \boldsymbol{l}^2/m_N} \sim \frac{m_N}{Q^2}. \tag{2.26}$$

These are the first four diagrams in Fig. 2.4c. Here, $E = \boldsymbol{p}^2/m_N$ is the initial energy and $\boldsymbol{l}$ is the loop three-momentum, all given in the c.m. frame. These small-energy denominators in Eq. (2.26) cause an infrared enhancement in reducible diagrams, meaning that they give a larger contribution than assumed in Eq. (2.22). The reducible time-ordered box diagrams are counted as LO if one adopts the counting rule that the nucleon mass is a separate hard scale according to $m_N \simeq \Lambda_b^2/Q > \Lambda_b$, i.e., factors of (Q/m_N) are equivalent to two chiral orders. This counting rule places an infinite number of contributions at LO, since all pion-exchange ladder diagrams are now counted as LO. This can be understood from Eq. (2.23) where the addition of an extra loop will be canceled by the enhancement $(m_N/Q) = (\Lambda_b/Q)^2$.

Weinberg suggested applying the PC defined by Eq. (2.23) to construct effective potentials of irreducible diagrams using time-ordered perturbation theory, and then iterating this potential in the LS equation to generate all enhanced diagrams with purely nucleonic intermediate states to construct the full amplitude. However, potentials constructed in this way will contain an energy dependence, which is problematic for applications beyond the NN system. One way of avoiding this is to apply the method of unitary transformation to isolate

the purely nucleonic part of the Fock space [23–25]. The energy dependence in the potentials can also be avoided by sticking to covariant perturbation theory and performing the non-relativistic m_N^{-1} expansion *after* computing the loop-integrals [123, 142].

Let us explicitly consider the two-nucleon box diagram shown in Fig. 2.4c and divide it into the infrared enhanced (iterated) and irreducible parts

$$V^{(2)}_{2\pi,\mathrm{box}} = V^{\mathrm{it}}_{2\pi,\mathrm{box}} + V_{2\pi,\mathrm{box}}. \tag{2.27}$$

The irreducible part ($V_{2\pi,\mathrm{box}}$) scales with the correct chiral order as shown in explicit calculations [142], in this case $\nu = 2$. The enhanced part can be expressed as [123]

$$\begin{aligned} V^{\mathrm{it}}_{2\pi,\mathrm{box}}(\boldsymbol{p}',\boldsymbol{p}) = {} & \frac{g_A^2 m_N}{16 f_\pi^4}\,(3 - 2\boldsymbol{\tau}_1\cdot\boldsymbol{\tau_2}) \\ & \times \int \frac{d^3\boldsymbol{l}}{(2\pi)^3}\,\frac{(\boldsymbol{\sigma}_1\cdot\boldsymbol{q}_1)\,(\boldsymbol{\sigma}_2\cdot\boldsymbol{q}_1)}{\boldsymbol{q}_1^2 + m_\pi^2}\,\frac{1}{\boldsymbol{p}^2 - \boldsymbol{l}^2 + i\epsilon}\,\frac{(\boldsymbol{\sigma}_1\cdot\boldsymbol{q}_2)\,(\boldsymbol{\sigma}_2\cdot\boldsymbol{q}_2)}{\boldsymbol{q}_2^2 + m_\pi^2} \end{aligned} \tag{2.28}$$

where $\boldsymbol{q}_1 = \boldsymbol{p}' + \boldsymbol{l}$ and $\boldsymbol{q}_2 = \boldsymbol{p} + \boldsymbol{l}$. This expression can be identified as the second-order term in the Born series from iterating $V^{(0)}_{1\pi}$, namely

$$\langle \boldsymbol{p}'|\, V^{(0)}_{1\pi} G_0^+ V^{(0)}_{1\pi}\, |\boldsymbol{p}\rangle = \int \frac{d^3\boldsymbol{l}}{(2\pi)^3} V^{(0)}_{1\pi}\,(\boldsymbol{p}',\boldsymbol{l})\,\frac{m_N}{\boldsymbol{p}^2 - \boldsymbol{l}^2 + i\epsilon} V^{(0)}_{1\pi}\,(\boldsymbol{l},\boldsymbol{p})\,, \tag{2.29}$$

where

$$\langle \boldsymbol{l}'|G_0^+(E)|\boldsymbol{l}\rangle = \frac{m_N}{\boldsymbol{p}^2 - \boldsymbol{l}^2 + i\epsilon}(2\pi)^3\delta^3(\boldsymbol{l}' - \boldsymbol{l}) \tag{2.30}$$

is the Schrödinger propagator in momentum space for an on-shell energy $E = \boldsymbol{p}^2/m_N$. This illustrates that the infrared-enhanced diagrams with purely nucleonic intermediate states are given by *iterations* like Eq. (2.29). This realization is the basis for constructing nuclear potentials that are treated in the non-relativistic Schrödinger and LS equations.

2.3.4 The nuclear interaction potential

We are now in a position to summarize the procedure to construct potentials in WPC. Potential contributions at each chiral order, $V^{(\nu)}$, are given by the irreducible components of diagrams at chiral order ν. The full scattering amplitude, $T^{(\nu)}_{\mathrm{WPC}}$, is computed from the potential $V^{(\nu)}_{\mathrm{WPC}} = \sum_{n=0}^{\nu} V^{(n)}$ by solving the LS equation

$$T^{(\nu)}_{\mathrm{WPC}}(\boldsymbol{p}',\boldsymbol{p}) = V^{(\nu)}_{\mathrm{WPC}}(\boldsymbol{p}',\boldsymbol{p}) + \int \frac{d^3\boldsymbol{l}}{(2\pi)^3} V^{(\nu)}_{\mathrm{WPC}}(\boldsymbol{p}',\boldsymbol{l})\frac{m_N}{\boldsymbol{p}^2 - \boldsymbol{l}^2 + i\epsilon} T^{(\nu)}_{\mathrm{WPC}}(\boldsymbol{l},\boldsymbol{p}), \tag{2.31}$$

for on-shell energy $E = \boldsymbol{p}^2/m_N$. Iterating the potential in the LS equation will automatically include the enhanced parts of diagrams with purely nucleonic intermediate states that were excluded from the potential. This can be seen by simply writing the Born series for Eq. (2.31), i.e.,

$$T^{(\nu)}_{\mathrm{WPC}} = V^{(\nu)}_{\mathrm{WPC}} + V^{(\nu)}_{\mathrm{WPC}} G^{+}_{0}(E) V^{(\nu)}_{\mathrm{WPC}} + \ldots , \tag{2.32}$$

where the second term in the LO amplitude generates the expression in Eq. (2.29).

The magnitude of the loop momentum in Eq. (2.31) generally needs to be regulated to make the amplitude $T^{(\nu)}_{\mathrm{WPC}}$ finite. This regulation is commonly introduced in the potential. We employ a non-local regulator of the form

$$V^{(\nu)}(\boldsymbol{p}', \boldsymbol{p}) \to \exp\left(-\frac{|\boldsymbol{p}'|^n}{\Lambda^n}\right) V^{(\nu)}(\boldsymbol{p}', \boldsymbol{p}) \exp\left(-\frac{|\boldsymbol{p}|^n}{\Lambda^n}\right) , \tag{2.33}$$

where Λ is referred to as the momentum cutoff. We choose $n = 6$, except for in Paper I, where we use the regulator of Ref. [106]. The non-local regulation in Eq. (2.33) is convenient because it commutes with the partial-wave decomposition used to solve Eq. (2.31), unlike local regulators [143, 144]. Many studies explore different types of regulation [46, 145, 146], and we will briefly revisit the regulator form when discussing so-called exceptional cutoffs [96] in Chapter 5.

It was early realized that the cutoff dependence in predicted observables cannot be eliminated in WPC [69, 70], which is due to the singular nature of the emerging pion-exchange potentials in χEFT. This issue will be studied in detail. Crucially, we will see that there are ways of mitigating this cutoff dependence by further modifying WPC. Studying such modified PCs is the central topic of this thesis and will be the subject of Chapters 3 and 5.

Chapter 3

The two-nucleon system with partly perturbative pions

In this chapter, we will explore how to construct NN interactions from χEFT with a modified PC that incorporates cutoff independence at each order. We start by discussing singular potentials and how they produce an uncontrolled cutoff dependence. We then demonstrate how to construct a modified version of Weinberg's PC that retains cutoff independence at each order, where pion-exchange interactions are included partly perturbatively. It is then described how this PC is implemented up to N^{3}LO to study *np* scattering observables and low-energy theorems. The detailed analysis of the NN system presented in this chapter is an important step to reach few-nucleon systems, studied in Chapter 5. The perturbative NN computations presented in this thesis are implemented in the publicly available code `nn-mwpc` [147].

3.1 Cutoff dependence and singular potentials

An attractive potential is singular if its short-distance behavior is $-|\lambda|/r^n$ for $n \geq 2$, where $\boldsymbol{r}$ is the two-nucleon relative position, and $r = |\boldsymbol{r}|$. For the limiting case $n = 2$, the potential is singular only for sufficiently large λ [80, 148]. Why the limiting case in non-relativistic quantum mechanics is $n = 2$ can be explained by the uncertainty principle. It prescribes the scaling of $\sim 1/r^2$ for the kinetic energy. For $n > 2$ and sufficiently small r, the negative potential will dominate over the positive kinetic energy and centrifugal barrier, leading to the energy being unbounded from below. This prohibits a well-defined solution to the Schrödinger equation and is the quantum version of two particles collapsing to $r = 0$.

The OPE potential in Eq. (2.25) emerges as a LO contribution to the NN

interaction in χEFT using WPC. The position space expression for OPE reads

$$V_{1\pi}^{(0)}(\boldsymbol{r}) = \int \frac{d^3\boldsymbol{q}}{(2\pi)^3}\, V_{1\pi}^{(0)}(\boldsymbol{p}', \boldsymbol{p}) \tag{3.1}$$

$$= \frac{m_\pi^2}{12\pi}\left(\frac{g_A}{2f_\pi}\right)^2 \boldsymbol{\tau}_1\cdot\boldsymbol{\tau}_2\left[T(r)S_{12} + \left(Y(r) - \frac{4\pi}{m_\pi^2}\delta^3(\boldsymbol{r})\right)\boldsymbol{\sigma}_1\cdot\boldsymbol{\sigma}_2\right], \tag{3.2}$$

where $\boldsymbol{q} = \boldsymbol{p}' - \boldsymbol{p}$ is the momentum transfer, $S_{12} = 3\,(\boldsymbol{\sigma}_1\cdot\hat{\boldsymbol{r}})\,(\boldsymbol{\sigma}_2\cdot\hat{\boldsymbol{r}}) - \boldsymbol{\sigma}_1\cdot\boldsymbol{\sigma}_2$ is the tensor operator ($\hat{\boldsymbol{r}} = \boldsymbol{r}/r$), and

$$T(r) = \frac{e^{-m_\pi r}}{r}\left[1 + \frac{3}{m_\pi r} + \frac{3}{(m_\pi r)^2}\right], \quad Y(r) = \frac{e^{-m_\pi r}}{r}. \tag{3.3}$$

This potential is singular in partial waves where the matrix element of $\boldsymbol{\tau}_1\cdot\boldsymbol{\tau}_2 S_{12}$ is negative, since $T(r) \sim 1/r^3$ for $r \ll m_\pi^{-1} \approx 1.4$ fm. More generally, pion-exchange potentials at order ν show an increasingly singular behavior for small r, and behave as $V^{(\nu)}(\boldsymbol{r}) \sim 1/r^{3+\nu}$. This can be understood from the PC, where higher powers of momenta translate to higher powers of $1/r$ in position space.[1]

The Hamiltonian for an attractive singular potential is not well defined since it does not correspond to a self-adjoint operator [80]. It is, however, possible to construct self-adjoint extensions. The number of parameters needed to determine such an extension is called the deficiency index, which for attractive singular potentials in three dimensions is infinite [150] — one constant (counterterm) is needed in each partial wave. In the case of OPE, there are infinitely many spin-triplet partial waves where $\boldsymbol{\tau}_1\cdot\boldsymbol{\tau}_2 S_{12}$ is negative, all of which need a counterterm to determine a self-adjoint extension [70]. This would obviously spoil the predictive power of χEFT. However, the centrifugal barrier shields the singular attraction and effectively limits the number of partial waves that require a counterterm.

In practice, all potentials are regulated before solving the Schrödinger (or LS equation), see Eq. (2.33). The regulation effectively removes the singular short-distance part, yielding a well-defined scattering amplitude. The potential's singularity instead manifests as an uncontrolled cutoff dependence in the predicted amplitudes. The ${}^3P_0$ partial wave is an example of where the OPE potential is singular and attractive, and the left panel of Fig. 3.1 shows the cutoff dependence of the *np* scattering phase shift at two different scattering energies. As expected, a significant cutoff dependence is observed.

The procedure to construct a self-adjoint extension [150] can be cast into the modern language of renormalization theory. A counterterm, consisting of a contact interaction with strength determined by a LEC, is added to the potential.

[1] Singular potentials and non-renormalizable field theories are tightly connected [149].

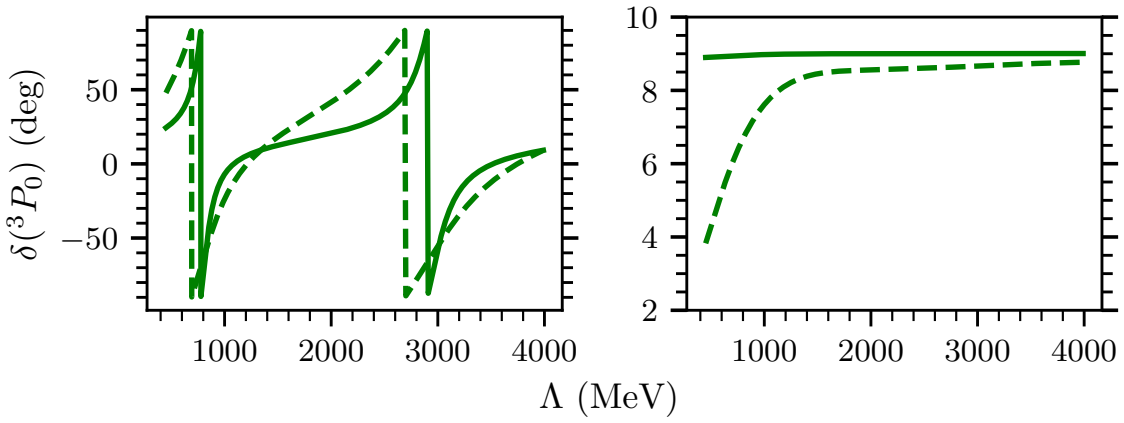

Figure 3.1: Predicted phase shifts in the $^3P_0$ channel at $T_{\rm lab} = 30$ MeV (solid) and $T_{\rm lab} = 100$ MeV (dashed) as a function of momentum cutoff, Λ. The left panel shows the result for pure OPE. In the right panel, an additional short-range counterterm is included.

The LEC is then calibrated to reproduce some observable (or amplitude) at each value of the cutoff, and the resulting cutoff-*dependent* counterterm in the potential will run with Λ to provide cutoff-*independent* predictions. The right panel in Fig. 3.1 shows predicted phase shifts in the $^3P_0$ partial wave for the OPE potential plus a counterterm, where the LEC is fixed by reproducing the scattering phase shift at $T_{\rm lab} = 25$ MeV. This demonstrates that well-defined cutoff-independent (RG-invariant) solutions to the LS equation can be obtained from a singular potential by adding a short-range counterterm that absorbs the divergence [70, 81, 151, 152].

In WPC, only S-wave counterterms in the channels $^1S_0$ and $^3S_1{-}^3D_1$ are prescribed at LO, see Eq. (2.24). This clearly illuminates a problematic feature of WPC; namely, predicted amplitudes and observables will receive a cutoff dependence from all singular pion-potential contributions without the required counterterm. This observation is the basis for seeking alternative modified PCs, where the cutoff independence of amplitudes is also used as a guiding principle when organizing the contributions to the nuclear force at each order. A central feature of such modified PC schemes is to promote subleading contact interactions to absorb the cutoff dependence caused by the singular potentials, as seen in the $^3P_0$ example.

The singular nature of the potential can also be obscured by keeping the cutoff at the order of the breakdown scale. This approach is used in WPC and is advocated in Refs. [25, 36, 46, 95–97, 100, 102]. It has proved successful in constructing nuclear interaction potentials from χEFT. Cutoff artifacts from singular potentials can be tolerated as long as they are smaller than the EFT truncation error. We will not pursue the finite-cutoff approach further in this

thesis, but instead focus on the less explored approach of constructing and evaluating PCs guided by cutoff independence.

3.2 Power counting guided by cutoff independence

We will now explore how to construct modified versions of WPC where cutoff independence, i.e. RG invariance, is used as a guiding principle. A momentum cutoff (or more generally, any type of regulation) is simply a way of splitting short-distance physics between loops and LECs. This is something that should not affect observables at scales $\ll \Lambda$. Specifically, changing Λ in the LS equation will explicitly include more or less short-range physics, which should be possible to compensate for by adjusting the available LECs in the potential. It is therefore essential to include the necessary counterterms with their associated LECs to be able to obtain cutoff-independent results.[2]

3.2.1 Partly perturbative pions and peripheral waves

The short-range nature of the nuclear interaction means that its strength decreases with increasing orbital angular momentum ℓ, which eventually allows for a perturbative treatment [142]. The centrifugal barrier

$$V(\boldsymbol{r}) \to V(\boldsymbol{r}) + \frac{\ell(\ell+1)}{m_N r^2}, \tag{3.4}$$

also shields the singular OPE potential for low-enough scattering energies. The feasibility of a perturbative treatment of OPE in different partial waves has been investigated in Refs. [82, 83, 104]. A conservative estimate is that a non-perturbative treatment of OPE is only needed in partial waves with $\ell \leq 1$, considering c.m. momenta up to $k \approx 400$ MeV. This means that only a few attractive singular partial waves need a counterterm promoted to LO, since the partial waves with $\ell > 1$ can be treated perturbatively and do not require a counterterm. The partly perturbative treatment of OPE effectively avoids the need to introduce an infinite number of counterterms, and is referred to as *partly perturbative pions* [72]. This approach can be viewed as a modification of the early attempt in Refs. [75, 76] where the renormalization problem was addressed by treating pion interactions entirely perturbatively.

The LO WPC potential, $V^{(0)}_{\text{WPC}} = V^{(0)}_{1\pi} + V^{(0)}_{\text{ct}}$ (see Eqs. (2.24) and (2.25)), is treated non-perturbatively in all partial waves. In contrast, the modified LO

[2] One objection to the approach of constructing PCs based on cutoff independence is that the cutoff should not be raised above the breakdown scale of the EFT, and that the singular parts of the potentials that call for the promotion of additional counterterms are unphysical predictions [95–97, 101].

potential proposed in Ref. [70], is instead only non-zero in the channels: ${}^1S_0$, ${}^3S_1{-}{}^3D_1$, ${}^3P_0$, ${}^1P_1$, ${}^3P_1$, and ${}^3P_2{-}{}^3F_2$, and reads

$$V^{(0)}(\boldsymbol{p}',\boldsymbol{p}) = -\frac{g_A^2}{4f_\pi^2}\frac{(\boldsymbol{\sigma}_1\cdot\boldsymbol{q})\,(\boldsymbol{\sigma}_2\cdot\boldsymbol{q})}{\boldsymbol{q}^2+m_\pi^2}\,(\boldsymbol{\tau}_1\cdot\boldsymbol{\tau}_2) + C_{^1S_0}\hat{P}_{^1S_0} + C_{^3S_1}\hat{P}_{^3S_1} + \Big[D_{^3P_0}\hat{P}_{^3P_0} + D_{^3P_2}\hat{P}_{^3P_2}\Big]\,p'p. \tag{3.5}$$

The partial-wave projectors and LECs are denoted by $\hat{P}_X$ and C_X, respectively, where the P-wave contacts are promoted $\nu = 2$ contributions to counter the singular attraction in the ${}^3P_0$ and ${}^3P_2{-}{}^3F_2$ channels. This is the LO potential that will be considered in this thesis. The OPE potential in the remaining partial waves ${}^1D_2$, ${}^3D_2, \ldots$ is included perturbatively. A perturbative treatment of all subleading orders is necessary to achieve RG invariance when including more singular subleading corrections. In fact, a perturbative treatment is also a natural consequence of consistently applying the PC at the amplitude level — as we will now see.

3.2.2 Perturbative subleading orders

In WPC, the PC is performed at the potential level, yielding $V^{(\nu)}_{\mathrm{WPC}} = \sum_{n=0}^{\nu} V^{(n)}$ as the sum of all potential contributions up to some order ν. These potentials are then employed non-perturbatively, e.g., in the LS equation giving the Born series (see Eq. (2.32))

$$T^{(\nu)}_{\mathrm{WPC}} = \sum_{n=0}^{\nu} V^{(n)} + \left[\sum_{n=0}^{\nu} V^{(n)}\right] G_0^+ \left[\sum_{n=0}^{\nu} V^{(n)}\right] + \ldots. \tag{3.6}$$

This series contains terms of orders higher than ν. For example, $V^{(\nu)}G_0^+V^{(\nu)}$ is of order 2ν. It is not inconsistent to include parts of higher-order contributions. However, a consistent amplitude truncation is beneficial to avoid introducing additional cutoff dependence. The increased singularity of higher-order potentials means that the subleading contributions will dominate at small enough distances. Long et al. [84] studied how to obtain RG-invariant results also at subleading chiral orders once the LO singular potential is properly renormalized according to Eq. (3.5). They showed that this can be done by including the subleading potentials in distorted-wave perturbation theory, with the distortion made by the LO potential.[3]

The distorted-wave Born series naturally emerges if the PC in Eq. (2.22) (supplemented by the infrared enhancement) is applied to the scattering amplitude. By collecting terms in Eq. (3.6) of the same chiral order and equating

[3]There is a complication of so-called exceptional cutoffs that show up when doing perturbation theory on top of a singular LO potential [96]. We will come back to this in Chapter 5.

them with the corresponding amplitude expansion $T = T^{(0)} + T^{(1)} + \ldots$, one obtains

$$T^{(0)} = V^{(0)} + V^{(0)}G_0^+V^{(0)} + V^{(0)}G_0^+V^{(0)}G_0^+V^{(0)} + \ldots, \tag{3.7}$$

$$T^{(1)} = V^{(1)} + V^{(1)}G_0^+V^{(0)} + V^{(0)}G_0^+V^{(1)} + V^{(1)}G_0^+V^{(0)}G_0^+V^{(0)} \ldots, \tag{3.8}$$

and so on. The LO amplitude is, by construction, given by an infinite number of diagrams from the infrared enhancement, as we saw in Chapter 2. From Eq. (3.8), it is seen that the subleading corrections $T^{(\nu>0)}$ also receive an infinite number of contributions. However, this is only a consequence of the non-perturbative nature of LO, and the subleading corrections can be expressed in a distorted-wave expansion. By introducing the Møller wave operators $\Omega_+ = \mathbb{1} + G_0^+T^{(0)}$ and $\Omega_-^\dagger = \mathbb{1} + T^{(0)}G_0^+$, as well as $G_1^+ = \Omega_+G_0^+$ it is straightforward to arrive at the expressions

$$T^{(1)} = \Omega_-^\dagger V^{(1)}\Omega_+, \tag{3.9}$$

$$T^{(2)} = \Omega_-^\dagger \left(V^{(2)} + V^{(1)}G_1^+V^{(1)}\right)\Omega_+, \tag{3.10}$$

$$T^{(3)} = \Omega_-^\dagger \Big(V^{(3)} + V^{(2)}G_1^+V^{(1)} + V^{(1)}G_1^+V^{(2)} + V^{(1)}G_1^+V^{(1)}G_1^+V^{(1)}\Big)\Omega_+. \tag{3.11}$$

This shows that subleading corrections to the amplitude are naturally expressed as perturbations around LO. The expressions in Eqs. (3.9) to (3.11) can equivalently be derived using the two-potential trick [153], see Paper II.

Another advantage of including subleading corrections perturbatively (besides attaining cutoff independence) is that it provides a consistency check of whether the contributions deemed as subleading are indeed perturbative with respect to LO [72, 154]. This consistency check is not fully taken advantage of when computing the amplitudes non-perturbatively in WPC. However, a perturbative treatment also introduces complications; a suitable starting point (LO) is necessary to attain a converging expansion. This makes strictly perturbative computations more challenging when it comes to calibrating the values of LECs, which is explored in Papers I and II (see Sections 3.4 and 3.5).

3.2.3 The Long and Yang power counting

We have seen how to treat the singular OPE potential at LO by promoting counterterms, and we showed that subleading corrections should naturally be included perturbatively using Eqs. (3.9) to (3.11). We will now put these pieces together and describe the resulting PC that is employed in this thesis.

Based on the LO potential in Eq. (3.5), Long and Yang [90–92] performed an extensive analysis to construct a PC up to N^{3}LO following the principles:

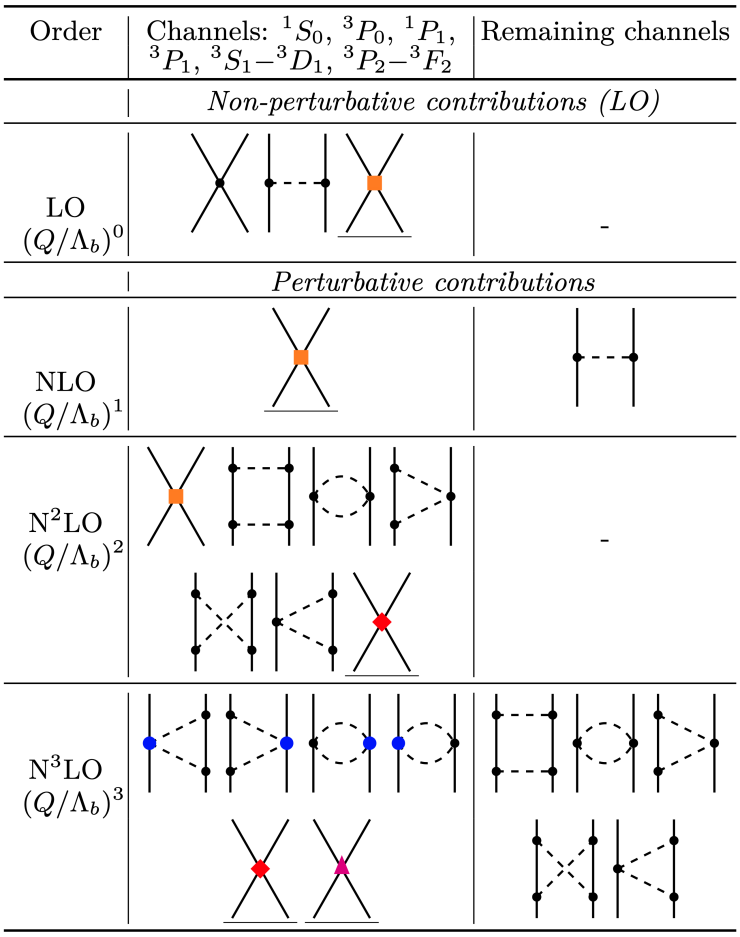

Figure 3.2: Diagrammatic representation of the contributions to the NN force in the modified PC employed in this thesis. Black dots, blue circles, orange squares, red diamonds, and pink triangles denote vertices with interaction index $\Delta_i = 0, 1, 2, 4, 6$, respectively. Underlined diagrams are promoted compared to WPC. All contributions beyond LO are treated perturbatively.

(i) The chiral orders of the irreducible pion-exchange diagrams, along with their necessary counterterms, follow WPC (see Chapter 2).

(ii) All corrections to the potential beyond LO are included perturbatively.

(iii) Counterterms are promoted to lower chiral orders when needed to fulfill the requirement of RG invariance.

By analyzing the cutoff dependence for the subleading amplitudes from Eqs. (3.9) to (3.11) in the channels up to P-waves, i.e., NN channels $^1S_0$, $^3P_0$, $^1P_1$, $^3P_1$, $^3S_1$–$^3D_1$, and $^3P_2$–$^3F_2$, they identified the necessary counterterms to absorb the cutoff dependence at each order. The resulting PC for these channels is presented in the middle column of Fig. 3.2. The underlined diagrams are higher-order contact diagrams that are promoted to absorb cutoff dependence. Note

that there is a $(Q/\Lambda_b)^1$ contribution, which is an order that vanishes in WPC. This is a promoted contact interaction in the ${}^1S_0$ channel and was identified by studying the residual cutoff dependence at LO, which contains a term $\propto \Lambda^{-1}$ (that, of course, vanishes in the $\Lambda \to \infty$ limit). The residual cutoff dependence gives information on which subsequent order new LECs are expected to appear, since the residual regulator error should not exceed the EFT truncation error. The analysis in the ${}^1S_0$ channel shows that a subleading counterterm must appear at NLO and the $\nu = 2$ term $D^{(0)}_{{}^1S_0}(p'^2 + p^2)$ is promoted to NLO.

A main goal of this thesis is to apply this PC to predict and study two- and few-nucleon observables. Thus, the PC needs to be complemented in the remaining NN channels where the force is treated entirely perturbatively. The contributions in these channels are shown in the rightmost column of Fig. 3.2, where OPE now enters at NLO. We follow Ref. [82] and suppress two-pion exchanges by the same power as OPE. Note that there are no contact interactions in these channels up to N^{3}LO.

Besides the diagrams shown in Fig. 3.2, there are diagrams at N^{2}LO and N^{3}LO that provide corrections to OPE and lower-order LECs [155]. We shift subleading OPE corrections to LO, and use the renormalized value of $g_A = 1.29$. The subleading diagrams that contribute to constant shifts in the available contacts at and below the given order can be dropped in WPC, since all potential contributions up to a given order are added before calibrating the LECs. In perturbative calculations, these diagrams need to be included at their respective order. In practice, this is done via perturbative corrections to the LECs that are introduced at subsequent orders [156]. As an example, there is one LEC at LO in the ${}^1S_0$ channel, and the contact part reads $C^{(0)}_{{}^1S_0}$ (see Eq. (3.5)). At NLO, the contact potential is simply $C^{(1)}_{{}^1S_0} + D^{(0)}_{{}^1S_0}(p'^2 + p^2)$, where $C^{(1)}_{{}^1S_0}$ is the perturbative correction to $C^{(0)}_{{}^1S_0}$ and $D^{(0)}_{{}^1S_0}(p'^2 + p^2)$ is the promoted $\nu = 2$ operator shown in Fig. 3.2. This pattern continues at subsequent orders, for all channels. For a more detailed description of the PC, see Papers II and VI.

Let us summarize the important points of this section. The LO potential in Eq. (3.5) is treated non-perturbatively in NN channels: ${}^1S_0$, ${}^3P_0$, ${}^1P_1$, ${}^3P_1$, ${}^3S_1{-}{}^3D_1$ and ${}^3P_2{-}{}^3F_2$. All subleading potential contributions are treated perturbatively, and contact terms are promoted to absorb the cutoff dependence also at subleading orders, as shown in Fig. 3.2. Table 3.1 summarizes the resulting potentials from the one- and two-pion exchange, as well as contact diagrams. The dependence on the LECs $\boldsymbol{\alpha}^{(\nu)}$ is explicitly indicated. The number of LECs at LO to N^{3}LO are 4, 2, 13, and 14, respectively. Determining the values of these LECs is a crucial next step for applying this PC to make predictions of observables.

Table 3.1: Potential contributions in channels where OPE is treated non-perturbatively (column three) and perturbatively (column four). The last column shows the number of LECs that appear in the contact potential at that order. Detailed expressions for all potentials can be found in Appendix A of Paper II.

order	potential	LO chn.	perturbative chn.	Num. LECs
LO	$V^{(0)}(\boldsymbol{\alpha}^{(0)})$	$V_{1\pi}^{(0)} + V_{\rm ct}^{(0)}(\boldsymbol{\alpha}^{(0)})$	0	4
NLO	$V^{(1)}(\boldsymbol{\alpha}^{(1)})$	$V_{\rm ct}^{(1)}(\boldsymbol{\alpha}^{(1)})$	$V_{1\pi}^{(0)}$	2
N^{2}LO	$V^{(2)}(\boldsymbol{\alpha}^{(2)})$	$V_{2\pi}^{(2)} + V_{\rm ct}^{(2)}(\boldsymbol{\alpha}^{(2)})$	0	13
N^{3}LO	$V^{(3)}(\boldsymbol{\alpha}^{(3)})$	$V_{2\pi}^{(3)} + V_{\rm ct}^{(3)}(\boldsymbol{\alpha}^{(3)})$	$V_{2\pi}^{(2)}$	14

3.3 Computing neutron-proton scattering observables perturbatively

In Papers I and II, we set out to study *np* scattering observables in the PC with partly perturbative pions described in Section 3.2. The motivation for studying *np* scattering is to be able to perform a robust inference of the unknown values of the LECs, and to study if our PC can provide quantitatively accurate predictions for these observables. We focus on the strong interaction in *np* scattering, and neglect electromagnetic and isospin-breaking effects.

The description of NN scattering was introduced in Section 2.3.1. We now specifically consider *np* scattering, for which the spin scattering matrix reads

$$M^{s}_{m'_s m_s}(\boldsymbol{p}', \boldsymbol{p}) = \frac{1}{2}[M^{s(t=0)}_{m'_s m_s}(\boldsymbol{p}', \boldsymbol{p}) + M^{s(t=1)}_{m'_s m_s}(\boldsymbol{p}', \boldsymbol{p})], \tag{3.12}$$

with $M^{st}_{m'_s m_s}(\boldsymbol{p}', \boldsymbol{p})$ defined in Eq. (2.20). We equivalently parameterize the M-matrix in terms of the laboratory kinetic energy of the impinging neutron, $T_{\rm lab}$, and the c.m. scattering angle $\theta_{\rm c.m.}$ as $M^{s}_{m'_s m_s}(T_{\rm lab}, \theta_{\rm c.m.}) \equiv M^{s}_{m'_s m_s}(\boldsymbol{p}', \boldsymbol{p})$, see Eq. (2.21).

Possible *np* scattering experiments with polarized and unpolarized spins in the beam and target can conveniently be expressed using density operators. A general mixed incoming state can be written as $\rho_i = \sum_{nm} |\lambda_n\rangle \, \rho_{nm} \, \langle\lambda_m|$, where $\{|\lambda_n\rangle\} = \{|m_1, m_2\rangle \,,\ (m_1, m_2) = \pm\frac{1}{2}\}$ denotes the uncoupled NN spin basis. The outgoing spin density matrix at a given scattering energy and angle is then

$$\rho_f = \boldsymbol{M}(T_{\rm lab}, \theta_{\rm c.m.}) \rho_i \boldsymbol{M}^{\dagger}(T_{\rm lab}, \theta_{\rm c.m.}), \tag{3.13}$$

where $\boldsymbol{M}(T_{\rm lab}, \theta_{\rm c.m.})$ denotes the 4×4 spin scattering matrix which can be expressed in terms of the matrix elements in Eq. (3.12).

The spin-averaged differential cross section can be expressed as [140]

$$\frac{d\sigma}{d\Omega} = \frac{\mathrm{Tr}\left(\rho_f\right)}{\mathrm{Tr}\left(\rho_i\right)} = \frac{1}{4}\,\mathrm{Tr}\left(\boldsymbol{M}\boldsymbol{M}^\dagger\right), \tag{3.14}$$

and the expectation value of a spin observable, $\mathcal{O}$, in the outgoing state reads

$$\langle\mathcal{O}\rangle = \frac{\mathrm{Tr}\left(\rho_f\mathcal{O}\right)}{\mathrm{Tr}(\rho_f)} = \frac{\mathrm{Tr}\left(\boldsymbol{M}\rho_i\boldsymbol{M}^\dagger\mathcal{O}\right)}{\mathrm{Tr}\left(\boldsymbol{M}\rho_i\boldsymbol{M}^\dagger\right)}. \tag{3.15}$$

By considering possible basis states for ρ_i and $\mathcal{O}$, together with parity conservation, time-reversal invariance, and the Pauli principle, one is left with 25 independent experiments [157]. Two important classes of observables are spin-polarization and spin-correlation observables. Specific examples are the dimensionless observables P_b and A_{yy}, defined as

$$\frac{d\sigma}{d\Omega}\times P_b = \frac{1}{4}\,\mathrm{Tr}\big\{\boldsymbol{M}\boldsymbol{\sigma}_{1n}\boldsymbol{M}^\dagger\big\}, \quad \frac{d\sigma}{d\Omega}\times A_{yy} = \frac{1}{4}\,\mathrm{Tr}\big\{\boldsymbol{M}\boldsymbol{\sigma}_{1n}\boldsymbol{\sigma}_{2n}\boldsymbol{M}^\dagger\big\}, \tag{3.16}$$

where $\boldsymbol{\sigma}_{in} \equiv \boldsymbol{\sigma}_i\cdot\hat{\boldsymbol{n}}$ and $\hat{\boldsymbol{n}}$ is normal to the scattering xz-plane [157]. The observable P_b shows the asymmetry in the differential cross section induced by polarizing one nucleon, while A_{yy} measures the spin-correlation induced by the scattering process.

To calculate the various scattering observables, we must solve the dynamics of the scattering process and construct $\boldsymbol{M}$. It is convenient to solve the scattering problem in a partial wave basis with partial wave states $|p\ell sj\rangle$ introduced as

$$\langle p'\ell sjm_jtm_t|\boldsymbol{p}sm_stm_t\rangle = i^\ell\,(2\pi)^{3/2}\,\frac{\delta(p'-p)}{p^2}C^{jm_j}_{\ell(m_j-m_s),sm_s}Y^{*\ell}_{m_j-m_s}(\hat{\boldsymbol{p}}). \tag{3.17}$$

where $C^{jm}_{j_1m_1,j_2m_2}$ and $Y^\ell_m(\hat{\boldsymbol{p}})$ denote Clebsch-Gordan coefficients and spherical harmonics, respectively. The projection quantum numbers m_j and m_t, associated with the j and t, are set to zero by rotational and isospin invariance, respectively, and are dropped from the notation. We consider fully antisymmetrized partial wave states, and for the np system, this means that t is fixed by ℓ and s through the Pauli principle $(-1)^{\ell+s+t} = -1$ and can also be dropped from the notation.

The spin scattering matrix in Eq. (3.12) can be expressed in terms of partial wave amplitudes as

$$\begin{aligned} M^s_{m'_sm_s}(T_{\mathrm{lab}},\theta_{\mathrm{c.m.}}) = \frac{\sqrt{\pi}}{ik}\sum_{j,\ell,\ell'} & i^{\ell-\ell'}(2j+1)\sqrt{2\ell+1} \\ & \times \begin{pmatrix} \ell' & s & j \\ m_s-m'_s & m'_s & -m_s \end{pmatrix}\begin{pmatrix} \ell & s & j \\ 0 & m_s & -m_s \end{pmatrix} \\ & \times Y^{\ell'}_{m_s-m'_s}(\theta_{\mathrm{c.m.}},0)\left(S^{js}_{\ell'\ell}(k)-\delta_{\ell'\ell}\right), \end{aligned} \tag{3.18}$$

where the matrices denote Wigner $3j$-symbols and the sum over j, ℓ', and ℓ is taken with respect to the spin-coupling rules and truncated at some $j_{\max}$. One generally needs higher $j_{\max}$ for larger $T_{\rm lab}$. For np scattering, $j_{\max} = 15$ is usually enough to obtain convergence up to $T_{\rm lab} = 200$ MeV. The partial-wave S-matrix is denoted $S^{js}_{\ell'\ell}$. In uncoupled channels (where $\ell' = \ell$) it is a unitary one-by-one matrix that can be parameterized by a real phase shift δ as

$$S^{js}_{\ell\ell} = e^{2i\delta}. \tag{3.19}$$

In coupled channels, the orbital angular momenta take the possible values $\ell' = j \pm 1$, $\ell = j \pm 1$, and the 2×2 unitary matrix can be parameterized in terms of three real phase shifts: δ_1, δ_2, and ε using the Stapp convention [158]

$$\begin{pmatrix} S^{js}_{\ell'=j-1,\ell=j-1} & S^{js}_{\ell'=j-1,\ell=j+1} \\ S^{js}_{\ell'=j+1,\ell=j-1} & S^{js}_{\ell'=j+1,\ell=j+1} \end{pmatrix} = \begin{pmatrix} \cos(2\varepsilon)e^{2i\delta_1} & i\sin(2\varepsilon)e^{i(\delta_1+\delta_2)} \\ i\sin(2\varepsilon)e^{i(\delta_1+\delta_2)} & \cos(2\varepsilon)e^{2i\delta_2} \end{pmatrix}. \tag{3.20}$$

The partial wave S-matrix for a given on-shell momentum, k, is computed from the on-shell T-matrix contributions up to the given order

$$S^{(\nu)js}_{\ell'\ell}(k) = \delta_{\ell'\ell} - i\pi m_N k \times \sum_{n=0}^{\nu} T^{(n)js}_{\ell'\ell}(k,k) \tag{3.21}$$

where $T^{(\nu)js}_{\ell'\ell}(p',p) \equiv \langle p'\ell' sj|T^{(\nu)}|p\ell sj\rangle$. The LO partial-wave T-matrix elements are obtained by solving the partial-wave LS equation

$$T^{(0)js}_{\ell'\ell}(p',k) = V^{(0)js}_{\ell'\ell}(p',k) + \sum_{\ell''} \int_0^\infty dq\; q^2\; V^{(0)js}_{\ell'\ell''}(p',q) \frac{m_N}{k^2 - q^2 + i\epsilon} T^{(0)js}_{\ell''\ell}(q,k), \tag{3.22}$$

for on-shell momentum k, where the partial wave matrix elements of the potential $V^{(\nu)js}_{\ell'\ell}(p',p) = \langle p'\ell' sj|V^{(\nu)}|p\ell sj\rangle$ can be computed using the helicity formalism [159]. The amplitudes, $T^{(\nu>0)js}_{\ell'\ell}$, are computed perturbatively from Eqs. (3.9) to (3.11) and all resulting integral equations are solved numerically using Gauss-Legendre quadrature [160, 161]. The typical number of discretization points for converged results is of the order 100. The numerical methods are described in detail in Appendix B of Paper II.

3.4 Neutron-proton scattering at leading order

When performing perturbative computations, the subleading orders only bring corrections on top of the LO result. In an EFT, all predictions naturally carry an uncertainty related to the truncation error, which is largest at LO. This means that the starting point for the perturbative expansion is only partially

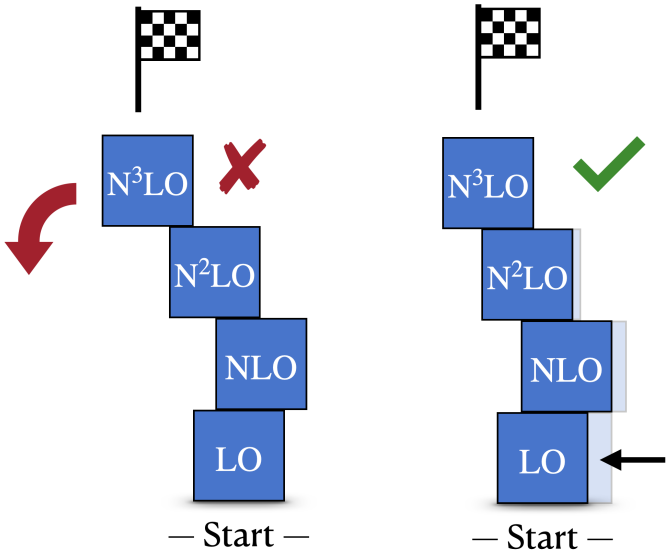

Figure 3.3: Perturbative computations can be illustrated as building a tower. The goal can only be reached if the starting point (LO) is sufficiently close to it.

constrained, and some starting points may be more successful than others. This is illustrated in Fig. 3.3, where a perturbative EFT calculation can be depicted as building a tower. This analogy shows that the starting point needs to be sufficiently close to the goal for the tower not to fall, i.e., LO needs to be able to be corrected perturbatively.

In Paper I, we quantify the possible LO interactions by inferring its LECs from *np* scattering observables, accounting for both experimental and EFT truncation uncertainties. The inference is carried out in a Bayesian framework across a wide range of cutoffs. The theoretical truncation error can naturally be extracted from the EFT expansion in Eq. (2.1) by partitioning the observable, y, into the theoretical prediction $y_{\text{th}}^{(\nu)}$ and truncation error $\delta y_{\text{th}}^{(\nu)}$ as

$$y = y_{\text{th}}^{(\nu)} + y_0 \sum_{n=\nu+1}^{\infty} c_n \left(\frac{Q}{\Lambda_b}\right)^n = y_{\text{th}}^{(\nu)} + \delta y_{\text{th}}^{(\nu)}. \tag{3.23}$$

Here, y_0 denotes a natural scale and $\{c_n\}_n$ are dimensionless expansion coefficients [35, 37, 162]. The leading truncation error scales as $(Q/\Lambda_b)^{\nu+1}$, which explicitly captures the fact that χEFT is more accurate for $Q \ll \Lambda_b$. This can naturally be incorporated in a likelihood of observing an experimental datum for a given order in the EFT

$$\text{pr}\left(y_{\text{exp}}|\boldsymbol{\alpha}^{(\nu)}, I\right) \sim \mathcal{N}\left(y_{\text{th}}^{(\nu)}\left(\boldsymbol{\alpha}^{(\nu)}\right), \sigma_{\text{th}}^2 + \sigma_{\text{exp}}^2\right), \tag{3.24}$$

where $\mathcal{N}\left(\mu, \sigma^2\right)$ is a normal distribution with mean μ and variance σ^2, $\text{pr}\left(\cdot\right)$ is the probability density function (pdf) and I denotes additional information or

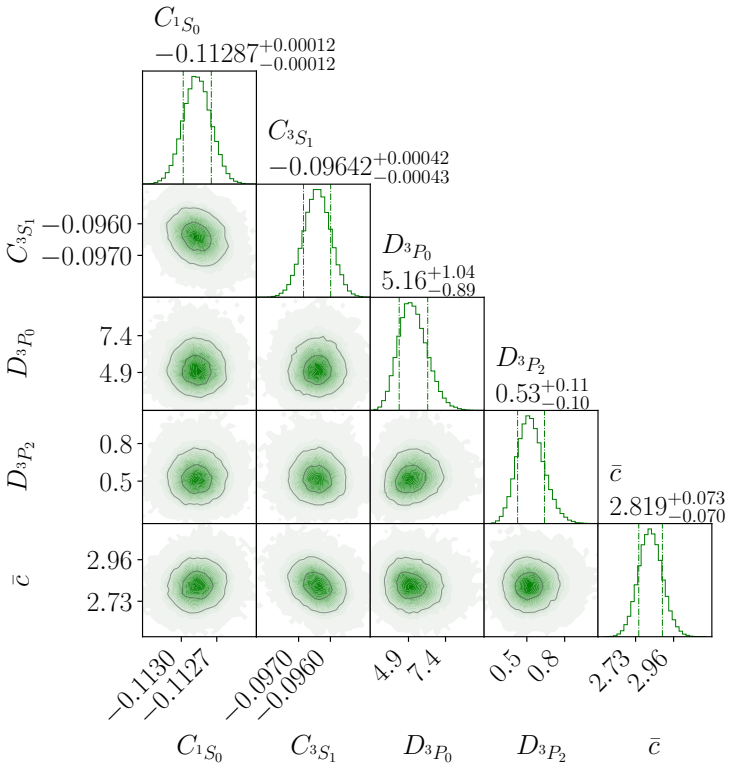

Figure 3.4: Posterior pdf for the parameters $\boldsymbol{\theta} = (\boldsymbol{\alpha}^{(0)}, \bar{c})$ for cutoff $\Lambda = 450$ MeV. The units of the LECs are $10^4 \times \text{GeV}^{-2}$ and $10^4 \times \text{GeV}^{-4}$ for the S- and P-waves, respectively. The median and the 68% equal-tailed credible interval are indicated for the marginal pdfs. The parameter $\bar{c}$ is a hyperparameter of the error model characterizing the size of σ_{th}. (Reprinted from Ref. [163].)

assumptions. For example, in Eq. (3.24) we assume that the experimental and EFT truncation errors, described by variances σ^2_{exp} and σ^2_{th}, are uncorrelated, where the latter can be computed from $\delta y^{(\nu)}_{\text{th}}$ given certain assumptions about $\{c_n\}_n$, see Paper I.

To capture the fact that LECs carry an inherent uncertainty, they are naturally described by random variables. The posterior pdf for the LECs can be related to the likelihood of observing a data set $D = \{y_{\text{exp},n}\}_n$ using Bayes' rule

$$\text{pr}\left(\boldsymbol{\alpha}^{(0)}|D, I\right) = \frac{\text{pr}\left(D|\boldsymbol{\alpha}^{(0)}, I\right) \cdot \text{pr}\left(\boldsymbol{\alpha}^{(0)}|I\right)}{\text{pr}\left(D|I\right)}. \tag{3.25}$$

Here, $\text{pr}\left(\boldsymbol{\alpha}^{(0)}|I\right)$ denotes the *prior* and $\text{pr}\left(D|I\right)$ the *model evidence* which here serves as a normalization factor. Using Eq. (3.25) one naturally incorporates the prior information of LECs through $\text{pr}\left(\boldsymbol{\alpha}^{(0)}|I\right)$, for example naturalness [164]. In Paper I we assume that the EFT truncation errors for all observables are independent, which means that the likelihood for the full data set, $\text{pr}(D|\boldsymbol{\alpha}^{(0)}, I)$,

is the product of the individual likelihoods for each datum. It is possible to relax this assumption and explore correlated truncation errors, see Refs. [40, 165, 166].

We compute the LEC posterior pdfs in Eq. (3.25) for cutoffs $\Lambda = 400$ MeV to $\Lambda = 4000$ MeV by identifying non-implausible domains using History Matching [57, 167–169] followed by Markov chain Monte Carlo (MCMC) sampling. Figure 3.4 shows the posterior pdf for the cutoff $\Lambda = 450$ MeV. The parameter $\bar{c}$ is also included, which parameterizes the size of the EFT truncation error. We demonstrate that the inference method introduced in Paper I can handle the limit-cycle-like behavior induced by singular LO potentials, leading to a rapid cutoff dependence in the LECs. This provides a basis for applying Bayesian inference schemes in modified PC frameworks across a wide range of cutoffs and at higher orders. We also validate the inference by computing posterior predictive distributions for phase shifts and various *np* scattering observables.

3.5 Neutron-proton scattering at subleading orders

In Paper II we extend the study of *np* scattering observables to subleading orders. We first develop a computational framework for perturbative computing *np* scattering observables up to N^{3}LO. As a first step, we employ a simpler method to calibrate the LECs compared to Paper I. We follow the procedure used in Refs. [90–92] and calibrate the LECs to reproduce selected *np* scattering phase shifts from Ref. [103]. Once the 33 different LECs in the potentials up to N^{3}LO are fixed, we predict *np* scattering observables and study the cutoff dependence.

The most important result of Paper II is summarized in Fig. 3.5. The figure shows predictions for a selected set of *np* scattering observables, see Eqs. (3.14) and (3.16). The bands in the figure indicate the residual cutoff variation, showing computations for $\Lambda = 500$ MeV and $\Lambda = 2500$ MeV. The residual cutoff variation can provide a useful indication of the expected size of the EFT truncation error, as discussed in Section 3.2.3. We observe a reduced cutoff dependence and an improved description of the experimental data when the chiral order is increased. This establishes that our PC with perturbative subleading orders provides a realistic description of *np* scattering observables, at least up to $T_{\text{lab}} \lesssim 100$ MeV.

We also study unitarity aspects in perturbative calculations, where the partial-wave S-matrix in Eq. (3.21) fulfills unitarity only perturbatively. This can be most easily seen by considering an uncoupled channel, with the quantum numbers suppressed from the notation. The partial-wave S-matrix computed

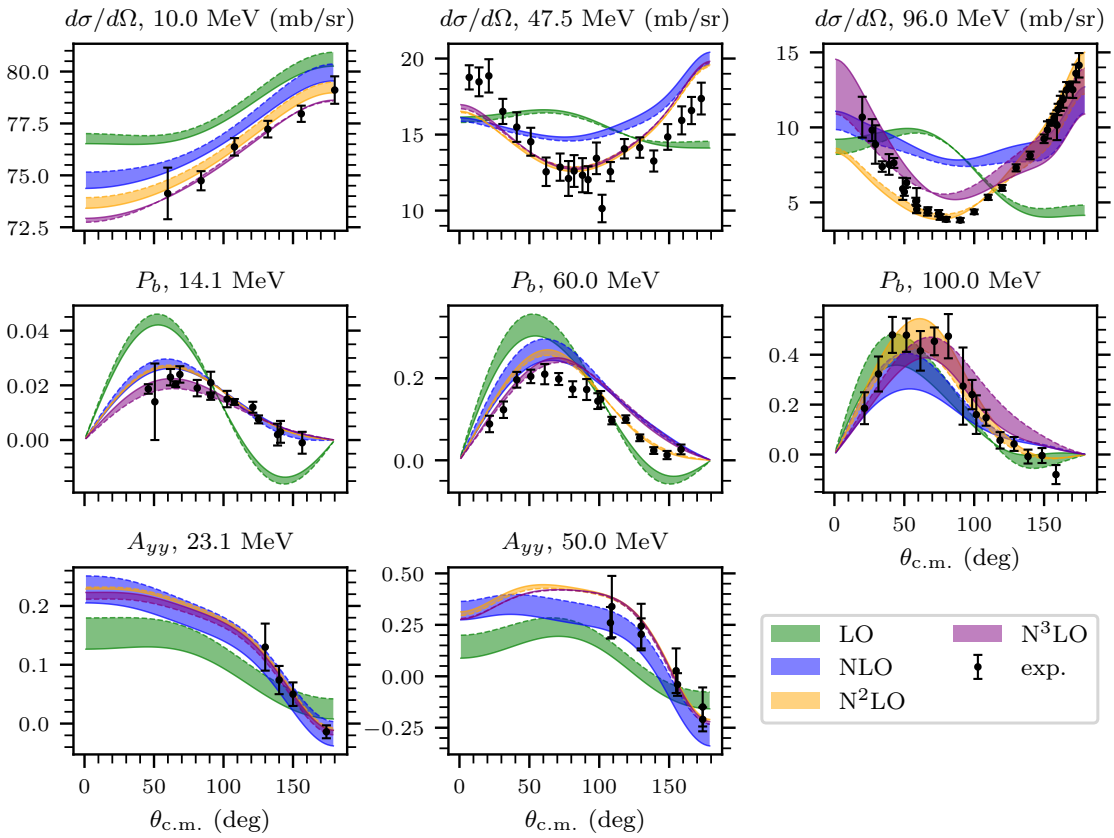

Figure 3.5: Predicted np scattering observables for energies $T_{\text{lab}} = 10$ to 100 MeV up to N^{3}LO together with experimental data (exp.) from Refs. [170, 171]. The bands show cutoff variation between $\Lambda = 500$ MeV (dashed line) and $\Lambda = 2500$ MeV (solid line). (Reprinted from Ref. [156].)

to all orders is assumed to satisfy unitarity, which gives

$$\begin{aligned} 1 = S^\dagger S &= \left(1 + \rho_T \sum_{n=0}^{\infty} T^{(n)\dagger}\right)\left(1 - \rho_T \sum_{n=0}^{\infty} T^{(n)}\right) \\ &= 1 - \rho_T \sum_{\nu=0}^{\infty}\left[T^{(\nu)} - T^{(\nu)\dagger} + \rho_T \sum_{n=0}^{\nu} T^{(n)\dagger} T^{(\nu-n)}\right] \end{aligned} \tag{3.26}$$

where $\rho_T = i\pi m_N k$. Perturbative unitarity guarantees that the terms in the bracket $[\dots]$ cancel for each value of ν, which we also verify numerically. For $\nu = 0$, one recovers the optical theorem, and for $\nu > 0$, the complex phase of $T^{(\nu)}$ is constrained from the amplitudes $T^{(n)}$ for $n < \nu$. It is apparent that $S^{(\nu)js}_{\ell'\ell}$, as defined in Eq. (3.21), does not fulfill unitarity in the sense $S^{(\nu)\dagger}S^{(\nu)} = 1 + \mathcal{O}[(Q/\Lambda_b)^{\nu+1}] \neq 1$, since the truncation to a finite order gives incomplete expressions in the bracket in Eq. (3.26) that no longer vanish. This small unitary breaking has consequences when computing np observables. For example, the

optical theorem for the total cross section is no longer exact since it assumes unitarity. Instead, the discrepancy between the total cross section computed using the optical theorem and integration of the differential cross section gives a quantitative measure of the unitary breaking. We investigate this in Paper II and confirm the expected decrease of unitary breaking with increased order. This unitary breaking is not considered problematic, since its effects are not greater than the EFT error.

3.6 Low-energy theorems and isospin breaking

The promising results for *np* scattering up to N^{3}LO presented in Papers I and II indicate that our PC with partly perturbative pions can be a candidate for an RG-invariant EFT description of the nuclear force. Another early attempt to resolve the renormalization issues caused by the OPE was proposed by Kaplan et al. [75, 76] (in papers known as KSW), where pions are treated entirely perturbatively in all NN partial waves. The KSW scheme saw some success in describing scattering phase shifts, although with a very limited improvement in the radius of convergence compared to a pionless theory [77]. Cohen and Hansen [78, 79] further investigated KSW counting by studying the S-wave effective range expansion (ERE) for *np* scattering. Their analysis pinpointed inconsistencies in the treatment of the long-range part of the force. In Paper III, I show that these inconsistencies do not appear in our PC with partly perturbative pions.

The on-shell scattering amplitude for uncoupled S-wave channels can be expressed as

$$T(k,k) = -\frac{2}{\pi m_N}\frac{1}{F(k) - ik}. \tag{3.27}$$

where $F(k)$ is analytic in k^2 near the origin with the expansion [5]

$$F(k) \equiv k\cot\delta\left(k\right) = -\frac{1}{a} + \frac{1}{2}rk^2 + v_2k^4 + v_3k^6 + v_4k^8 + \mathcal{O}\left(k^{10}\right). \tag{3.28}$$

The parameters a and r are the scattering length and effective range, while v_2, v_3 and v_4 are referred to as shape parameters. In Ref. [78], it was shown that the shape parameters in KSW counting are functions of: the scattering length, nucleon mass, and the parameters defining the pion-exchange potential. By calibrating the LECs to reproduce the empirical scattering lengths, the shape parameters are predicted solely by the long-range part of the interaction. Such predictions of ERE parameters are referred to as LETs [78, 79]. Cohen and Hansen compared the LETs with empirical ERE parameters extracted from the Nijmegen partial-wave analysis [103], where the latter provides a high-precision parameterization of the low-energy behavior of the nuclear force [172]. The agreement in this comparison was poor, even though realistic phase shifts were

observed [75, 76]. The valuable conclusion of this analysis is that LETs serve as a sensitive test of whether the long-range part of the interaction induces a correct energy dependence in the scattering amplitude.

Following Ref. [78], LETs have been used as a tool to study the low-energy properties of EFT potentials [25, 102, 173–176] and Ref. [177] showed that LETs computed in WPC are in good agreement with empirical ERE parameters. In Paper III, I study LETs for our PC with partly perturbative pions. For the uncoupled ${}^1S_0$ channel, ERE parameters are computed perturbatively from the scattering amplitudes $T^{(\nu)}$ by expanding Eq. (3.27) up to N^{3}LO

$$F(k) - ik = -\frac{2}{\pi m_N T^{(0)}} \left[1 - \frac{T^{(1)}}{T^{(0)}} + \left(\left[\frac{T^{(1)}}{T^{(0)}} \right]^2 - \frac{T^{(2)}}{T^{(0)}} \right) + \right.$$
$$\left. + \left(2 \frac{T^{(1)} T^{(2)}}{\left(T^{(0)}\right)^2} - \frac{T^{(3)}}{T^{(0)}} - \left[\frac{T^{(1)}}{T^{(0)}} \right]^3 \right) + \mathcal{O}\left(\frac{Q^4}{\Lambda_b^4} \right) \right]. \tag{3.29}$$

Contributions to the ERE at each order are identified as $F^{(0)}(k) = -\beta(k) + ik$, $F^{(1)}(k) = \beta(k) T^{(1)}/T^{(0)}$, and so on, for $\beta(k) = 2/(\pi m_N T^{(0)})$. Note that in a theory with pions, the radius of convergence for the ERE is given by $k < m_\pi/2 \approx 69$ MeV ($T_{\text{lab}} \lesssim 10$ MeV) corresponding to the first left-hand cut in the scattering amplitude caused by OPE [175].

The LECs up to N^{3}LO are calibrated using empirical phase shifts and scattering lengths. Table 3.2 shows predicted LETs up to N^{3}LO together with LETs from KSW and WPC. I also gauge the impact of including the leading isospin breaking in the OPE potential. This breaking is induced by the mass difference of neutral and charged pions $|m_{\pi^0} - m_{\pi^\pm}| = 4.6$ MeV [110], which is referred to as charge-independence breaking (CIB) in Table 3.2. Both with and without CIB, we observe a large improvement compared to KSW. By including CIB, the LETs in our PC become consistent with empirical ERE parameters and WPC. It is interesting to see that the LETs in the ${}^1S_0$ channel show a relatively high sensitivity to this CIB. For most quantities CIB only provides a small correction [123]. The description of phase shifts is also studied, as shown in Fig. 3.6. This is done to confirm that a simultaneous description of ERE parameters and phase shifts is achieved. It is also noted that the cutoff dependence in the LETs is negligible.

I also study the coupled ${}^3S_1 - {}^3D_1$ channel and the LETs for the ${}^3S_1$ partial wave. This is entirely analogous but slightly more involved, as described in Paper III. A good description of both phase shifts and LETs is found also in this case, where CIB is now a much smaller effect that does not need to be considered. In summary, the analysis in Paper III demonstrates that our PC with partly perturbative pions retains a correct near-threshold behavior and does not suffer the same issues as a fully perturbative treatment of pion interactions.

Table 3.2: LETs for the $^1S_0$ partial wave, both without and with leading CIB. The corresponding phase shifts are shown in Fig. 3.6. The parameters marked with a star ($*$) are used in the inference of the LECs and are not predicted. The quoted errors are only from the numerical extraction of the ERE parameters from Eq. (3.29). Empirical ERE parameters together with predictions from KSW and WPC are also shown.

	a [fm]	r [fm]	v_2 [fm^3]	v_3 [fm^5]	v_4 [fm^7]
Empirical [172]	−23.735(16)	2.68(3)	−0.48(2)	3.9(1)	−19.6(5)
NLO KSW [78]	$*$	$*$	−3.3	18	−108
N^{2}LO WPC [177]	−23.936	2.73	−0.46	3.8	−19.1
$\Lambda = 500$ MeV					
LO	$*$	1.71(0)	−1.77(0)	8.54(0)	−47.0(3)
NLO	$*$	$*$	−0.64(0)	4.79(0)	−29.9(2)
N^{2}LO	$*$	2.72(0)	−0.71(0)	5.05(0)	−29.3(2)
N^{3}LO	$*$	2.69(0)	−0.66(0)	5.42(0)	−31.0(2)
LO (CIB)	$*$	1.68(0)	−1.55(0)	6.63(0)	−31.64(8)
NLO (CIB)	$*$	$*$	−0.45(0)	3.42(0)	−18.95(8)
N^{2}LO (CIB)	$*$	2.70(0)	−0.55(0)	3.77(0)	−18.8(2)
N^{3}LO (CIB)	$*$	2.68(0)	−0.50(0)	4.02(0)	−19.8(2)

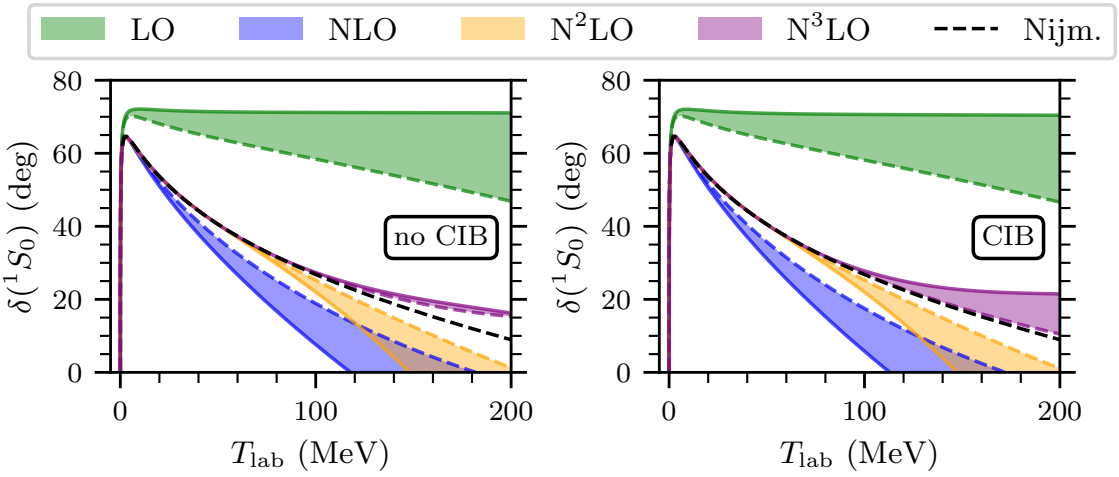

Figure 3.6: Phase shifts in the $^1S_0$ partial wave as a function of laboratory scattering energy $T_{\rm lab}$. The left (right) panel shows results without (with) CIB in the OPE potential, see Paper III. The bands show the cutoff variation for $\Lambda = 500$ MeV (dashed line) and $\Lambda = 2500$ MeV (solid line). The black dashed line shows phase shifts from Ref. [103]. (Reprinted from Ref. [178].)

Chapter 4

Accidental symmetries and spin entanglement

We have seen in Chapter 2 that the nuclear force is constrained by the low-energy symmetries of QCD, and in particular by the approximate chiral symmetry. In Chapter 3 we introduced the additional constraint of RG invariance and showed how one arrives at a modified PC with partly perturbative pions. Before extending the study of this PC to few-nucleon systems, we further explore symmetries in the nuclear interaction. In particular, we will study how Wigner SU(4) symmetry can be quantified through the spin entanglement generated in NN scattering. The implications of the work presented in this chapter will also be discussed in relation to the perturbative computational framework developed in this thesis.

4.1 Wigner SU(4) symmetry in the nuclear interaction

Including more information when constructing nuclear interaction models can yield more robust predictions. This is indeed observed when introducing the chiral symmetry and going from phenomenological high-precision potentials to potentials derived from χEFT. The chiral symmetry not only provides a systematic EFT expansion scheme with a connection to QCD, but also gives nuclear interactions that match the accuracy of phenomenological models but with fewer unknown parameters [179].

In contrast to explicitly considered symmetries, there are also emerging (accidental) ones, such as Wigner's SU(4) symmetry. Inspired by the charge independence hypothesis, Wigner [180] and Hund [181] independently proposed a symmetry in which the nuclear force is assumed to be independent of both

isospin and ordinary spin. This is mathematically formulated as invariance under SU(4) transformations acting on the multiplet of the neutron and proton spin states $[p\uparrow,\ p\downarrow,\ n\uparrow,\ n\downarrow]^{\mathrm{T}}$. Note that this invariance provides stronger constraints than the subgroup of independent spin- and isospin symmetry. An SU(4) invariant interaction can depend only on the spatial coordinates of the nucleons, thereby giving identical interactions in NN partial waves with the same orbital angular momentum

$$\left({}^1S_0, {}^3S_1\right),\ \left({}^1P_1, {}^3P_{0,1,2}\right),\ \left({}^1D_2, {}^3D_{1,2,3}\right),\ \ldots \tag{4.1}$$

Wigner's SU(4) symmetry manifests in several contexts in low-energy nuclear physics [182–184]. Two pronounced examples are the structure of light nuclei [185] and β-decay rates [186, 187]. However, the SU(4) symmetry seems to be significantly broken already in the NN S-wave interaction. This can be seen in the left panel of Fig. 4.1, which shows the substantially different ${}^1S_0$ and ${}^3S_1$ phase shifts. The physics of the singlet and triplet channels is indeed very different, with a shallow virtual state in the singlet and a bound state in the triplet. This raises the question of why SU(4) symmetry emerges in light nuclei, where S-wave interactions are known to have a dominant role. The emerging symmetry can be understood as a consequence of fine-tuning in the nuclear interaction, with singlet and triplet scattering lengths $a_s = -23.7$ fm and $a_t = 5.4$ fm being unnaturally large compared to the interaction range $R \approx m_\pi^{-1} = 1.4$ fm. This places the nuclear interaction close to the unitary limit, which is formally defined by $a_s^{-1} = a_t^{-1} = 0$. Wigner's SU(4) symmetry naturally appears near the unitary limit in low-energy NN scattering, as shown in Ref. [188] using pionless EFT. This EFT is valid for c.m. momenta $k < \Lambda_\pi \sim m_\pi$, where also the pion can be integrated out, yielding an effective theory involving only low-energy nucleons [73, 74]. Its breakdown scale is denoted by Λ_π [189]. The LO expression for the scattering amplitude in both the singlet and triplet channels in pionless EFT is given by

$$T(k,k) = \frac{2}{\pi m_N}\frac{1}{1/a + ik}, \tag{4.2}$$

where higher-order S–D mixing is neglected. It can be seen that both the singlet and triplet scattering amplitudes reduce to $T \approx 2/(\pi m_N i k)$ for $k \in [a_t^{-1}, \Lambda_\pi]$, consistent with the expectation of SU(4) symmetry. Note that the two S-wave amplitudes remain different for $k \lesssim a_t^{-1} \approx 36$ MeV, as will become apparent in the next section.

Studies of light nuclei have been performed expanding the interaction around the unitary and SU(4) symmetric limit in pionless EFT [190–192] up to NLO, with promising results. Wigner SU(4) symmetric interactions are also considered at LO in nuclear Lattice EFT computations [183, 185, 193], which is beneficial to reduce the fermion sign problem in the Monte Carlo simulations.

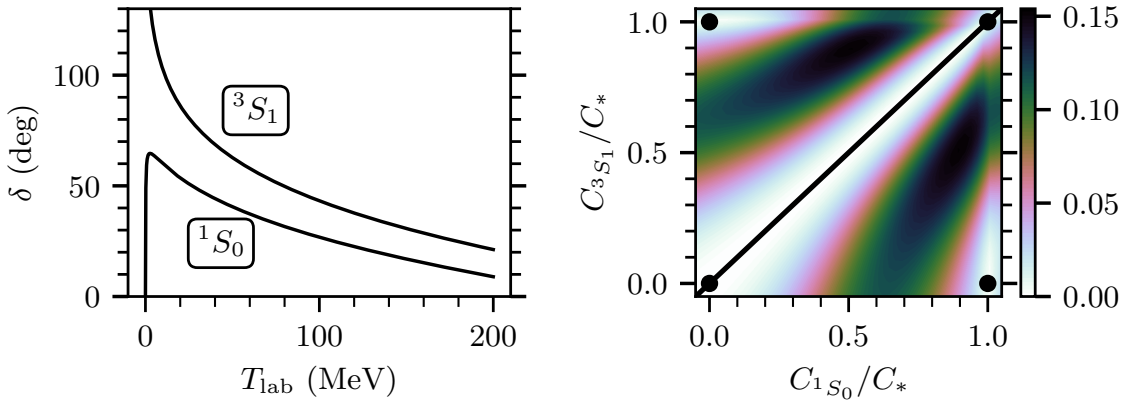

Figure 4.1: The left panel shows the S-wave phase shifts as a function of laboratory scattering energy from the Nijmegen partial-wave analysis [103]. The right panel shows the entanglement power of the S-matrix at LO in pionless EFT averaged over $k \in [0, m_\pi/2]$. The partial-wave coupling constants are expressed in terms of the critical coupling for unitary scattering, C_*. (Result reproduced from Ref. [195].)

While emerging SU(4) symmetry can be attributed to the proximity to the unitary limit, its fundamental origin in the nuclear force is less established. The large-N_c limit of QCD (where N_c is the number of colors) can provide a part of the explanation. The spin-isospin structure of leading contributions to the nuclear force in this limit are given by $V^{(0)}_{N_c} = V_C + \boldsymbol{\sigma}_1 \cdot \boldsymbol{\sigma}_2 \boldsymbol{\tau}_1 \cdot \boldsymbol{\tau}_2 W_S + S_{12} \boldsymbol{\tau}_1 \cdot \boldsymbol{\tau}_2 W_T$, where S_{12} is the tensor operator [194]. This structure breaks SU(4) symmetry in all NN partial waves. However, if one considers interactions at low-energy ($k \lesssim m_\pi$), mainly S-waves contribute.[1] The matrix element of the tensor operator vanishes in both the $^1S_0$ and $^3S_1$ partial waves, while $\boldsymbol{\sigma}_1 \cdot \boldsymbol{\sigma}_2 \boldsymbol{\tau}_1 \cdot \boldsymbol{\tau}_2 = -3$ in both cases. As a result, low-energy SU(4) symmetry is predicted in $V^{(0)}_{N_c}$.

Beane et al. [195] highlighted the connection between emerging symmetries in the strong interaction and the induced spin entanglement in S-wave np scattering. They identified the emergence of SU(4) (and SU(16) in the three-quark-flavor case) symmetries with minimal spin entanglement, and proposed the principle of entanglement suppression as a dynamical property of QCD that can explain the origin of these symmetries. The connection between entanglement suppression and SU(4) symmetry is illustrated in the right panel of Fig. 4.1, which shows a measure of the induced spin entanglement in S-wave np scattering at LO in pionless EFT. The diagonal line shows where the two S-wave LECs take the same value, giving identical interactions. The identical S-wave

[1] This can be understood as follows. The strength of the centrifugal barrier at the range of the potential, $R = m_\pi^{-1}$, is $\ell(\ell+1)/R^2$. A momentum of $k^2 \approx \ell(\ell+1)/R^2$ is needed to overcome this barrier and penetrate the region of non-zero interaction. This means that the force is heavily S-wave ($\ell = 0$) dominated for energies where $k < R^{-1}$, which correspond to $T_{\rm lab} < 40$ MeV.

interactions result in exact SU(4) symmetry and no entanglement. The circles correspond to conformal fixed points, which also show entanglement suppression [195]. Entanglement suppression connected to emergent symmetries was further studied in Refs. [196–199], and was recently applied to charged lepton scattering in the Standard Model to extract the value of the weak mixing angle [200].

4.2 Spin entanglement in two-nucleon scattering

There have been several works considering entanglement properties in NN scattering in recent years [196–198, 201–212], where the first studies of entanglement in *np* scattering using realistic potentials was performed in Refs. [204, 213]. In Paper V, we follow Ref. [195] and further study the connection between SU(4) symmetry and spin entanglement in NN scattering using realistic potentials from χEFT, where we go beyond the S-wave approximation. The aim is to quantitatively identify how entanglement is generated in scattering processes and to assess its usefulness as a probe of symmetry breaking in a nuclear interaction.

Some fundamental elements of NN scattering were introduced in Chapters 2 and 3. In particular, we remind the reader of the relation between the ingoing and outgoing NN spin state for non-forward scattering angles ($\theta_{\text{c.m.}} \neq 0$) expressed using the $\boldsymbol{M}$-matrix, see Eq. (3.13). We will only consider pure initial states, $|\chi_{\text{in}}\rangle$, for which the normalized final state reads

$$|\chi_{\text{out}}\rangle = \frac{\boldsymbol{M}\,|\chi_{\text{in}}\rangle}{\sqrt{\langle\chi_{\text{in}}|\boldsymbol{M}^\dagger\boldsymbol{M}|\chi_{\text{in}}\rangle}}. \tag{4.3}$$

We now consider the entanglement created in the NN scattering process from an initially unentangled spin state. A pure bipartite state is unentangled if and only if it can be written as a tensor product $|\chi_{\text{in}}\rangle = |\chi_1\rangle \otimes |\chi_2\rangle$, where 1 and 2 enumerate the two spin-$\frac{1}{2}$ nucleons. The final scattering state $|\chi_{\text{out}}\rangle \propto \boldsymbol{M}\,|\chi_{\text{in}}\rangle$ is also pure, but possibly entangled — which means that it cannot be written as a product state. We follow Ref. [195] and use the two-entropy

$$\mathcal{E}_{2\text{E}}(|\chi_{\text{out}}\rangle) = 1 - \text{Tr}_1\,\rho_1^2 \tag{4.4}$$

to quantify the entanglement in the final state, where $\rho_1 = \text{Tr}_2\,|\chi_{\text{out}}\rangle\langle\chi_{\text{out}}|$ is the reduced density matrix for nucleon one. The range of the two-entropy is $0 \leq \mathcal{E}_{2\text{E}} \leq 1/2$ and it attains its minimal (maximal) value for unentangled (maximally entangled) states.

The amount of entanglement in the final state $|\chi_{\text{out}}\rangle$ depends on the given kinematical setup, as well as the initial state $|\chi_{\text{in}}\rangle$. It is useful to define a measure that quantifies the entanglement produced by the scattering process,

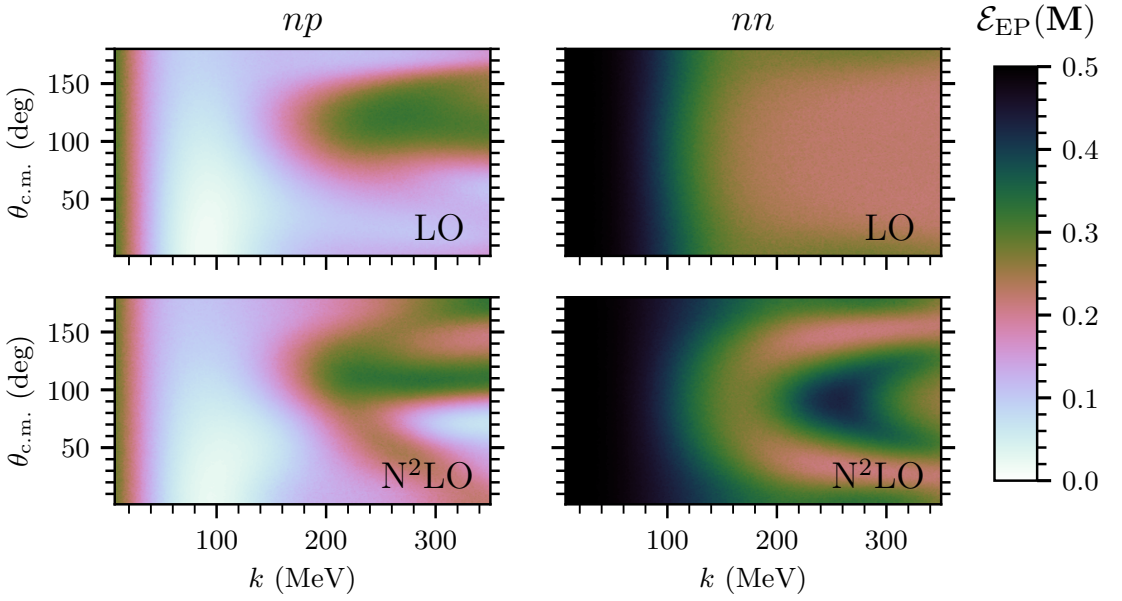

Figure 4.2: Entanglement power of the $\boldsymbol{M}$-matrix $\mathcal{E}_{\mathrm{EP}}(\boldsymbol{M})$ for the np system (left) and the nn system (right). We employ the WPC potentials from Ref. [34]. (Reprinted from Ref. [221].)

i.e., a measure of entanglement caused by the operator $\boldsymbol{M}$. One such measure is the *entanglement power* [195, 214], which is defined as the two-entropy averaged over all initial unentangled tensor product states

$$\mathcal{E}_{\mathrm{EP}}(\boldsymbol{M}) \equiv \overline{\mathcal{E}_{\mathrm{2E}}(\boldsymbol{M}\,|\chi_{\mathrm{in}}\rangle)}. \tag{4.5}$$

Other pure-state entanglement measures can also be used as a basis for the entanglement power, see, e.g., Ref. [203]. This treatment of spin entanglement is used for both the np and neutron-neutron (nn) cases, where the latter system of identical particles can be treated as *effectively distinguishable* [215–220] in the asymptotic states of the scattering process.

In Paper V, we first consider np scattering and investigate the relation between scattering-induced spin entanglement and SU(4) symmetry in χEFT. We begin by considering the LO WPC potential $V^{(0)}_{\mathrm{WPC}} = V^{(0)}_{1\pi} + C_S + C_T \boldsymbol{\sigma}_1 \cdot \boldsymbol{\sigma}_2$ (see Eqs. (2.24) and (2.25)) and its entanglement power is displayed in the top left panel of Fig. 4.2. This potential is not SU(4) symmetric, but SU(4) symmetry can be enforced in the contact part by letting $C_T = 0$, and in $V^{(0)}_{1\pi}$ by excluding the tensor force and only including even-parity partial waves. We construct five variants of the LO potential with various degrees of SU(4) symmetry to investigate the impact on the resulting entanglement. From this analysis, we identify that the entanglement for $k < a_t^{-1}$ arises from a non-zero C_T, while the tensor force in OPE (and in particular in even-parity partial waves) is the

main contributor to entanglement in the region $k > m_\pi$. We note that entanglement suppression for $k \in [a_t^{-1}, m_\pi]$ is also observed with χEFT interactions. The results from this analysis are consistent with the conclusions of the previous section regarding the relation between SU(4) breaking and the S-wave scattering lengths. We also note that an entirely SU(4) symmetric interaction produces no spin entanglement in np scattering.[2]

We continue to study the evolution of the entanglement power as we increase the chiral order, and now consider both np and nn scattering. In this (and only this) paper, we employ WPC, and in particular the interactions from Ref. [34]. We compute the entanglement power up to N^{2}LO, and also compare with results for the Nijmegen I potential [103]. The resulting entanglement power for LO and N^{2}LO is shown in Fig. 4.2. We note in Paper V that the N^{2}LO and Nijmegen I results are nearly indistinguishable. We observe that the entanglement power up to $k \approx 150$ MeV is already accurately captured at LO, and that the $k \in [a_t^{-1}, m_\pi]$ region of entanglement suppression in np scattering survives as the chiral order is increased. A significantly lower entanglement is observed in the case of np scattering, compared to nn scattering. This can be attributed to the presence (absence) of approximate SU(4) symmetry in the np (nn) system, respectively. The near-maximal low-energy entanglement observed in the nn case can be explained by the fact that they are identical particles. The S-wave dominance for $k < m_\pi$ forces the spin part of the final wave function to a maximally entangled spin-singlet state due to the Pauli principle. Our results for nn scattering are confirmed by the similar study of proton-proton scattering [223], which specifically emphasizes the emergence of maximally entangled spin states relevant for nuclear Bell tests [224, 225].

The quantitative results for different interactions presented in Paper V strengthen the connection between SU(4) symmetry and spin-entanglement suppression, which can be relevant for understanding entanglement in many-nucleon systems [226–231]. We show that the SU(4) properties of the interaction are directly related to the resulting entanglement, thereby yielding an energy-resolved probe of the symmetries of the potential. This entanglement-based approach may be more useful than directly comparing the magnitudes of potential terms with different symmetry structures [195]. Extending this work to higher orders, and combining it with the framework for adding sub-leading corrections perturbatively, provides a natural path to further studying (approximate) SU(4) symmetry also at higher orders in χEFT. Specifically, PCs around symmetric or mostly symmetric LO forces can naturally be investigated.

[2]This might seem obvious, since an SU(4) symmetric potential acts trivially on the spin state. Note, however, the similar case where a spin-independent potential can induce non-zero spin entanglement in the case of two *identical* fermions through the Pauli principle [222].

Chapter 5

Predicting binding energies in light nuclei

In this chapter, we apply the PC with partly perturbative pions developed in Chapter 3 to study light nuclei. We will start by investigating the ground-state energy of ^{3}H using the NCSM, and then move on to compute ground-state energies of ^{4}He and ^{6}Li. The key development presented in this chapter is the advancement of perturbative many-body computations, which enables us to apply our PC with partly perturbative pions up to N^{3}LO for $A \leq 6$ systems.

5.1 The no-core shell model

The Hamiltonian governing a system of A non-relativistic nucleons reads

$$H = \sum_{i=1}^{A} \frac{\boldsymbol{P}_i^2}{2m_N} + \sum_{i<j=1}^{A} V_{ij} + \ldots, \tag{5.1}$$

where $\boldsymbol{P}_i$ is the momentum of nucleon i expressed in the laboratory frame, V_{ij} is the NN potential between nucleons i and j, and the ellipsis denotes three- and many-body forces which we neglect in our studies. The Hamiltonian in Eq. (5.1) includes both the relative motion of the nucleons and the motion of their c.m. By subtracting the c.m. kinetic energy from H one obtains the following Hamiltonian for the intrinsic motion of the nucleons

$$H_{\text{int}} = \frac{1}{A} \sum_{i<j=1}^{A} \frac{(\boldsymbol{p}_i - \boldsymbol{p}_j)^2}{2m_N} + \sum_{i<j=1}^{A} V_{ij}, \tag{5.2}$$

where the intrinsic kinetic energy will be denoted T_{int}. The intrinsic Hamiltonian is Galilean invariant, and we can choose to express it in the c.m. frame

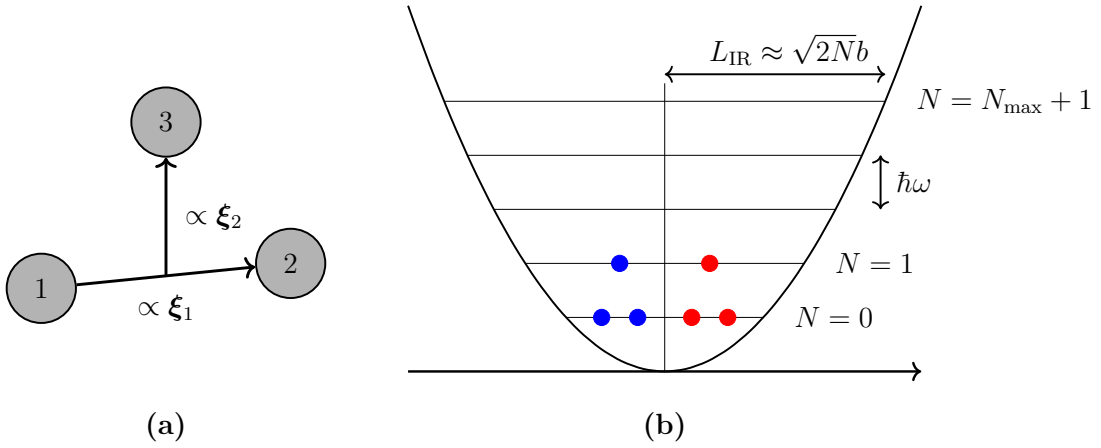

Figure 5.1: (a) A system of three nucleons described by Jacobi coordinates $\boldsymbol{\xi}_1$ and $\boldsymbol{\xi}_2$. **(b)** Illustration of the lowest Pauli-allowed configuration neutrons (left) and protons (right) in the ground state of ^{6}Li in a basis of eigenstates of the harmonic oscillator.

($\sum_i \boldsymbol{P}_i = 0$) where we denote the particle momenta as $\boldsymbol{p}_i$. We are interested in solving the time-independent Schrödinger equation for H_{int},

$$H_{\mathrm{int}} \left|\Psi_{\mathrm{int}}\right\rangle = E \left|\Psi_{\mathrm{int}}\right\rangle , \tag{5.3}$$

which describes the stationary quantum states of the A-body system.

One natural way to solve Eq. (5.3) is to expand it in a suitable large, but finite, A-body basis, which results in an eigenvalue problem. One such method is the NCSM [47], which was applied in pioneering studies of light nuclei from microscopic descriptions of the NN force [232, 233]. The exponential complexity in mass number limits the application of the NCSM to relatively light nuclei. Higher mass numbers, all the way up to ^{208,266}Pb [57, 58], can be reached with a variety of other many-body methods that employ more efficient truncation schemes and controlled approximations to achieve polynomial scaling in A, see, e.g., Ref. [52]. All these many-body methods can be used to predict nuclear properties directly from microscopic descriptions of the nuclear force, and are commonly referred to as *ab initio* [51, 234] methods.

It is natural to express Eq. (5.3) in relative (Jacobi) coordinates, where ^{3}H is exemplified in Fig. 5.1a. Natural basis states read $|\boldsymbol{\xi}_1\rangle \otimes |\boldsymbol{\xi}_2\rangle \otimes |(s\tfrac{1}{2})Sm_S\rangle \otimes |(t\tfrac{1}{2})Tm_T\rangle$, where $\boldsymbol{\xi}_1$ and $\boldsymbol{\xi}_2$ are the Jacobi coordinates. Furthermore, s and t denote the spin and isospin of the subsystem consisting of nucleons (12), while S and T, with associated projections m_S and m_T, are the total spin and isospin for the three-nucleon system. The two Jacobi coordinates can be expanded in eigenfunctions of the spherical harmonic oscillator (HO) $|n\ell m_\ell\rangle$ and $|\mathcal{N}\mathcal{L}m_\mathcal{L}\rangle$, respectively, where $\langle\boldsymbol{\xi}_1|n\ell m_\ell\rangle = R_{n\ell}(\xi_1; b) \times Y^\ell_{m_\ell}(\hat{\boldsymbol{\xi}}_1)$ (and analogously for $\boldsymbol{\xi}_2$). The length parameter $b = (m_N\omega)^{-1/2}$ is related to the HO frequency ω. By

recoupling angular momenta and dropping superfluous quantum numbers, a three-body basis with well-defined total angular momentum, parity, and isospin (J^Π, T) can be constructed [232]

$$|n\ell sjt, \mathcal{N}\mathcal{L}\mathcal{J}; JT\rangle \equiv |n\mathcal{N}(\ell s)j(\mathcal{L}\frac{1}{2})\mathcal{J}; (j\mathcal{J})Jm_J\rangle \otimes |(t\frac{1}{2})Tm_T\rangle\,. \tag{5.4}$$

The total angular momenta above are defined as follows: j for the (12) subsystem, $\mathcal{J}$ for nucleon 3 relative to the center of mass for (12), and J for the full three-nucleon system. The states in Eq. (5.4) are not fully antisymmetric; however, the (12) subsystem becomes antisymmetric by enforcing the condition $(-1)^{\ell+s+t} = -1$. Fully antisymmetric states $\{|\Gamma\rangle\}$ are constructed from the states in Eq. (5.4) as eigenstates of the three-particle antisymmetrizer with eigenvalue one [232]. The most common basis truncation is to limit the total energy quanta of the oscillators $N \leq N_{\max}$, where $N \equiv 2n+\ell+2\mathcal{N}+\mathcal{L}$. The details of the basis construction for the three-nucleon system in the Jacobi-coordinate NCSM (J-NCSM) are presented in Appendix A.

The computational complexity of the antisymmetrization limits the application of the Jacobi-coordinate approach to relatively low values of $A \lesssim 4$, above which it is more efficient to directly solve Eq. (5.1) in a basis of Slater determinants of single-nucleon states [47]. In the latter approach, antisymmetrization is trivial, at the cost of an enlarged basis size, where no coupling to good J and T is considered. Diagonalization can still be performed in these larger bases, using iterative algorithms such as Lanczos [235].

The lowest Pauli-allowed configuration of occupied single-nucleon states for ^{6}Li is illustrated in Fig. 5.1b. The unique feature of the HO basis is that there is no mixing between the internal and c.m. excitations if the Slater determinant basis is truncated to contain excitations of $N_{\max}$ energy quanta above the lowest Pauli-allowed configuration (N_0), i.e., $\sum_{i=1}^{A}(2n_i + \ell_i) \leq N_{\max} + N_0$ [47]. For example, $N_0 = 1$ for ^{6}Li. Since this truncation does not mix internal and c.m. excitations, the relevant states of the H_{int} can be identified as the eigenstates of Eq. (5.1) with the c.m. in the ground state.[1] The c.m. is constrained to its ground state in calculations by adding a Lawson term to the Hamiltonian that pushes c.m. excitations higher up in the spectrum [237].

Describing the A-nucleon system in a finite basis naturally introduces infrared and ultraviolet scales L_{IR} and Λ_{UV} that characterize the basis limits of resolution. For the considered system, the basis parameters $N_{\max}$ and ω need to be chosen such that convergence is achieved in both scales

$$L_{\text{IR}} \approx \sqrt{2N_{\max}}b \gg R_{\text{sys}}, \quad \Lambda_{\text{UV}} \approx \sqrt{2N_{\max}}b^{-1} \gg \Lambda, \tag{5.5}$$

[1] For general basis states, or other truncation schemes, this factorization does not hold, and the intrinsic eigenstates will suffer from c.m. contamination. Other many-body methods generally have this contamination, which needs to be under control, see, e.g., Ref. [236].

where R_{sys} is the system size and Λ is the momentum cutoff employed in the regulated potential, see also Fig. 5.1. The expressions for L_{IR} and Λ_{UV} quoted above hold for $N_{\text{max}} \gg 1$, while more accurate expressions can be derived, see Ref. [238]. The only possibility to simultaneously reach convergence in both scales is to increase the basis size through N_{max}. Arbitrarily large bases are not achievable in numerical computations, which is the fundamental reason why the NCSM (and many-body methods in general) effectively only can be applied for interaction potentials with relatively low cutoffs, Λ.

5.2 Perturbative computations in ^{3}H and exceptional cutoffs

To assess whether our PC with partly perturbative pions, introduced in Section 3.2, can provide realistic descriptions of nuclear observables, it is essential to (*i*) construct interactions to a non-trivial chiral order (Papers I and II), and to (*ii*) develop computational frameworks for computing few- and many-body nuclear observables (Papers IV and VI). In this section, we describe the first perturbative ground-state energy computations of ^{3}H in the NCSM at N^{2}LO. This will also be the first time exceptional cutoffs [96] manifest beyond the NN system.

5.2.1 Rayleigh-Schrödinger perturbation theory in ^{3}H

In Paper IV we primarily study the ground-state energy of ^{3}H, where the perturbative corrections are implemented using the Rayleigh-Schrödinger formulation. For this purpose, a J-NCSM code `py-ncsm` [239] was developed. This code is open source and freely available. As discussed in the previous section, the HO basis used in the NCSM naturally limits the accessible cutoffs. A more efficient method for studying cutoffs beyond ~ 1 GeV is to use the Faddeev equations [105, 191, 240, 241]. We still employ the NCSM because it can be extended to higher-mass nuclei. Furthermore, ^{3}H is a suitable non-trivial system for benchmarking the perturbative computational framework we develop.

At LO we solve the Schrödinger equation non-perturbatively for the intrinsic Hamiltonian $H_{\text{int}}^{(0)} = T_{\text{int}} + V^{(0)}$, where we employ the NN interaction from Paper II. We construct fully antisymmetric basis states $\{|\Gamma\rangle\}$ with the quantum numbers of the ^{3}H ground state $(J^\Pi, T) = (\frac{1}{2}^+, \frac{1}{2})$ and solve

$$\sum_{\Gamma'} \langle\Gamma|\, H_{\text{int}}^{(0)}\, |\Gamma'\rangle \, \langle\Gamma'|\Psi_n^{(0)}\rangle = E_n^{(0)} \, \langle\Gamma|\Psi_n^{(0)}\rangle \,. \tag{5.6}$$

We consider basis truncations up to $N_{\text{max}} = 46$, for which the size of the partially- and fully-antisymmetric basis is 19 000 and 6 336, respectively, and the

full LO spectrum $\{|\Psi_n^{(0)}\rangle\,, E_n^{(0)}\}_n$ can be obtained. By first assuring convergence in $\Lambda_{\rm UV}$ and performing extrapolation in $L_{\rm IR}$ [238], we can investigate cutoffs up to $\Lambda \approx 1500$ MeV at LO. We verify that the ground-state energy appears to reach a plateau as a function of the cutoff Λ, consistent with Ref. [105].

Spurious deeply bound NN states with $|E_{\rm gs}| \approx 200 - 1000$ MeV appear in the $^3P_0$ and $^3S_1{-}^3D_1$ channels for cutoffs $\Lambda > 679$ MeV (see Paper I). These unphysical states need to be projected out of the NN spectrum before computing properties of ^{3}H. This is done using the technique of orthogonalizing pseudopotentials [70, 105, 242] by applying the transformation

$$V^{(0)} \to V^{(0)} + \sum_{\phi} \lambda_\phi \,|\phi\rangle\,\langle\phi|\,, \tag{5.7}$$

where $|\phi\rangle$ denotes a spurious state, and λ_ϕ is a positive constant of order 10^8 MeV. We show in Paper IV that this procedure removes the effect of spurious states both at leading and subleading orders.

Subleading corrections to the ground-state energy are computed by implementing Rayleigh-Schrödinger perturbation theory, which up to N^{3}LO reads

$$E_0^{(1)} = \langle\Psi_0|V^{(1)}|\Psi_0\rangle\,, \tag{5.8}$$

$$E_0^{(2)} = \langle\Psi_0|V^{(2)}|\Psi_0\rangle + \sum_{k\neq 0} \frac{|\,\langle\Psi_0|V^{(1)}|\Psi_k\rangle\,|^2}{E_0^{(0)} - E_k^{(0)}}, \tag{5.9}$$

$$\begin{aligned} E_0^{(3)} &= \langle\Psi_0|V^{(3)}|\Psi_0\rangle \\ &\quad + 2\sum_{k\neq 0} \frac{\langle\Psi_0|V^{(2)}|\Psi_k\rangle\,\langle\Psi_k|V^{(1)}|\Psi_0\rangle}{E_0^{(0)} - E_k^{(0)}} \\ &\quad + \sum_{k\neq 0}\sum_{m\neq 0} \frac{\langle\Psi_0|V^{(1)}|\Psi_k\rangle\,\langle\Psi_k|V^{(1)}|\Psi_m\rangle\,\langle\Psi_m|V^{(1)}|\Psi_0\rangle}{(E_0^{(0)} - E_k^{(0)})(E_0^{(0)} - E_m^{(0)})} \\ &\quad - \langle\Psi_0|V^{(1)}|\Psi_0\rangle \sum_{k\neq 0} \frac{|\,\langle\Psi_0|V^{(1)}|\Psi_k\rangle\,|^2}{\left(E_0^{(0)} - E_k^{(0)}\right)^2}, \end{aligned} \tag{5.10}$$

where $|\Psi_n\rangle \equiv |\Psi_n^{(0)}\rangle$. Despite the presence of energy denominators of the form $(E_0^{(0)} - E_m^{(0)})$, contributions from highly excited states are not significantly suppressed. The full numerical spectrum generally needs to be included in the sums of Eqs. (5.9) and (5.10). The ground-state energy at N$^\nu$LO is given by adding the contributions $\sum_{k=0}^{\nu} E_0^{(k)}$, and the corresponding predictions up to N^{2}LO are shown in Fig. 5.2. We investigate the model-space convergence for $N_{\rm max} \leq 46$ and HO frequencies $\omega \in [10\text{ MeV}, 125\text{ MeV}]$, for cutoffs 500 MeV $\leq \Lambda \leq$ 1560 MeV. We find converged results up to N^{2}LO for $\Lambda \lesssim 1200$ MeV. In these first N^{2}LO computations, a pronounced cutoff depen-

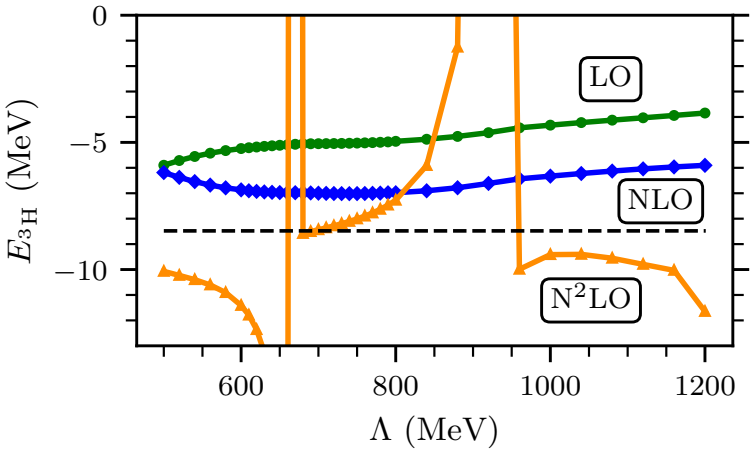

Figure 5.2: The ground-state energy of ^{3}H up to N^{2}LO computed with the J-NCSM for $N_{\max} = 46$. The HO frequency of the variational minimum at LO is used at all orders. The black dashed line shows the experimental value [243]. (Reprinted from Ref. [244].)

dence at $\Lambda \approx 670$ MeV and $\Lambda \approx 900$ MeV can be observed. The motivation and guiding principle when constructing this PC with partly perturbative pions was cutoff independence, which the N^{2}LO prediction in Fig. 5.2 clearly appears to violate. We will now see how this cutoff dependence results from so-called exceptional cutoffs and investigate strategies to remedy this behavior.

5.2.2 Origin and consequences of exceptional cutoffs

The cutoff dependence of the *np* scattering amplitude in the $^3P_0$ channel for the same PC that we employ was examined in detail in Ref. [96]. They identified narrow regions in the cutoff domain where the N^{2}LO LECs diverge. Diverging LECs is not necessarily a problem, and is a known feature at LO. Here, limit-cycle-like divergences appear due to the singular and attractive nature of the OPE tensor force [70, 81] (see also Paper I). The key difference with exceptional cutoffs is that these divergences propagate to observables, which appear to break cutoff independence beyond NLO [96]. We show that the divergences observed in Fig. 5.2 can be explained by exceptional cutoffs in the $^3P_0$ and $^3S_1$–$^3D_1$ channels by extending the analysis in Ref. [96] to coupled channels, see Appendix B in Paper IV.

The origin, meaning, and effects of exceptional cutoffs will here be discussed for the uncoupled $^3P_0$ channel, following Ref. [96], to avoid the unnecessary complication of the coupled-channel formalism. Let us remember the perturbative scattering amplitude computations from Chapter 3. Specifically, the equations for the subleading T-amplitudes Eqs. (3.9) to (3.11), and the potential expres-

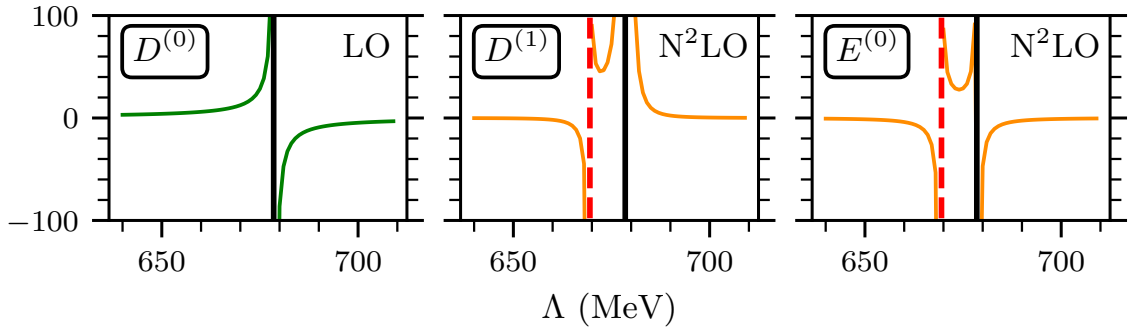

Figure 5.3: The $^3P_0$ LECs at LO and N^{2}LO as a function of the momentum cutoff, in units of $10^4 \times \mathrm{GeV}^{-4}$, $10^7 \times \mathrm{GeV}^{-4}$ and $10^6 \times \mathrm{GeV}^{-6}$, from left to right, respectively. The solid black vertical lines mark the location of limit-cycle-like cutoffs, while the dashed red lines mark the exceptional cutoff. (Adapted from Ref. [244].)

sions shown in Table 3.1. The LO amplitude in the $^3P_0$ channel is obtained by solving the partial-wave LS equation in Eq. (3.22). The NLO correction vanishes in our PC while the N^{2}LO contribution reads

$$T^{(2)} = \Omega_-^\dagger V_{2\pi}^{(2)} \Omega_+ + \Omega_-^\dagger V_{\mathrm{ct}}^{(2)} \Omega_+ \equiv T_\pi^{(2)} + T_{\mathrm{ct}}^{(2)}, \tag{5.11}$$

where the parts stemming from two-pion exchange ($V_{2\pi}^{(2)}$) and contacts ($V_{\mathrm{ct}}^{(2)}$) can be separated. The contact potential is parameterized by two LECs, here denoted $\boldsymbol{\alpha} = (D^{(1)}(\Lambda), E^{(0)}(\Lambda))$ (see Appendix A in Paper II), and can be written as [96]

$$T_{\mathrm{ct}}^{(2)}(k,k) = D^{(1)}(\Lambda)\ \psi_\Lambda^2(k) + E^{(0)}(\Lambda)\ 2\psi_\Lambda(k)\psi'_\Lambda(k). \tag{5.12}$$

The vertex functions $\psi_\Lambda(k)$ and $\psi'_\Lambda(k)$ can be expressed as derivatives of the LO radial wave function, $R^{(0)}(kr)$, at the origin[2]

$$\left.\frac{dR^{(0)}(kr)}{dr}\right|_{r=0} \propto \psi_\Lambda(k), \qquad \left.\frac{d^3R^{(0)}(kr)}{dr^3}\right|_{r=0} \propto \psi'_\Lambda(k). \tag{5.13}$$

The complex phase of these vertex functions are given by the LO $^3P_0$ phase shifts, $\delta^{(0)}(k)$, and it is convenient to introduce the real-valued functions $\bar{\psi}_\Lambda(k) \equiv \psi_\Lambda(k)e^{-i\delta^{(0)}(k)}$ and $\bar{\psi}'_\Lambda(k) \equiv \psi'_\Lambda(k)e^{-i\delta^{(0)}(k)}$.

The N^{2}LO correction to the phase shift is linear in $T^{(2)}$. By using two phase shifts at different on-shell momenta, k_1 and k_2, as renormalization conditions to constrain the two LECs, one obtains a linear system of equations

$$\begin{pmatrix} \bar{\psi}_\Lambda^2(k_1) & 2\bar{\psi}_\Lambda(k_1)\bar{\psi}'_\Lambda(k_1) \\ \bar{\psi}_\Lambda^2(k_2) & 2\bar{\psi}_\Lambda(k_2)\bar{\psi}'_\Lambda(k_2) \end{pmatrix} \boldsymbol{\alpha} = \boldsymbol{\delta}. \tag{5.14}$$

[2]Note that this identification only holds exactly if a sharp momentum cutoff is applied, see Ref. [245].

We denote the matrix above by A_Λ to indicate that it depends on the cutoff. The right-hand side, $\boldsymbol{\delta}$, involves the choice of experimental calibration phase shifts as well as phase-shift contributions from the pion part of the interaction. The exact form of $\boldsymbol{\delta}$ is not central for the argument here, for details see Paper IV. The key point is; determining subleading LECs in a PC where corrections are computed perturbatively generally involves solving a linear system of equations.[3] Crucially, the matrix A_Λ is sensitive to the LO wave function at $r \approx 0$, whose oscillatory nature for increasing cutoffs can result in $\det(A_\Lambda) \to 0$ for specific values of Λ. The determinant of A_Λ can go to zero if $\bar{\psi}_\Lambda(k) \to 0$, for all k, which happens at limit-cycle-like cutoffs where the LO LEC diverges. These zeros are benign, which is confirmed in both the case of ${}^3P_0$ [96, 245] and for ${}^3S_1{-}{}^3D_1$ in Paper IV. Importantly, the determinant can also acquire zeros where its individual matrix elements stay finite. This is what happens at the exceptional cutoffs, and the resulting divergences in the N^{2}LO LECs propagate to observables, which is detrimental for the RG invariance. Figure 5.3 shows the ${}^3P_0$ LEC values where limit-cycle-like and exceptional cutoffs are visible. In Paper IV, we can conclude that the divergence around $\Lambda = 670$ MeV in Fig. 5.2 is caused by the exceptional cutoff observed in Fig. 5.3. We also show that the limit-cycle-like divergence in the LECs at LO and N^{2}LO does not cause any divergence in the triton prediction, as expected.

Two approaches to mitigate the effects of exceptional cutoffs in the ${}^3P_0$ channel are presented in Refs. [245, 246]. Both are based on modifying the LO amplitude, and thus the matrix A_Λ. This modification is, however, kept within the allowed EFT truncation error, very much in the spirit of what is illustrated in Fig. 3.3. In Paper IV, we extend the mitigation strategy of Ref. [245] to the coupled ${}^3S_1{-}{}^3D_1$ channel, and further apply it to the ^{3}H computations. Figure 5.4 shows the predicted triton ground-state energy at N^{2}LO as a function of the cutoff, where Δ parameterizes the LO shifts applied in the ${}^3P_0$ channel. The introduced shifts effectively move the location of the exceptional cutoff, and Fig. 5.4 confirms that a divergence-free prediction can be stitched together by applying different shifts in different cutoff domains. We find, however, that the same approach does not work for the exceptional cutoff at $\Lambda \approx 900$ MeV stemming from the ${}^3S_1{-}{}^3D_1$ channel. Another mitigation strategy is likely needed in this case, and exceptional cutoffs currently hinder reliable computations of $A > 2$ observables beyond NLO for $\Lambda \gtrsim 650$ MeV. However, as seen in the deuteron computations presented in Paper IV, there are wide regions at $\Lambda \gtrsim 1500$ MeV without exceptional cutoffs, implying that the divergences can in principle be avoided by going to high cutoffs. Unfortunately, this cutoff region remains challenging to access in many-body computations, where our ^{3}H

[3] One can also apply other methods of computing subleading phase shifts from the perturbative amplitude that do not explicitly give a linear system of equations. This was also explored, but gave the same outcome regarding exceptional cutoffs as the approach presented here.

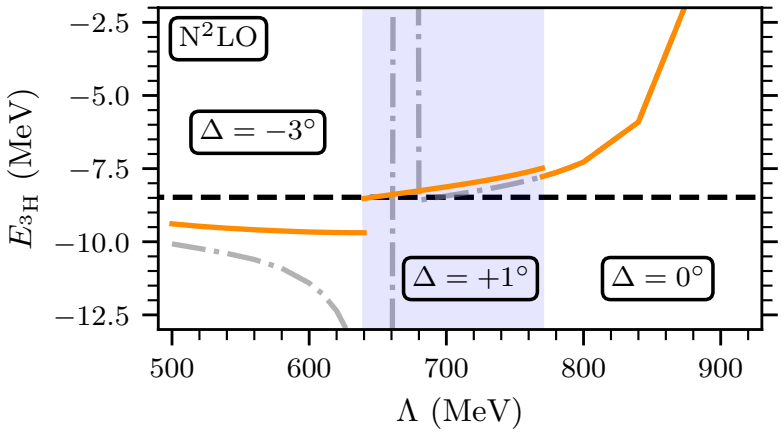

Figure 5.4: The triton ground-state energy at N^{2}LO as a function of the momentum cutoff. The orange solid lines in each cutoff region correspond to shifts $\Delta = -3°, +1°$ and $0°$, respectively, as defined in Eq. (29) in Paper IV. The gray dashed-dotted line shows the $\Delta = 0°$ result across all cutoffs. The black dashed line shows the experimental triton ground-state energy [110]. All calculations use $N_{\max} = 46$ and the HO frequency, ω, is chosen as the LO variational minimum at all orders. (Reprinted from Ref. [244].)

computations are limited to $\Lambda \lesssim 1200$ MeV.

An open question regarding the exceptional cutoffs remains: are they inherent to perturbative PC schemes or merely a mathematical artifact that can be eliminated? In Appendix A in Paper IV we show that the same pattern of "exceptional divergences" appears when considering perturbative corrections in the $^1S_0$ channel, but for increasing g_A instead of increasing Λ. This indicates that this is a mathematical problem related to the oscillatory behavior of the wave function at distances $r \lesssim \Lambda^{-1}$, and singular potentials are not a necessary condition for the problem to arise. A recent study [247] continued to analyze the impact of different regulation schemes and showed that exceptional cutoffs are tightly linked to non-local regulators at LO. It remains to be studied if applying other regulation schemes is an effective way to eliminate exceptional cutoffs in this PC.

5.3 Perturbative computations up to ^{6}Li

We saw in the previous section that exceptional cutoffs currently present a challenge for reliably computing $A > 2$ observables beyond NLO for $\Lambda \gtrsim 650$ MeV. This is an important problem to address for analyzing the cutoff dependence beyond the NN system. However, as we previously discussed, converging many-body computations beyond $\Lambda \approx 500$ MeV is already challenging. The effects of exceptional cutoffs are naturally avoided by this restriction to lower cutoff val-

ues. In Paper VI, we shift focus from RG analyses in the two- and three-nucleon systems to simultaneously advancing perturbative many-body computations in both mass number and chiral order. We focus on ^{4}He and ^{6}Li systems up to N^{3}LO and apply relatively low cutoffs, $\Lambda \leq 500$ MeV, to obtain converged many-body computations. These systems are analyzed using the M-scheme NCSM (M-NCSM) code `pANTOINE` [248–251] which employs a Slater determinant basis, discussed in Section 5.1.

5.3.1 Perturbative corrections from numerical derivatives

We show in Paper IV that the whole LO spectrum is needed when computing perturbative corrections with Rayleigh-Schrödinger perturbation theory (see Eqs. (5.9) and (5.10)). However, full diagonalization of the Hamiltonian is not feasible with M-NCSM in relevant model spaces for ^{4}He or ^{6}Li [248]. In Paper VI, we demonstrate that it is possible to instead reliably compute perturbative corrections up to N^{3}LO from numerical derivatives, without explicit knowledge of the full LO spectrum. We refer to this approach as the finite-difference (FD) method, similar to what has been applied at NLO in Refs. [106, 252]. This approach will now be described.

Let us define a Hamiltonian where we add the subleading potentials multiplied by constants $\boldsymbol{x} = (x_1, x_2, x_3) \in \mathbb{R}^3$

$$H(\boldsymbol{x}) = H^{(0)} + \sum_{\nu=1}^{3} x_\nu V^{(\nu)}, \tag{5.15}$$

where $H^{(0)} = T_{\text{int}} + V^{(0)}$ is the intrinsic LO Hamiltonian. By solving the Schrödinger equation

$$H(\boldsymbol{x}) \left|\Psi_n(\boldsymbol{x})\right\rangle = E_n(\boldsymbol{x}) \left|\Psi_n(\boldsymbol{x})\right\rangle, \tag{5.16}$$

one obtains $\boldsymbol{x}$-dependent energies and states. The energy corrections in Eqs. (5.8) to (5.10), can equivalently be expressed in terms of derivatives of $E_0(\boldsymbol{x})$. By performing a Taylor expansion and identifying the order-by-order contributions, one obtains the general expression

$$E_n^{(\nu)} = \sum_{m=1}^{\nu} \frac{1}{m!} \sum_{\substack{\alpha_1,\ldots,\alpha_m=1 \,:\\ (\alpha_1+\cdots+\alpha_m=\nu)}}^{\nu} \partial_{\alpha_1} \ldots \partial_{\alpha_m} E_n(\boldsymbol{x})|_{\boldsymbol{x}=0}, \tag{5.17}$$

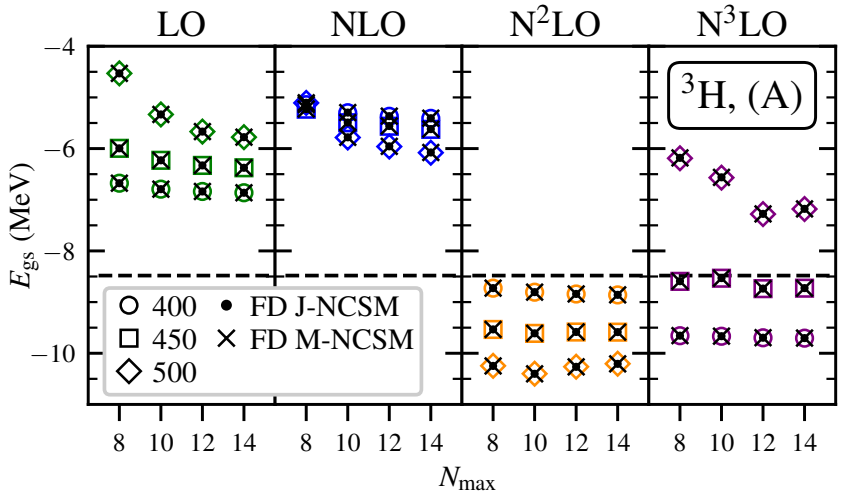

Figure 5.5: Ground-state energy of ^{3}H as a function of $N_{\max}$ up to N^{3}LO. The circles, squares, and diamonds show the exact Rayleigh-Schrödinger result for cutoffs $\Lambda = 400, 450, 500$ MeV, respectively. The interaction from Paper II is employed, here denoted as (A). The black dots (crosses) show the FD computations with the J- (M-) NCSM, respectively for a h^2 stencil, and $h = 0.06$. The dashed horizontal line shows the experimental triton ground-state energy [243]. The HO frequency $\omega = 24$ MeV is employed.

where $\partial_\alpha \equiv \frac{\partial}{\partial x_\alpha}$. The ground-state corrections explicitly read

$$\begin{aligned} E_0^{(1)} &= \partial_1 E_0(\boldsymbol{x}), \\ E_0^{(2)} &= \partial_2 E_0(\boldsymbol{x}) + \frac{1}{2}\partial_1^2 E_0(\boldsymbol{x}), \\ E_0^{(3)} &= \partial_3 E_0(\boldsymbol{x}) + \partial_1\partial_2 E_0(\boldsymbol{x}) + \frac{1}{6}\partial_1^3 E_0(\boldsymbol{x}), \end{aligned} \tag{5.18}$$

with the derivatives evaluated at $\boldsymbol{x} = 0$. These derivatives can be computed numerically. The question is; can this be done with sufficient numerical precision to accurately determine the energy corrections, considering that $E_0(\boldsymbol{x})$ is only computed approximately in a finite basis.

We employ finite-difference stencils to compute the derivatives in Eq. (5.18) [253]. If the eigenvalue, $E_0(\boldsymbol{x})$, is computed with numerical precision ϵ (e.g. $\epsilon = 10^{-7}$ for single precision) the relative error in an n:th order derivative follow the form $E_\epsilon(h) = \epsilon h^{-n} + Kh^p$, where h is the differentiation step length. The first term is the floating point round-off error, and the second is the stencil truncation error with ($p \in \mathbb{N}$, $K \in \mathbb{R}$). An optimal accuracy is obtained for a value of h that balances these two error sources. This naturally limits the accuracy for high-order derivatives. An increased accuracy can be obtained by applying higher-order stencils, but this also requires additional evaluations of

$E_0(\boldsymbol{x})$. A full N^{3}LO calculation requires 13 (31) exact diagonalizations for h^2 (h^4) stencils.

We benchmark the FD method in ^{3}H where we have access to exact Rayleigh-Schrödinger computations. Figure 5.5 shows this comparison, where we apply the FD method to ground-state energies computed with both the J- and M-NCSM. An excellent agreement is observed in both bases independently of $N_{\max}$. We present a more detailed convergence analysis in Paper VI, including how to choose an optimal value of h. For ^{4}He and ^{6}Li, there are no exact Rayleigh-Schrödinger computations to compare with, and convergence is instead confirmed by applying stencils with different truncation errors. We conclude in Paper VI that computing $E_0(\boldsymbol{x})$ with the Lanczos algorithm to single precision ($\epsilon = 10^{-7}$) is sufficient for obtaining sub-percent errors in the predictions of ^{4}He up to N^{3}LO, employing a h^2 stencil. Since we apply the same computational framework for ^{6}Li, we expect similarly-sized errors also for this system.

5.3.2 Predicted binding energies in ^{2,3}H, ^{4}He, and ^{6}Li

Having verified the FD method, we continue the study in Paper VI by examining predictions for ground-state energies in the ^{2,3}H, ^{4}He, and ^{6}Li systems. We start by employing the interaction from Paper II, which we denote by (A), in which the LECs are constrained solely by *np* phase shifts. The predicted ground-state energies for this interaction are shown in the left column of Fig. 5.6a. We observe a rather poor agreement, unnaturally large subleading corrections, and a considerable cutoff dependence in the predictions of ^{3}H, ^{4}He, and ^{6}Li, beyond NLO. Prompted by these observations, we explore how predictions for ^{4}He and ^{6}Li are impacted by conditioning the LEC calibration on the binding energies of ^{2,3}H. We limit this investigation to the S-wave LECs, since we find that the $A > 2$ ground-state energy predictions are predominantly sensitive to the LECs in the $^3S_1 - ^3D_1$ channel, and in particular to the LEC controlling the strength of the tensor interaction, and thus the mixing angle ε_1. We construct two modifications of (A) and consider interactions (A) – (C), (two additional interactions are also considered in the Appendix of Paper VI). Interactions (B) and (C) differ from (A) only in the $^1S_0$ and $^3S_1 - ^3D_1$ channels, and are identical for the remaining NN channels.

The study of different interactions is here summarized by specifically focusing on interactions (A) and (B). For interaction (B), the calibration data for the LECs in the $^3S_1 - ^3D_1$ channel additionally include the ground-state energy of ^{3}H at N^{2,3}LO and ^{2}H at N^{3}LO.[4] The predictions for interaction (B) are shown in the right column of Fig. 5.6a, where a clear improvement is observed for ^{4}He

[4]The two NLO LECs in the $^1S_0$ channel are also calibrated slightly differently compared to (A) in order to decrease the magnitude of the corrections in this channel, see Paper VI for the details.

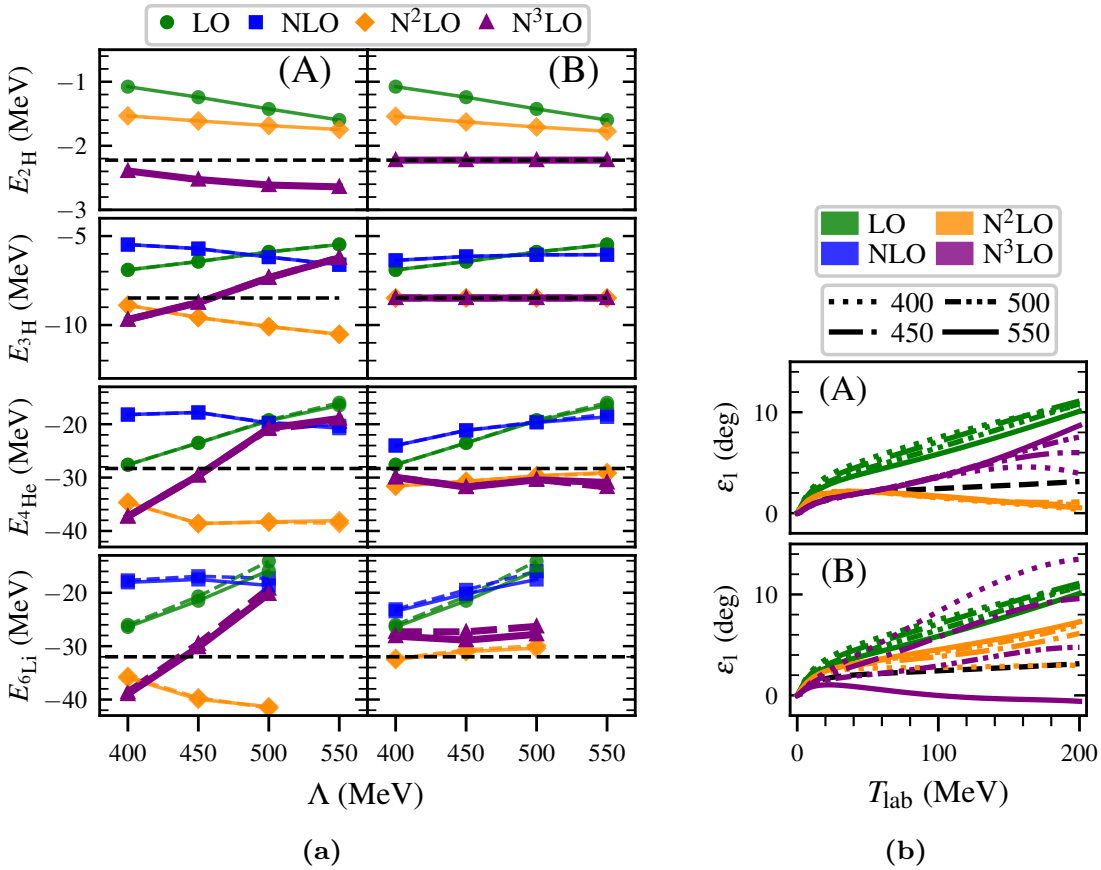

Figure 5.6: **(a)** Ground-state energies for ^{2,3}H, ^{4}He and ^{6}Li (rows) as a function of the cutoff for interaction (A) and (B), (columns). Interaction (A) is calibrated using neutron-proton phase shifts alone, while (B) additionally uses few-body input: ^{3}H at N^{2,3}LO and ^{2}H at N^{3}LO. The solid (dashed) lines show $N_{\max} = 30$ (28) for ^{3}H, $N_{\max} = 16$ (14) for ^{4}He, and $N_{\max} = 14$ (12) for ^{6}Li. The black dashed lines show the experimental values. The HO frequency $\omega = 24$ MeV was used in all computations. **(b)** The mixing angle in the $^3S_1 - ^3D_1$ channel for interaction (A) and (B) for different cutoffs and chiral orders. The black dashed lines show the mixing angle from the Nijmegen partial-wave analysis [103].

and ^{6}Li. In particular, the significant cutoff dependence for ^{4}He and ^{6}Li beyond NLO with interaction (A) is remedied.

The cutoff dependence in interaction (A) beyond NLO likely originates from the lack of three-body forces, and possibly also from the influence of exceptional cutoffs — whose effect at N^{3}LO is not yet studied even in the NN system. When interaction (B) is constructed by recalibrating the S-wave LECs to reproduce the ^{3}H ground-state energy, this two-body interaction will effectively compensate for the missing three-body physics. This naturally results in a reduced accuracy on pure NN data. This is indeed observed, where an increased cutoff dependence in the $^3S_1 - ^3D_1$ mixing angle is noted for (B), as shown in Fig. 5.6b.

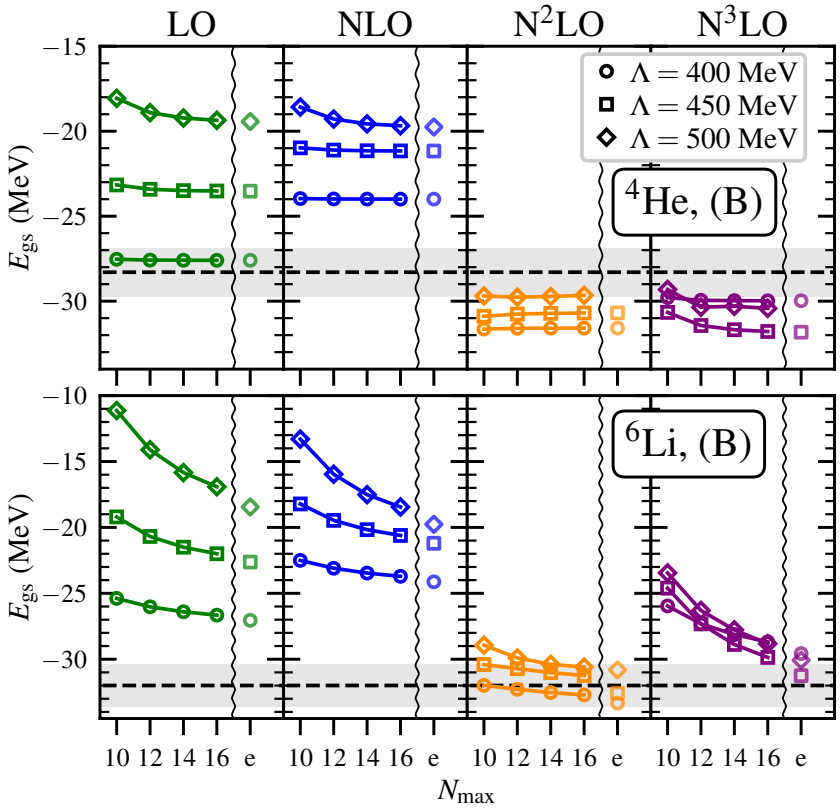

Figure 5.7: Ground-state energies of ^{4}He (top) and ^{6}Li (bottom) as a function of $N_{\max}$ up to N^{3}LO. Results for cutoffs $\Lambda = 400, 450, 500$ MeV and interaction (B) are presented. The column denoted 'e' displays an exponential extrapolation in $N_{\max}$ (where possible). The black dashed line shows the experimental ground-state energies [243] and the shaded bands ±5%. We use $h = 0.06$ with a $p = 2$ stencil and $\omega = 24$ MeV in all computations.

The magnitude of this cutoff dependence is largely influenced by our choice of calibration scheme, where we only recalibrate the LECs in the $^3S_1 - ^3D_1$ channel when including the ^{3}H ground-state energy. A recalibration of all LECs would be interesting to explore in further studies. Note that there is one important takeaway from Fig. 5.6a. When the cutoff dependence in ^{3}H is eliminated, it is also eliminated in ^{4}He and ^{6}Li. This suggests that a proper treatment of ^{3}H, including three-nucleon forces and remedying possible effects from exceptional cutoffs, will eliminate the cutoff dependence also for ^{4}He and ^{6}Li.

Another observation we make in Paper VI is that ^{6}Li is close to unbound or unbound with respect to ^{4}He+^{2}H breakup in most of the interactions. Although, the model-space convergence in ^{6}Li needs to be quantified more thoroughly. This finding is consistent with Ref. [106] and also observed at LO in WPC [254]. We speculate that a more careful calibration of the P-wave interactions, which has not been the focus of this study, is an important next step.

In Paper VI we conclude that interaction (B), where both ^{2,3}H binding energies are included in the calibration of the LECs, provides the most accurate ground-state energies for ^{4}He and ^{6}Li. Figure 5.7 shows the convergence as a function of $N_{\max}$ for predicted ^{4}He and ^{6}Li ground-state energies up to N^{3}LO for interaction (B). Well-converged energies are obtained up to N^{3}LO for ^{4}He. The convergence is marginally slower for ^{6}Li, but a precision of ≈ 1 MeV in the N^{3}LO prediction can still be obtained. This shows that converged perturbative results are achievable with basis sizes comparable to what is needed in conventional non-perturbative computations.

The results that we obtain in Paper VI demonstrate that it is possible to apply our PC with partly perturbative pions to construct NN forces that provide quantitatively accurate predictions of nuclear ground-state energies in nuclei up to ^{6}Li. This demonstrates that this class of PC schemes with a partly perturbative treatment can be an alternative to WPC for quantitatively accurate predictions in nuclei. The key development in this work is the simultaneous advancement of both chiral order and mass number, which relies on the demonstrated high accuracy of the FD method — even with a limited basis size and output precision in the computed ground-state energies. Since the FD method only relies on exact non-perturbative energies from the Schrödinger equation, we believe that this is a versatile and scalable approach that can be applied in other few- and many-body methods.

Chapter 6

Summary and concluding remarks

Describing atomic nuclei and nuclear matter from first principles using quarks and gluons is challenging due to the non-perturbative nature of the strong force at the energy scales relevant to nuclear systems. This thesis provides a comprehensive overview of how to instead apply χEFT to construct models of the strong force among effective degrees of freedom (nucleons and pions), and how to use such models to predict nuclear observables. A major advantage of EFTs is that the incorporated symmetries, together with a quantitative control of theoretical uncertainties, preserve a connection to QCD. Both the controlled uncertainties and connection to QCD are vital features for precision *ab initio* studies of nuclear observables. The most commonly employed PC to construct nuclear forces in χEFT is WPC, in which the singular pion-exchange interactions lead to an undesirable cutoff dependence in predicted observables.

This thesis investigates a modified PC with partly perturbative pions, which is constructed to explicitly incorporate RG invariance at each order. RG invariance is achieved by promoting certain counterterms, and by treating subleading interactions perturbatively. However, the need for a strictly perturbative treatment of subleading interactions adds complexity to the computational framework for solving the many-body Schrödinger equation. This is likely a contributing aspect to why perturbative PC schemes, proposed already several decades ago, have only been employed to study a limited set of nuclear observables.

The work presented in this thesis enables and extends the study of χEFT PCs that are guided by RG invariance. Specifically, we apply a version of the Long and Yang PC with partly perturbative pions. The aim of this thesis has been to study the predictive power of this PC for few-nucleon observables by developing interactions and computational frameworks up to $\mathrm{N^3LO}$. This is achieved by first studying the NN system, which is done in Papers I – III

and V. In these studies, we perform Bayesian inference of the LECs at LO and proceed to calibrate interactions up to N^{3}LO. These interactions are then employed to predict NN scattering observables and LETs. In Paper V, we also connect the symmetry properties of NN interactions to scattering-induced spin entanglement. In Papers IV and VI, we study binding energies of light nuclei (^{3}H, ^{4}He, and ^{6}Li) by performing perturbative NCSM computations up to N^{3}LO. The obtained results show that it is possible to find parameterizations of the nuclear force in the studied PC that produce quantitatively accurate predictions, for $A \leq 6$ nuclei. From the studies presented in this thesis, we conclude that the employed PC scheme based on RG invariance can be a viable alternative to WPC for constructing predictive nuclear forces in few-nucleon systems.

Key directions for future research include:

(i) Further investigation of the origin of exceptional cutoffs to devise strategies mitigating their effect, also for $A > 2$ systems. This research direction will likely include the exploration of different local regulation schemes for the potentials. Further studies of exceptional cutoffs will be important to validate the theoretical consistency of the PC studied in this thesis.

(ii) The inclusion of three-nucleon forces, Coulomb interactions, and isospin breaking. All of these subleading effects are important to advance towards more accurate *ab initio* predictions. The residual cutoff dependence observed at N^{3}LO in Paper VI indicates that a three-nucleon force is needed to renormalize the three-nucleon system at this order.

(iii) Extension of the Bayesian inference scheme to perform a simultaneous inference of the LECs at all orders from few-nucleon observables. This type of inference will likely require the development of emulators for perturbative computations to enable fast and accurate evaluations of predictions.

(iv) Utilize the developed code frameworks for computing of NN scattering observables (`nn-mwpc` [147]) and ground-state energies (`py-ncsm` [239]) in other contexts. One application is to extend the work in Paper V and use entanglement as a guide to develop and study symmetry-guided PCs, where subleading interactions can be treated perturbatively.

While this thesis demonstrates a simultaneous advancement in both chiral order and mass number, reaching N^{3}LO and ^{6}Li, these types of perturbative PCs guided by RG invariance are still far less explored than WPC. In light of the results presented in this thesis, extending perturbative computations to observables in medium-mass nuclei and beyond is a promising direction for further research.

Bibliography

[1] E. Rutherford, "The scattering of alpha and beta particles by matter and the structure of the atom", Phil. Mag. Ser. 6 **21**, 669–688 (1911).

[2] J. Chadwick, "The Existence of a Neutron", Proc. Roy. Soc. Lond. A **136**, 692–708 (1932).

[3] E. Wigner, "On the mass defect of helium", Phys. Rev. **43**, 252–257 (1933).

[4] H. Yukawa, "On the Interaction of Elementary Particles I", Proc. Phys. Math. Soc. Jap. **17**, 48–57 (1935).

[5] H. A. Bethe, "Theory of the Effective Range in Nuclear Scattering", Phys. Rev. **76**, 38–50 (1949).

[6] D. J. Gross and F. Wilczek, "Asymptotically Free Gauge Theories - I", Phys. Rev. D **8**, 3633–3652 (1973).

[7] H. D. Politzer, "Reliable Perturbative Results for Strong Interactions?", Phys. Rev. Lett. **30**, edited by J. C. Taylor, 1346–1349 (1973).

[8] H. Fritzsch, M. Gell-Mann, and H. Leutwyler, "Advantages of the Color Octet Gluon Picture", Phys. Lett. B **47**, 365–368 (1973).

[9] S. Weinberg, "Phenomenological Lagrangians", Physica A **96**, edited by S. Deser, 327–340 (1979).

[10] S. Weinberg, "Nuclear forces from chiral Lagrangians", Phys. Lett. B **251**, 288–292 (1990).

[11] S. Weinberg, "Effective chiral Lagrangians for nucleon - pion interactions and nuclear forces", Nucl. Phys. B **363**, 3–18 (1991).

[12] J. Gasser and H. Leutwyler, "Chiral perturbation theory to one loop", Annals of Physics **158**, 142–210 (1984).

[13] J. Gasser, M. E. Sainio, and A. Svarc, "Nucleons with Chiral Loops", Nucl. Phys. B **307**, 779–853 (1988).

[14] S. Scherer and M. Schindler, *A primer for chiral perturbation theory*, Lecture Notes in Physics (Springer Berlin Heidelberg, 2011).

[15] C. Ordonez and U. van Kolck, "Chiral lagrangians and nuclear forces", Phys. Lett. B **291**, 459–464 (1992).

[16] C. Ordonez, L. Ray, and U. van Kolck, "Nucleon-nucleon potential from an effective chiral Lagrangian", Phys. Rev. Lett. **72**, 1982–1985 (1994).

[17] C. Ordonez, L. Ray, and U. van Kolck, "The Two nucleon potential from chiral Lagrangians", Phys. Rev. C **53**, 2086–2105 (1996).

[18] N. Kaiser, "Chiral 3π-exchange NN potentials: Results for representation invariant classes of diagrams", Phys. Rev. C **61**, 014003 (2000).

[19] N. Kaiser, "Chiral 3π-exchange NN potentials: Results for diagrams proportional to g_A^4 and g_A^6", Phys. Rev. C **62**, 024001 (2000).

[20] N. Kaiser, "Chiral 3π-exchange NN potentials: Results for dominant next-to-leading order contributions", Phys. Rev. C **63**, 044010 (2001).

[21] N. Kaiser, "Chiral 2π-exchange NN potentials: Two loop contributions", Phys. Rev. C **64**, 057001 (2001).

[22] N. Kaiser, "Chiral 2π exchange NN potentials: Relativistic $1/M^2$ corrections", Phys. Rev. C **65**, 017001 (2002).

[23] E. Epelbaum, W. Gloeckle, and U.-G. Meissner, "Nuclear forces from chiral Lagrangians using the method of unitary transformation. 1. Formalism", Nucl. Phys. A **637**, 107–134 (1998).

[24] E. Epelbaum, W. Gloeckle, and U.-G. Meissner, "Nuclear forces from chiral Lagrangians using the method of unitary transformation. 2. The two nucleon system", Nucl. Phys. A **671**, 295–331 (2000).

[25] E. Epelbaum, W. Glockle, and U.-G. Meissner, "The Two-nucleon system at next-to-next-to-next-to-leading order", Nucl. Phys. A **747**, 362–424 (2005).

[26] E. Epelbaum, A. Nogga, W. Gloeckle, H. Kamada, U. G. Meissner, and H. Witala, "Three nucleon forces from chiral effective field theory", Phys. Rev. C **66**, 064001 (2002).

[27] D. R. Entem and R. Machleidt, "Accurate charge dependent nucleon nucleon potential at fourth order of chiral perturbation theory", Phys. Rev. C **68**, 041001 (2003).

[28] V. G. J. Stoks, R. A. M. Klomp, C. P. F. Terheggen, and J. J. de Swart, "Construction of high quality N N potential models", Phys. Rev. C **49**, 2950–2962 (1994).

[29] R. Machleidt, "The High precision, charge dependent Bonn nucleon-nucleon potential (CD-Bonn)", Phys. Rev. C **63**, 024001 (2001).

[30] A. Ekström et al., "Optimized Chiral Nucleon-Nucleon Interaction at Next-to-Next-to-Leading Order", Phys. Rev. Lett. **110**, 192502 (2013).

[31] A. Ekström, G. R. Jansen, K. A. Wendt, G. Hagen, T. Papenbrock, B. D. Carlsson, C. Forssén, M. Hjorth-Jensen, P. Navrátil, and W. Nazarewicz, "Accurate nuclear radii and binding energies from a chiral interaction", Phys. Rev. C **91**, [Erratum: Phys.Rev.C 109, 059901 (2024)], 051301 (2015).

[32] M. Hoferichter, J. Ruiz de Elvira, B. Kubis, and U.-G. Meißner, "Roy–Steiner-equation analysis of pion–nucleon scattering", Phys. Rept. **625**, 1–88 (2016).

[33] W. G. Jiang, A. Ekström, C. Forssén, G. Hagen, G. R. Jansen, and T. Papenbrock, "Accurate bulk properties of nuclei from $A = 2$ to ∞ from potentials with Δ isobars", Phys. Rev. C **102**, 054301 (2020).

[34] B. D. Carlsson, A. Ekström, C. Forssén, D. F. Strömberg, G. R. Jansen, O. Lilja, M. Lindby, B. A. Mattsson, and K. A. Wendt, "Uncertainty analysis and order-by-order optimization of chiral nuclear interactions", Phys. Rev. X **6**, 011019 (2016).

[35] R. J. Furnstahl, N. Klco, D. R. Phillips, and S. Wesolowski, "Quantifying truncation errors in effective field theory", Phys. Rev. C **92**, 024005 (2015).

[36] E. Epelbaum, H. Krebs, and U. G. Meißner, "Improved chiral nucleon-nucleon potential up to next-to-next-to-next-to-leading order", Eur. Phys. J. A **51**, 53 (2015).

[37] M. R. Schindler and D. R. Phillips, "Bayesian Methods for Parameter Estimation in Effective Field Theories", Ann. Phys. **324**, [Erratum: Ann. Phys. 324, 2051–2055 (2009)], 682–708 (2009).

[38] R. J. Furnstahl, D. R. Phillips, and S. Wesolowski, "A recipe for EFT uncertainty quantification in nuclear physics", J. Phys. G **42**, 034028 (2015).

[39] J. A. Melendez, S. Wesolowski, and R. J. Furnstahl, "Bayesian truncation errors in chiral effective field theory: nucleon-nucleon observables", Phys. Rev. C **96**, 024003 (2017).

[40] J. A. Melendez, R. J. Furnstahl, D. R. Phillips, M. T. Pratola, and S. Wesolowski, "Quantifying Correlated Truncation Errors in Effective Field Theory", Phys. Rev. C **100**, 044001 (2019).

[41] I. Svensson, A. Ekström, and C. Forssén, "Bayesian parameter estimation in chiral effective field theory using the hamiltonian monte carlo method", Phys. Rev. C **105**, 014004 (2022).

[42] I. Svensson, A. Ekström, and C. Forssén, "Bayesian estimation of the low-energy constants up to fourth order in the nucleon-nucleon sector of chiral effective field theory", Phys. Rev. C **107**, 014001 (2023).

[43] S. Wesolowski, R. J. Furnstahl, J. A. Melendez, and D. R. Phillips, "Exploring bayesian parameter estimation for chiral effective field theory using nucleon-nucleon phase shifts", J. Phys. G **46**, 045102 (2019).

[44] S. Wesolowski, I. Svensson, A. Ekström, C. Forssén, R. J. Furnstahl, J. A. Melendez, and D. R. Phillips, "Rigorous constraints on three-nucleon forces in chiral effective field theory from fast and accurate calculations of few-body observables", Phys. Rev. C **104**, 064001 (2021).

[45] D. R. Entem, N. Kaiser, R. Machleidt, and Y. Nosyk, "Dominant contributions to the nucleon-nucleon interaction at sixth order of chiral perturbation theory", Phys. Rev. C **92**, 064001 (2015).

[46] P. Reinert, H. Krebs, and E. Epelbaum, "Semilocal momentum-space regularized chiral two-nucleon potentials up to fifth order", Eur. Phys. J. A **54**, 86 (2018).

[47] B. R. Barrett, P. Navratil, and J. P. Vary, "Ab initio no core shell model", Prog. Part. Nucl. Phys. **69**, 131–181 (2013).

[48] G. Hagen, T. Papenbrock, M. Hjorth-Jensen, and D. J. Dean, "Coupled-cluster computations of atomic nuclei", Rept. Prog. Phys. **77**, 096302 (2014).

[49] A. Tichai, R. Roth, and T. Duguet, "Many-body perturbation theories for finite nuclei", Front. in Phys. **8**, 164 (2020).

[50] S. Elhatisari et al., "Wavefunction matching for solving quantum many-body problems", Nature **630**, 59–63 (2024).

[51] A. Ekström, C. Forssén, G. Hagen, G. R. Jansen, W. Jiang, and T. Papenbrock, "What is ab initio in nuclear theory?", Front. Phys. **11**, 1129094 (2023).

[52] H. Hergert, "A Guided Tour of *ab initio* Nuclear Many-Body Theory", Front. Phys. **8**, 379 (2020).

[53] G. Hagen et al., "Neutron and weak-charge distributions of the ^{48}Ca nucleus", Nature Phys. **12**, 186–190 (2015).

[54] S. Elhatisari, D. Lee, G. Rupak, E. Epelbaum, H. Krebs, T. A. Lähde, T. Luu, and U.-G. Meißner, "Ab initio alpha-alpha scattering", Nature **528**, 111 (2015).

[55] S. R. Stroberg, J. D. Holt, A. Schwenk, and J. Simonis, "Ab initio Limits of Atomic Nuclei", Phys. Rev. Lett. **126**, 022501 (2021).

[56] P. Arthuis, C. Barbieri, M. Vorabbi, and P. Finelli, "Ab initio Computation of Charge Densities for Sn and Xe Isotopes", Phys. Rev. Lett. **125**, 182501 (2020).

[57] B. Hu et al., "Ab initio predictions link the neutron skin of ^{208}Pb to nuclear forces", Nature Phys. **18**, 1196–1200 (2022).

[58] F. Bonaiti, G. Hagen, and T. Papenbrock, "Structure of the doubly magic nuclei ^{208}Pb and ^{266}Pb from ab initio computations", (2025), arXiv:2508.14217 [nucl-th].

[59] B. A. Brown, "Neutron radii in nuclei and the neutron equation of state", Phys. Rev. Lett. **85**, 5296–5299 (2000).

[60] R. Essick, I. Tews, P. Landry, and A. Schwenk, "Astrophysical Constraints on the Symmetry Energy and the Neutron Skin of Pb208 with Minimal Modeling Assumptions", Phys. Rev. Lett. **127**, 192701 (2021).

[61] J. M. Lattimer, "Neutron stars and the dense matter equation of state", Astrophys. Space Sci. **336**, 67–74 (2011).

[62] T. Dietrich, M. W. Coughlin, P. T. H. Pang, M. Bulla, J. Heinzel, L. Issa, I. Tews, and S. Antier, "Multimessenger constraints on the neutron-star equation of state and the Hubble constant", Science **370**, 1450–1453 (2020).

[63] R. Somasundaram, I. Svensson, S. De, A. E. Deneris, Y. Dietz, P. Landry, A. Schwenk, and I. Tews, "Inferring three-nucleon couplings from multi-messenger neutron-star observations", Nature Commun. **16**, 9819 (2025).

[64] J. C. Hardy and I. S. Towner, "Superallowed $0^+ \to 0^+$ nuclear β decays: 2014 critical survey, with precise results for V_{ud} and CKM unitarity", Phys. Rev. C **91**, 025501 (2015).

[65] L. Hayen, "Standard model $\mathcal{O}(\alpha)$ renormalization of g_A and its impact on new physics searches", Phys. Rev. D **103**, 113001 (2021).

[66] M. Gennari, M. Drissi, M. Gorchtein, P. Navratil, and C.-Y. Seng, "Ab Initio Strategy for Taming the Nuclear-Structure Dependence of V_{ud} Extractions: The ^{10}C$\to^{10}$B Superallowed Transition", Phys. Rev. Lett. **134**, 012501 (2025).

[67] V. Cirigliano, W. Dekens, J. De Vries, M. L. Graesser, E. Mereghetti, S. Pastore, and U. Van Kolck, "New Leading Contribution to Neutrinoless Double-β Decay", Phys. Rev. Lett. **120**, 202001 (2018).

[68] V. Cirigliano et al., "Neutrinoless Double-Beta Decay: A Roadmap for Matching Theory to Experiment", (2022), arXiv:2203.12169 [hep-ph].

[69] D. B. Kaplan, M. J. Savage, and M. B. Wise, "Nucleon - nucleon scattering from effective field theory", Nucl. Phys. B **478**, 629–659 (1996).

[70] A. Nogga, R. G. E. Timmermans, and U. van Kolck, "Renormalization of one-pion exchange and power counting", Phys. Rev. C **72**, 054006 (2005).

[71] M. Pavon Valderrama and E. Ruiz Arriola, "Renormalization of NN interaction with chiral two pion exchange potential: Non-central phases", Phys. Rev. C **74**, [Erratum: Phys.Rev.C 75, 059905 (2007)], 064004 (2006).

[72] U. van Kolck, "The Problem of Renormalization of Chiral Nuclear Forces", Front. Phys. **8**, 79 (2020).

[73] P. F. Bedaque and U. van Kolck, "Nucleon deuteron scattering from an effective field theory", Phys. Lett. B **428**, 221–226 (1998).

[74] U. van Kolck, "Effective field theory of short range forces", Nucl. Phys. A **645**, 273–302 (1999).

[75] D. B. Kaplan, M. J. Savage, and M. B. Wise, "A New expansion for nucleon-nucleon interactions", Phys. Lett. B **424**, 390–396 (1998).

[76] D. B. Kaplan, M. J. Savage, and M. B. Wise, "Two nucleon systems from effective field theory", Nucl. Phys. B **534**, 329–355 (1998).

[77] S. Fleming, T. Mehen, and I. W. Stewart, "NNLO corrections to nucleon-nucleon scattering and perturbative pions", Nucl. Phys. A **677**, 313–366 (2000).

[78] T. D. Cohen and J. M. Hansen, "Low-energy theorems for nucleon-nucleon scattering", Phys. Rev. C **59**, 13–20 (1999).

[79] T. D. Cohen and J. M. Hansen, "Testing low-energy theorems in nucleon-nucleon scattering", Phys. Rev. C **59**, 3047–3051 (1999).

[80] W. Frank, D. J. Land, and R. M. Spector, "Singular potentials", Rev. Mod. Phys. **43**, 36–98 (1971).

[81] S. R. Beane, P. F. Bedaque, L. Childress, A. Kryjevski, J. McGuire, and U. van Kolck, "Singular potentials and limit cycles", Phys. Rev. A **64**, 042103 (2001).

[82] S. Wu and B. Long, "Perturbative NN scattering in chiral effective field theory", Phys. Rev. C **99**, 024003 (2019).

[83] M. C. Birse, "Power counting with one-pion exchange", Phys. Rev. C **74**, 014003 (2006).

[84] B. Long and U. van Kolck, "Renormalization of Singular Potentials and Power Counting", Ann. Phys. **323**, 1304–1323 (2008).

[85] M. Pavon Valderrama and E. Ruiz Arriola, "Renormalization of the deuteron with one pion exchange", Phys. Rev. C **72**, 054002 (2005).

[86] M. Pavon Valderrama, "Perturbative Renormalizability of Chiral Two Pion Exchange in Nucleon-Nucleon Scattering: P- and D-waves", Phys. Rev. C **84**, 064002 (2011).

[87] C. J. Yang, "Do we know how to count powers in pionless and pionful effective field theory?", Eur. Phys. J. A **56**, 96 (2020).

[88] M. Pavón Valderrama, M. Sánchez Sánchez, C. J. Yang, B. Long, J. Carbonell, and U. van Kolck, "Power Counting in Peripheral Partial Waves: The Singlet Channels", Phys. Rev. C **95**, 054001 (2017).

[89] M. P. Valderrama, "Perturbative renormalizability of chiral two pion exchange in nucleon-nucleon scattering", Phys. Rev. C **83**, 024003 (2011).

[90] B. Long and C. J. Yang, "Renormalizing chiral nuclear forces: a case study of 3P0", Phys. Rev. C **84**, 057001 (2011).

[91] B. Long and C. J. Yang, "Short-range nuclear forces in singlet channels", Phys. Rev. C **86**, 024001 (2012).

[92] B. Long and C. J. Yang, "Renormalizing chiral nuclear forces: triplet channels", Phys. Rev. C **85**, 034002 (2012).

[93] C. J. Yang, "Chiral potential renormalized in harmonic-oscillator space", Phys. Rev. C **94**, 064004 (2016).

[94] H. W. Griesshammer, "A Consistency Test of EFT Power Countings from Residual Cutoff Dependence", Eur. Phys. J. A **56**, 118 (2020).

[95] E. Epelbaum, A. M. Gasparyan, J. Gegelia, and U.-G. Meißner, "How (not) to renormalize integral equations with singular potentials in effective field theory", Eur. Phys. J. A **54**, 186 (2018).

[96] A. M. Gasparyan and E. Epelbaum, ""Renormalization-group-invariant effective field theory" for few-nucleon systems is cutoff dependent", Phys. Rev. C **107**, 034001 (2023).

[97] E. Epelbaum and U.-G. Meissner, "On the Renormalization of the One-Pion Exchange Potential and the Consistency of Weinberg's Power Counting", Few Body Syst. **54**, 2175–2190 (2013).

[98] M. Pavon Valderrama, "Comment on "How (not) to renormalize integral equations with singular potentials in effective field theory" by E. Epelbaum et al.", Eur. Phys. J. A **55**, 55 (2019).

[99] E. Epelbaum, A. M. Gasparyan, J. Gegelia, and U.-G. Meißner, "Reply to "Comment on "How (not) to renormalize integral equations with singular potentials in effective field theory"", Eur. Phys. J. A **55**, 56 (2019).

[100] G. P. Lepage, "How to renormalize the Schrodinger equation", in 8th Jorge Andre Swieca Summer School on Nuclear Physics (1997), pp. 135–180.

[101] A. M. Gasparyan and E. Epelbaum, "Nucleon-nucleon interaction in chiral effective field theory with a finite cutoff: Explicit perturbative renormalization at next-to-leading order", Phys. Rev. C **105**, 024001 (2022).

[102] E. Epelbaum and J. Gegelia, "Regularization, renormalization and 'peratization' in effective field theory for two nucleons", Eur. Phys. J. A **41**, 341–354 (2009).

[103] V. G. J. Stoks, R. A. M. Klomp, M. C. M. Rentmeester, and J. J. de Swart, "Partial wave analaysis of all nucleon-nucleon scattering data below 350-MeV", Phys. Rev. C **48**, 792–815 (1993).

[104] R. Peng, S. Lyu, and B. Long, "Perturbative chiral nucleon–nucleon potential for the $^3P_0$ partial wave", Commun. Theor. Phys. **72**, 095301 (2020).

[105] Y.-H. Song, R. Lazauskas, and U. van Kolck, "Triton binding energy and neutron-deuteron scattering up to next-to-leading order in chiral effective field theory", Phys. Rev. C **96**, [Erratum: Phys.Rev.C 100, 019901 (2019)], 024002 (2017).

[106] C. J. Yang, A. Ekström, C. Forssén, and G. Hagen, "Power counting in chiral effective field theory and nuclear binding", Phys. Rev. C **103**, 054304 (2021).

[107] C. J. Yang, A. Ekström, C. Forssén, G. Hagen, G. Rupak, and U. van Kolck, "The importance of few-nucleon forces in chiral effective field theory", Eur. Phys. J. A **59**, 233 (2023).

[108] K. G. Wilson, "The Renormalization Group and Strong Interactions", Phys. Rev. D **3**, 1818 (1971).

[109] G. P. Lepage, "What is Renormalization?", in Theoretical Advanced Study Institute in Elementary Particle Physics (1989).

[110] R. Workman et al. (Particle Data Group), *Review of particle physics*, to be published (2022).

[111] D. P. Aguillard et al. (Muon g-2), "Measurement of the Positive Muon Anomalous Magnetic Moment to 127 ppb", Phys. Rev. Lett. **135**, 101802 (2025).

[112] J. R. Ellis, "Beyond the standard model with the LHC", Nature **448**, 297–301 (2007).

[113] J. Ellis, "Outstanding questions: Physics beyond the Standard Model", Phil. Trans. Roy. Soc. Lond. A **370**, 818–830 (2012).

[114] L. Allwicher, L. Di Luzio, M. Fedele, F. Mescia, and M. Nardecchia, "What is the scale of new physics behind the muon g-2?", Phys. Rev. D **104**, 055035 (2021).

[115] S. Weinberg, *The Quantum theory of fields. Vol. 1: Foundations* (Cambridge University Press, 2005).

[116] E. Fermi, "Tentativo di una teoria dell'emissione dei raggi beta", Ric. Sci. **4**, 491–495 (1933).

[117] A. Glick-Magid and D. Gazit, "A formalism to assess the accuracy of nuclear-structure weak interaction effects in precision β-decay studies", J. Phys. G **49**, 105105 (2022).

[118] R. Gupta, "Introduction to lattice QCD: Course", in Les Houches Summer School in Theoretical Physics, Session 68: Probing the Standard Model of Particle Interactions (1997), pp. 83–219.

[119] C. C. Chang et al., "A per-cent-level determination of the nucleon axial coupling from quantum chromodynamics", Nature **558**, 91–94 (2018).

[120] S. Aoki and T. Doi, "Lattice QCD and baryon-baryon interactions: HAL QCD method", Front. in Phys. **8**, 307 (2020).

[121] S. Durr et al. (BMW), "Ab-Initio Determination of Light Hadron Masses", Science **322**, 1224–1227 (2008).

[122] M. E. Peskin and D. V. Schroeder, *An Introduction to quantum field theory* (Addison-Wesley, Reading, USA, 1995).

[123] R. Machleidt and D. R. Entem, "Chiral effective field theory and nuclear forces", Phys. Rep. **503**, 1–75 (2011).

[124] U.-G. Meißner and A. Rusetsky, *Effective Field Theories* (Cambridge University Press, 2022).

[125] S. L. Adler, "Axial vector vertex in spinor electrodynamics", Phys. Rev. **177**, 2426–2438 (1969).

[126] E. Noether, "Invariante variationsprobleme", Nachrichten von der Gesellschaft der Wissenschaften zu Göttingen, Mathematisch-Physikalische Klasse, 235–257 (1918).

[127] E. Noether, "Invariant Variation Problems", Gott. Nachr. **1918**, 235–257 (1918).

[128] S. Weinberg, *The quantum theory of fields. Vol. 2: Modern applications* (Cambridge University Press, 2013).

[129] J. Goldstone, A. Salam, and S. Weinberg, "Broken Symmetries", Phys. Rev. **127**, 965–970 (1962).

[130] M. Gell-Mann, R. J. Oakes, and B. Renner, "Behavior of current divergences under SU(3) x SU(3)", Phys. Rev. **175**, 2195–2199 (1968).

[131] S. R. Coleman, J. Wess, and B. Zumino, "Structure of phenomenological Lagrangians. 1.", Phys. Rev. **177**, 2239–2247 (1969).

[132] C. G. Callan Jr., S. R. Coleman, J. Wess, and B. Zumino, "Structure of phenomenological Lagrangians. 2.", Phys. Rev. **177**, 2247–2250 (1969).

[133] H. Georgi, "An Effective Field Theory for Heavy Quarks at Low-energies", Phys. Lett. B **240**, 447–450 (1990).

[134] E. E. Jenkins and A. V. Manohar, "Baryon chiral perturbation theory using a heavy fermion Lagrangian", Phys. Lett. B **255**, 558–562 (1991).

[135] T. Mannel, W. Roberts, and Z. Ryzak, "A derivation of the heavy quark effective lagrangian from qcd", Nuclear Physics B **368**, 204–217 (1992).

[136] L. L. Foldy and S. A. Wouthuysen, "On the Dirac theory of spin 1/2 particle and its nonrelativistic limit", Phys. Rev. **78**, 29–36 (1950).

[137] M. E. Luke and A. V. Manohar, "Reparametrization invariance constraints on heavy particle effective field theories", Phys. Lett. B **286**, 348–354 (1992).

[138] R. Machleidt, "The meson theory of nuclear forces and nuclear structure", in *Advances in nuclear physics*, edited by J. W. Negele and E. Vogt (Springer US, Boston, MA, 1989), pp. 189–376.

[139] J. R. Taylor, *Scattering Theory: The quantum Theory on Nonrelativistic Collisions* (Wiley, New York, 1972).

[140] W. Glöckle, *The Quantum Mechanical Few-body Problem* (Springer-Verlag, Berlin Heidelberg, 1983).

[141] A. Ekström, D. R. Phillips, L. Platter, and M. R. Schindler, "Inferring the breakdown scales of the chiral expansions for gA and mN", Phys. Lett. B **875**, 140352 (2026).

[142] N. Kaiser, R. Brockmann, and W. Weise, "Peripheral nucleon-nucleon phase shifts and chiral symmetry", Nucl. Phys. A **625**, 758–788 (1997).

[143] M. Piarulli, L. Girlanda, R. Schiavilla, R. Navarro Pérez, J. E. Amaro, and E. Ruiz Arriola, "Minimally nonlocal nucleon-nucleon potentials with chiral two-pion exchange including Δ resonances", Phys. Rev. C **91**, 024003 (2015).

[144] A. Dyhdalo, R. J. Furnstahl, K. Hebeler, and I. Tews, "Regulator Artifacts in Uniform Matter for Chiral Interactions", Phys. Rev. C **94**, 034001 (2016).

[145] H. Krebs and E. Epelbaum, "Toward consistent nuclear interactions from chiral Lagrangians. I. The path-integral approach", Phys. Rev. C **110**, 044003 (2024).

[146] H. Krebs and E. Epelbaum, "Toward consistent nuclear interactions from chiral Lagrangians. II. Symmetry preserving regularization", Phys. Rev. C **110**, 044004 (2024).

[147] O. Thim, *nn-mwpc: an open-source research code for perturbatively computing nucleon-nucleon scattering observables*, `https://github.com/othim/nn_mwpc`, (2026).

[148] K. M. Case, "Singular potentials", Phys. Rev. **80**, 797–806 (1950).

[149] A. Bastai, L. Bertocchi, S. Fubini, G. Furlan, and M. Tonin, "On the treatment of singular bethe-salpeter equations", en, Nuovo Cim **30**, 1512–1531 (1963).

[150] H. Behncke, "Some remarks on singular attractive potentials", Il Nuovo Cimento A (1965-1970) **55**, 780–785 (1968).

[151] H.-W. Hammer and B. G. Swingle, "On the limit cycle for the $1/r^2$ potential in momentum space", Ann. Phys. **321**, 306–317 (2006).

[152] M. Pavon Valderrama and E. Ruiz Arriola, "Renormalization group analysis of boundary conditions in potential scattering", Annals Phys. **323**, 1037–1086 (2008).

[153] R. G. Newton, *Scattering theory of waves and particles* (Springer-Verlag New York, Inc., 175 Fifth Avenue New York, New York, 10010 U.S.A., 1982).

[154] M. Pavon Valderrama, "Scattering amplitudes versus potentials in nuclear effective field theory: is there a potential compromise?", (2019), arXiv:`1902.08172 [nucl-th]`.

[155] E. Epelbaum, H.-W. Hammer, and U.-G. Meissner, "Modern Theory of Nuclear Forces", Rev. Mod. Phys. **81**, 1773–1825 (2009).

[156] O. Thim, A. Ekström, and C. Forssén, "Perturbative computations of neutron-proton scattering observables using renormalization-group invariant chiral effective field theory up to N3LO", Phys. Rev. C **109**, 064001 (2024).

[157] J. Bystricky, F. Lehar, and P. Winternitz, "Formalism of Nucleon-Nucleon Elastic Scattering Experiments", J. Phys. (France) **39**, 1 (1978).

[158] H. P. Stapp, T. J. Ypsilantis, and N. Metropolis, "Phase shift analysis of 310-MeV proton proton scattering experiments", Phys. Rev. **105**, 302–310 (1957).

[159] K. Erkelenz, R. Alzetta, and K. Holinde, "Momentum space calculations and helicity formalism in nuclear physics", Nucl. Phys. A **176**, 413–432 (1971).

[160] M. I. Haftel and F. Tabakin, "Nuclear saturation and the smoothness of nucleon-nucleon potentials", Nucl. Phys. A **158**, 1–42 (1970).

[161] R. H. Landau, *Quantum mechanics ii: a second course in quantum theory*, 2nd ed (Wiley, New York, 1996).

[162] M. Cacciari and N. Houdeau, "Meaningful characterisation of perturbative theoretical uncertainties", JHEP **09**, 039 (2011).

[163] O. Thim, E. May, A. Ekström, and C. Forssén, "Bayesian analysis of chiral effective field theory at leading order in a modified Weinberg power counting approach", Phys. Rev. C **108**, 054002 (2023).

[164] U. van Kolck, "Naturalness in nuclear effective field theories", Eur. Phys. J. A **56**, 97 (2020).

[165] I. Svensson, A. Ekström, and C. Forssén, "Inference of the low-energy constants in Δ-full chiral effective field theory including a correlated truncation error", Phys. Rev. C **109**, 064003 (2024).

[166] L. I. G. B. Abrahamsson, O. Thim, A. Ekström, and C. Forssén, "Correlated effective field theory truncation errors: from nucleon-nucleon scattering amplitudes to observables", (*in preparation*).

[167] I. Vernon, M. Goldstein, and R. Bower, "Galaxy formation: a bayesian uncertainty analysis", Bayesian Anal. **5(4)**, 619–669 (2010).

[168] I. Vernon, M. Goldstein, and R. Bower, "Galaxy formation: bayesian history matching for the observable universe", Statist. Sci. **29**, 81–90 (2014).

[169] I. Vernon, J. Liu, M. Goldstein, J. Rowe, J. Topping, and K. Lindsey, "Bayesian uncertainty analysis for complex systems biology models: emulation, global parameter searches and evaluation of gene functions", BMC Syst. Biol. **12**, 1 (2018).

[170] R. Navarro Pérez, J. E. Amaro, and E. Ruiz Arriola, "Partial-wave analysis of nucleon-nucleon scattering below the pion-production threshold", Phys. Rev. C **88**, 024002 (2013).

[171] R. N. Pérez, J. E. Amaro, and E. R. Arriola, "Coarse-grained potential analysis of neutron-proton and proton-proton scattering below the pion production threshold", Phys. Rev. C **88**, 064002 (2013).

[172] R. Navarro Pérez, J. E. Amaro, and E. Ruiz Arriola, "The low-energy structure of the nucleon–nucleon interaction: statistical versus systematic uncertainties", J. Phys. G **43**, 114001 (2016).

[173] S.-I. Ando and C. H. Hyun, "Effective range corrections from effective field theory with di-baryon fields and perturbative pions", Phys. Rev. C **86**, 024002 (2012).

[174] M. Pavon Valderrama and E. Ruiz Arriola, "Renormalization of singlet NN scattering with one pion exchange and boundary conditions", Phys. Lett. B **580**, 149–156 (2004).

[175] V. Baru, E. Epelbaum, A. A. Filin, and J. Gegelia, "Low-energy theorems for nucleon-nucleon scattering at unphysical pion masses", Phys. Rev. C **92**, 014001 (2015).

[176] V. Baru, E. Epelbaum, and A. A. Filin, "Low-energy theorems for nucleon-nucleon scattering at $M_\pi = 450$ MeV", Phys. Rev. C **94**, 014001 (2016).

[177] E. Epelbaum, W. Gloeckle, and U.-G. Meissner, "Improving the convergence of the chiral expansion for nuclear forces. 2. Low phases and the deuteron", Eur. Phys. J. A **19**, 401–412 (2004).

[178] O. Thim, "Low-Energy Theorems for Neutron–Proton Scattering in χEFT Using a Perturbative Power Counting", Few Body Syst. **65**, 69 (2024).

[179] E. Epelbaum, "Chiral Symmetry and Nuclear Interactions", Few Body Syst. **65**, 39 (2024).

[180] E. Wigner, "On the Consequences of the Symmetry of the Nuclear Hamiltonian on the Spectroscopy of Nuclei", Phys. Rev. **51**, 106–119 (1937).

[181] F. Hund, "Symmetrieeigenschaften der Kräfte in Atomkernen und Folgen fur deren Zustände, insbesondere der Kerne bis zu sechzehn Teilchen", Z. Phys. **105**, 202 (1937).

[182] J. C. Parikh, *Group Symmetries in Nuclear Structure* (Plenum Press, 1978), pp. 143–194.

[183] D. Lee et al., "Hidden Spin-Isospin Exchange Symmetry", Phys. Rev. Lett. **127**, 062501 (2021).

[184] X. Lin, H. Singh, R. P. Springer, and J. Vanasse, "Cold neutron-deuteron capture and Wigner-SU(4) symmetry", Phys. Rev. C **108**, 044001 (2023).

[185] S. Shen, T. A. Lähde, D. Lee, and U.-G. Meißner, "Wigner SU(4) symmetry, clustering, and the spectrum of ^{12}C", Eur. Phys. J. A **57**, 276 (2021).

[186] E. P. Wigner, "On Coupling Conditions in Light Nuclei and the Lifetimes of beta-Radioactivities", Phys. Rev. **56**, 519–527 (1939).

[187] S. S. Li Muli, T. R. Djärv, C. Forssén, and D. R. Phillips, "The role of spin-isospin symmetries in nuclear β-decays", (2025), arXiv:2503.16372 [nucl-th].

[188] T. Mehen, I. W. Stewart, and M. B. Wise, "Wigner symmetry in the limit of large scattering lengths", Phys. Rev. Lett. **83**, 931–934 (1999).

[189] A. Ekström and L. Platter, "Breakdown scale of pionless effective field theory in the three-nucleon sector", Phys. Rev. C **112**, L031002 (2025).

[190] S. König, H. W. Grießhammer, H. W. Hammer, and U. van Kolck, "Nuclear Physics Around the Unitarity Limit", Phys. Rev. Lett. **118**, 202501 (2017).

[191] S. König, "Energies and radii of light nuclei around unitarity", Eur. Phys. J. A **56**, 113 (2020).

[192] J. Vanasse and D. R. Phillips, "Three-nucleon bound states and the Wigner-SU(4) limit", Few Body Syst. **58**, 26 (2017).

[193] B.-N. Lu, N. Li, S. Elhatisari, Y.-Z. Ma, D. Lee, and U.-G. Meißner, "Perturbative Quantum Monte Carlo Method for Nuclear Physics", Phys. Rev. Lett. **128**, 242501 (2022).

[194] D. B. Kaplan and A. V. Manohar, "The Nucleon-nucleon potential in the $1/N_c$ expansion", Phys. Rev. C **56**, 76–83 (1997).

[195] S. R. Beane, D. B. Kaplan, N. Klco, and M. J. Savage, "Entanglement Suppression and Emergent Symmetries of Strong Interactions", Phys. Rev. Lett. **122**, 102001 (2019).

[196] I. Low and T. Mehen, "Symmetry from entanglement suppression", Phys. Rev. D **104**, 074014 (2021).

[197] Q. Liu, I. Low, and T. Mehen, "Minimal entanglement and emergent symmetries in low-energy QCD", Phys. Rev. C **107**, 025204 (2023).

[198] T.-R. Hu, K. Sone, F.-K. Guo, T. Hyodo, and I. Low, "Entanglement suppression, quantum statistics, and symmetries in spin-3/2 baryon scatterings", Phys. Rev. Res. **7**, 043306 (2025).

[199] Y. P. Teng and H. W. Griesshammer, "On two nucleons near unitarity with perturbative pions", Eur. Phys. J. A **61**, 211 (2025).

[200] Q. Liu, I. Low, and Z. Yin, "A Quantum Computational Determination of the Weak Mixing Angle in the Standard Model", (2025), arXiv:2509.18251 [hep-ph].

[201] D. Bai and Z. Ren, "Entanglement generation in few-nucleon scattering", Phys. Rev. C **106**, 064005 (2022).

[202] E. F. Zagirdinova and K. A. Kouzakov, "The Effects of Quantum Entanglement in Low-Energy Proton–Proton Scattering", Moscow Univ. Phys. Bull. **77**, 490–497 (2022).

[203] T. Kirchner, W. Elkamhawy, and H.-W. Hammer, "Entanglement in Few-Nucleon Scattering Events", Few Body Syst. **65**, 29 (2024).

[204] D. Bai, "Spin entanglement in neutron-proton scattering", Phys. Lett. B **845**, 138162 (2023).

[205] D. Bai, "Toward experimental determination of spin entanglement of nucleon pairs", Phys. Rev. C **109**, 034001 (2024).

[206] D. Bai, "Quantum information in nucleon-nucleon scattering", Phys. Rev. C **107**, 044005 (2023).

[207] Q. Liu and I. Low, "Hints of entanglement suppression in hyperon-nucleon scattering", Phys. Lett. B **856**, 138899 (2024).

[208] C. E. P. Robin and M. J. Savage, "Quantum complexity fluctuations from nuclear and hypernuclear forces", Phys. Rev. C **112**, 044004 (2025).

[209] T.-R. Hu, S. Chen, K. Sone, F.-K. Guo, T. Hyodo, and I. Low, "Entanglement suppression and emergent symmetries in hadron scatterings", PoS **HADRON2025**, 104 (2026).

[210] H. Witala, "Investigation of entanglement in pure final polarization states from neutron–deuteron elastic scattering and exclusive deuteron breakup", Eur. Phys. J. A **62**, 24 (2026).

[211] H. Witala, J. Golak, and R. Skibiński, "Searching for entanglement in final polarization states of neutron-proton scattering", Phys. Rev. C **112**, 044002 (2025).

[212] A. Cavallin, *Entanglement and accidental symmetries in nuclear effective field theory*, Master's Thesis, Göteborg, Sweden, 2025.

[213] L. Abrahamsson, A. Cavallin, L. Hanebring, H. Hansen, E. Karlsson Öhman, and L. Westin, *Kvantmekanisk sammanflätning i nukleon-nukleonspridning*, Kandidatarbete inom fysik, Göteborg, Sweden, 2023.

[214] P. Zanardi, "Entanglement of quantum evolutions", Phys. Rev. A **63**, 040304 (2001).

[215] W. M. De Muynck, "Distinguishable- and indistinguishable-particle descriptions of systems of identical particles", Int. J. Theor. Phys. **14**, 327–346 (1975).

[216] F. Herbut and M. Vujicic, "Irrelevance of the pauli principle in distant correlations between identical fermions", J. Phys. A **20**, 5555 (1987).

[217] F. Herbut, *How to Distinguish Identical Particles. The General Case*, 2006, arXiv:quant-ph/0611049 [quant-ph].

[218] M. Tichy, F. de Melo, M. Kuś, F. Mintert, and A. Buchleitner, "Entanglement of identical particles and the detection process", Fortschr. Phys. **61**, 225–237 (2012).

[219] F. D. Cunden, S. Di Martino, P. Facchi, and G. Florio, "Spatial separation and entanglement of identical particles", Int. J. Quantum Inf. **12**, 1461001 (2014).

[220] F. Benatti, R. Floreanini, F. Franchini, and U. Marzolino, "Entanglement in indistinguishable particle systems", Phys. Rep. **878**, 1–27 (2020).

[221] A. L. Cavallin, O. Thim, and C. Forssén, "Entanglement and accidental symmetries in the nucleon-nucleon system", Phys. Rev. C **113**, 014005 (2026).

[222] L. Lamata and J. Leon, "Generation of bipartite spin entanglement via spin-independent scattering", Phys. Rev. A **73**, 052322 (2006).

[223] Z. X. Shen, H. Y. Shang, Y. G. Ma, D. Bai, S. M. Wang, Z. C. Xu, Y. Ayyad, and C. Filgueira, "Emergent Bell-Triplet State in Proton-Proton Scattering", (2025), arXiv:2510.24325 [nucl-th].

[224] J. S. Bell, "On the Einstein-Podolsky-Rosen paradox", Physics Physique Fizika **1**, 195–200 (1964).

[225] M. Lamehi-Rachti and W. Mittig, "Quantum Mechanics and Hidden Variables: A Test of Bell's Inequality by the Measurement of the Spin Correlation in Low-Energy Proton Proton Scattering", Phys. Rev. D **14**, 2543–2555 (1976).

[226] C. Robin, M. J. Savage, and N. Pillet, "Entanglement Rearrangement in Self-Consistent Nuclear Structure Calculations", Phys. Rev. C **103**, 034325 (2021).

[227] A. T. Kruppa, J. Kovács, P. Salamon, Ö. Legeza, and G. Zaránd, "Entanglement and seniority", Phys. Rev. C **106**, 024303 (2022).

[228] A. Tichai, S. Knecht, A. T. Kruppa, Ö. Legeza, C. P. Moca, A. Schwenk, M. A. Werner, and G. Zarand, "Combining the in-medium similarity renormalization group with the density matrix renormalization group: Shell structure and information entropy", Phys. Lett. B **845**, 138139 (2023).

[229] C. W. Johnson and O. C. Gorton, "Proton-neutron entanglement in the nuclear shell model", J. Phys. G **50**, 045110 (2023).

[230] A. Pérez-Obiol, S. Masot-Llima, A. M. Romero, J. Menéndez, A. Rios, A. García-Sáez, and B. Juliá-Díaz, "Quantum entanglement patterns in the structure of atomic nuclei within the nuclear shell model", Eur. Phys. J. A **59**, 240 (2023).

[231] O. C. Gorton and C. W. Johnson, "Weak entanglement approximation for nuclear structure", Phys. Rev. C **110**, 034305 (2024).

[232] P. Navratil, G. P. Kamuntavicius, and B. R. Barrett, "Few nucleon systems in translationally invariant harmonic oscillator basis", Phys. Rev. C **61**, 044001 (2000).

[233] P. Navratil, J. P. Vary, and B. R. Barrett, "Large basis ab initio no-core shell model and its application to C-12", Phys. Rev. C **62**, 054311 (2000).

[234] R. Machleidt, "What is ab initio?", Few Body Syst. **64**, 77 (2023).

[235] C. Lanczos, "An iteration method for the solution of the eigenvalue problem of linear differential and integral operators", J. Res. Natl. Bur. Stand. B **45**, 255–282 (1950).

[236] G. Hagen, T. Papenbrock, and D. J. Dean, "Solution of the center-of-mass problem in nuclear structure calculations", Phys. Rev. Lett. **103**, 062503 (2009).

[237] D. H. Gloeckner and R. D. Lawson, "Spurious center-of-mass motion", Phys. Lett. B **53**, 313–318 (1974).

[238] K. A. Wendt, C. Forssén, T. Papenbrock, and D. Sääf, "Infrared length scale and extrapolations for the no-core shell model", Phys. Rev. C **91**, 061301 (2015).

[239] O. Thim, *py-ncsm: an open-source research code for perturbatively computing three-nucleon ground-state energies in the jacobi no-core shell model.* `https://github.com/othim/py-ncsm`, (2025).

[240] L. D. Faddeev, "Scattering Theory for a Three-Particle System", Sov. Phys. JETP **12**, 1014–1019 (1961).

[241] S. König, "Second-order perturbation theory for ^{3}He and pd scattering in pionless EFT", J. Phys. G **44**, 064007 (2017).

[242] V. I. Kukulin and V. N. Pomerantsev, "The Orthogonal Projection Method in Scattering Theory", Annals Phys. **111**, 330–363 (1978).

[243] W. J. Huang, M. Wang, F. G. Kondev, G. Audi, and S. Naimi, "The AME 2020 atomic mass evaluation (I). Evaluation of input data, and adjustment procedures", Chin. Phys. C **45**, 030002 (2021).

[244] O. Thim, A. Ekström, and C. Forssén, "Perturbative χEFT calculations of the deuteron and triton up to N2LO", Phys. Rev. C **112**, 064008 (2025).

[245] R. Peng, B. Long, and F.-R. Xu, "Contact operators in renormalization of attractive singular potentials", Phys. Rev. C **110**, 054001 (2024).

[246] C. J. Yang, "Further theoretical study on the renormalization group aspect of perturbative corrections", Phys. Rev. C **112**, 014004 (2025).

[247] M. Pavon Valderrama, "Regulator constraints for the perturbative renormalizability of attractive triplets", Phys. Rev. C **112**, 064009 (2025).

[248] C. Forssén, B. D. Carlsson, H. T. Johansson, D. Sääf, A. Bansal, G. Hagen, and T. Papenbrock, "Large-scale exact diagonalizations reveal low-momentum scales of nuclei", Phys. Rev. C **97**, 034328 (2018).

[249] E. Caurier and F. Nowacki, "Present Status of Shell Model Techniques", Acta Physica Polonica B **30**, 705 (1999).

[250] E. Caurier, G. Martinez-Pinedo, F. Nowacki, A. Poves, J. Retamosa, and A. P. Zuker, "Full $0\hbar\omega$ shell model calculation of the binding energies of the 1f(7/2) nuclei", Phys. Rev. C **59**, 2033–2039 (1999).

[251] P. Navrtil and E. Caurier, "Nuclear structure with accurate chiral perturbation theory nucleon nucleon potential: Application to ^{6}Li and ^{10}B", Phys. Rev. C **69**, 014311 (2004).

[252] S. Mondal, M. Schäfer, M. Bagnarol, N. Barnea, U. Raha, and J. Kirscher, "A practical approach to perturbative corrections to few-body observables", (2025), arXiv:`2509.17366 [nucl-th]`.

[253] B. Fornberg, "Generation of finite difference formulas on arbitrarily spaced grids", Mathematics of Computation **51**, 699–706 (1988).

[254] S. Binder et al. (LENPIC), "Few-nucleon and many-nucleon systems with semilocal coordinate-space regularized chiral nucleon-nucleon forces", Phys. Rev. C **98**, 014002 (2018).

[255] K. Heyde, *The nuclear shell model* (Springer-Verlag, 1994).

[256] M. Moshinsky, "Transformation brackets for harmonic oscillator functions", Nucl. Phys. **13**, 104–116 (1959).

[257] S. Binder, A. Ekström, G. Hagen, T. Papenbrock, and K. A. Wendt, "Effective field theory in the harmonic oscillator basis", Phys. Rev. C **93**, 044332 (2016).

[258] G. P. Kamuntavicius, P. Navratil, B. R. Barrett, G. Sapragonaite, and R. K. Kalinauskas, "Isoscalar Hamiltonians for light atomic nuclei", Phys. Rev. C **60**, 044304 (1999).

[259] H. T. Johansson and C. Forssén, "Fast and Accurate Evaluation of Wigner $3j$, $6j$, and $9j$ Symbols Using Prime Factorization and Multiword Integer Arithmetic", SIAM J. Sci. Comput. **38**, A376–A384 (2016).

[260] A. Ekström, *Private communication*, 2024.

[261] D. A. Varshalovich, A. N. Moskalev, and V. K. Khersonskii, *Quantum theory of angular momentum* (World Scientific, Singapore, 1988).

[262] G. P. Kamuntavicius, R. K. Kalinauskas, B. R. Barrett, S. Mickevicius, and D. Germanas, "The General harmonic oscillator brackets: Compact expression, symmetries, sums and Fortran code", Nucl. Phys. A **695**, 191–201 (2001).

[263] L. Trlifaj, "Simple Formula for the General Oscillator Brackets", Phys. Rev. C **5**, 1534–1539 (1972).

[264] P. Navratil, J. P. Vary, and B. R. Barrett, "Properties of C-12 in the ab initio nuclear shell model", Phys. Rev. Lett. **84**, 5728–5731 (2000).

[265] M. Sotona and M. Gimitro, "Generalized transformation brackets for the harmonic oscillator functions", Comp. Phys. Comm. **3** (1971).

Appendix A

Perturbative computations in ^{3}H using the no-core shell model

In this appendix, it is explained how to solve the Schrödinger equation for a system of $A = 3$ interacting nucleons using the NCSM formulated in relative coordinates. The specific system considered is ^{3}H ($J^\Pi = \frac{1}{2}^+$, $T = \frac{1}{2}$). It is explained in detail how to construct an antisymmetric basis of harmonic-oscillator states, how to obtain potential matrix elements in this basis, and how to solve the Schrödinger equation exactly or perturbatively. All computations are implemented in an open-source `python` program (`py-ncsm`) that is available for download [239]. A brief description of `py-ncsm` and examples of how to use it are also provided.

A.1 Theoretical formalism

This section describes the formalism required to implement the NCSM for three nucleons in relative coordinates.

The three-nucleon Hamiltonian

The starting point for describing the A-nucleon system is the A-nucleon Hamiltonian

$$H = \sum_{i=1}^{A} \frac{\boldsymbol{P}_i^2}{2m_N} + \sum_{i<j=1}^{A} V_{ij}, \tag{A.1}$$

where only two-nucleon forces are considered in this case. Here, m_N denotes the nucleon mass, $\boldsymbol{P}_i$ the nucleon momentum in the laboratory frame, and V_{ij} the two-nucleon potential between nucleons i and j.

We will only consider the case $A = 3$, for which relative (Jacobi) coordinates can be introduced to describe the positions of the three particles

$$\boldsymbol{\xi}_0 = \sqrt{\frac{1}{3}} \left[\boldsymbol{r}_1 + \boldsymbol{r}_2 + \boldsymbol{r}_3 \right], \tag{A.2}$$

$$\boldsymbol{\xi}_1 = \sqrt{\frac{1}{2}} \left[\boldsymbol{r}_1 - \boldsymbol{r}_2 \right], \tag{A.3}$$

$$\boldsymbol{\xi}_2 = \sqrt{\frac{2}{3}} \left[\frac{1}{2} \left(\boldsymbol{r}_1 + \boldsymbol{r}_2 \right) - \boldsymbol{r}_3 \right], \tag{A.4}$$

where $\{\boldsymbol{r}_i\}_{i=1}^3$ are the laboratory coordinates for the three nucleons. In general, the coordinate $\boldsymbol{\xi}_i$ is proportional to the relative position between the i+1 nucleon and the c.m. of the i first nucleons. The c.m. motion can now be eliminated by expressing the Hamiltonian in the c.m. frame ($\sum_i \boldsymbol{P}_i = 0$), where we denote the particle momenta as $\boldsymbol{p}_i$. This leaves the Hamiltonian for the intrinsic motion

$$H_{\text{int}} = \frac{1}{3} \sum_{i<j=1}^{3} \frac{(\boldsymbol{p}_i - \boldsymbol{p}_j)^2}{2m_N} + \sum_{i<j=1}^{3} V_{ij}. \tag{A.5}$$

The kinetic energy only depends on the relative momenta, which can be written in terms of the Jacobi momenta corresponding to $\boldsymbol{\xi}_1$ and $\boldsymbol{\xi}_2$

$$\boldsymbol{\eta}_1 = \sqrt{\frac{1}{2}} (\boldsymbol{p}_1 - \boldsymbol{p}_2), \tag{A.6}$$

$$\boldsymbol{\eta}_2 = \sqrt{\frac{1}{6}} (\boldsymbol{p}_1 + \boldsymbol{p}_2) - \sqrt{\frac{2}{3}} \boldsymbol{p}_3. \tag{A.7}$$

One advantage of using the Jacobi basis is that the c.m. motion can be eliminated entirely.

The next step is to construct a three-nucleon basis in which the Hamiltonian in Eq. (A.5) can be expressed and diagonalized. This is the subject of the coming sections.

Constructing a fully antisymmetric three-nucleon basis

A basis for the three-nucleon system in the c.m. frame can be chosen as

$$|\boldsymbol{\xi}_1\rangle \otimes |\boldsymbol{\xi}_2\rangle \otimes |(s\frac{1}{2})Sm_S\rangle \otimes |(t\frac{1}{2})Tm_T\rangle \,. \tag{A.8}$$

Here, s and t denote the spin and isospin of the subsystem consisting of nucleons one and two, while S and T, with associated projections m_S and m_T, denote the total spin and isospin for the three-nucleon system. In the NCSM approach,

the spatial part of the wave functions is expanded in terms of eigenfunctions of the spherical HO

$$|\boldsymbol{\xi}_1\rangle = \sum_{n\ell m_\ell} \langle n\ell m_\ell|\boldsymbol{\xi}_1\rangle\, |n\ell m_\ell\rangle\,. \tag{A.9}$$

The overlap $\langle\boldsymbol{\xi}_1|n\ell m_\ell\rangle = R_{n\ell}(|\boldsymbol{\xi}_1|;b)\times Y^\ell_{m_\ell}(\hat{\boldsymbol{\xi}}_1)$ can be expressed in terms of the radial wave function

$$R_{n\ell}(r;b) = \sqrt{\frac{2(n!)}{\Gamma(n+l+\frac{3}{2})b^3}}\left(\frac{r}{b}\right)^\ell e^{-\frac{1}{2}\left(\frac{r}{b}\right)^2} L_n^{\ell+1/2}\left(\frac{r^2}{b^2}\right) \tag{A.10}$$

and spherical harmonics Y^ℓ_m, where $L^\alpha_n(x)$ denotes the generalized Laguerre polynomials. The expansion of $\boldsymbol{\xi}_2$ is analogous in terms of the HO states labeled $|\mathcal{N}\mathcal{L}m_\mathcal{L}\rangle$. Furthermore, $b=(m_N\omega)^{-1/2}$ is the HO length parameter defined in terms of the nucleon mass and the HO frequency ω.

A set of basis functions, equivalent to those in Eq. (A.8), can thus be constructed as

$$|n\ell m_\ell\rangle\otimes|\mathcal{N}\mathcal{L}m_\mathcal{L}\rangle\otimes|(s\tfrac{1}{2})Sm_S\rangle\otimes|(t\tfrac{1}{2})Tm_T\rangle\,. \tag{A.11}$$

By coupling the quantum numbers $(\ell,\mathcal{L})$ to a total L and further coupling (L,S) to J we obtain the basis states

$$\begin{aligned}|n\mathcal{N}(\ell\mathcal{L})L(s\tfrac{1}{2})S;(LS)Jm_J\rangle\otimes|(t\tfrac{1}{2})Tm_T\rangle&\\ = \sum_{m_L,m_S} C^{Jm_J}_{Lm_L,Sm_S}\,|n\mathcal{N}(\ell\mathcal{L})Lm_L\rangle\otimes|(s\tfrac{1}{2})Sm_S\rangle\otimes|(t\tfrac{1}{2})Tm_T\rangle\,.&\end{aligned} \tag{A.12}$$

These states are referred to as using LS-coupling since the angular momentum and spin for each coordinate are coupled first, and then coupled to the total J. For our purposes, it is convenient to also express these states in the so-called JJ-coupling scheme, where the spin and orbital angular momentum for each coordinate are coupled first. This recouping can be compactly written using a Wigner $9j$ - symbol as [140, 255]

$$\begin{aligned}|n\mathcal{N}(\ell s)j(\mathcal{L}\tfrac{1}{2})\mathcal{J};(j\mathcal{J})Jm_J\rangle\otimes|(t\tfrac{1}{2})Tm_T\rangle = \sum_{L,S}\,\hat{j}\hat{\mathcal{J}}\hat{L}\hat{S}\begin{Bmatrix}\ell & s & j\\ \mathcal{L} & \frac{1}{2} & \mathcal{J}\\ L & S & J\end{Bmatrix}&\\ \times|n\mathcal{N}\ (\ell\mathcal{L})L(s\tfrac{1}{2})S;(LS)Jm_J\rangle\otimes|(t\tfrac{1}{2})Tm_T\rangle\,,&\end{aligned} \tag{A.13}$$

where the notation $\hat{j}\equiv\sqrt{2j+1}$ is used for all quantum numbers.

It is straightforward to enforce antisymmetry in the states in Eq. (A.13) for the $(1,2)$ subsystem by enforcing the condition $(-1)^{\ell+s+t}=-1$. This

condition guarantees that the basis states are antisymmetric under the exchange of particles ($1 \leftrightarrow 2$), but not under any of the exchanges ($1 \leftrightarrow 3$) or ($2 \leftrightarrow 3$). These states are thus referred to as partially antisymmetric, for which we introduce the notation

$$|n\mathcal{N}\alpha\rangle_{12} \equiv |n\ell sjt, \mathcal{N}\mathcal{L}\mathcal{J}; JT\rangle \equiv |n\mathcal{N}(\ell s)j(\mathcal{L}\frac{1}{2})\mathcal{J}; (j\mathcal{J})Jm_J\rangle \otimes |(t\frac{1}{2})Tm_T\rangle\,, \tag{A.14}$$

where m_J and m_T are dropped by rotational symmetry and assumed isospin symmetry, $\alpha \equiv (\ell sjt\mathcal{L}\mathcal{J}JT)$, and the index (12) denotes that the state is antisymmetric under the exchange ($1 \leftrightarrow 2$).

Fully antisymmetric states are constructed as eigenvectors of the three-nucleon antisymmetrizer

$$\hat{\mathcal{A}} = \frac{1}{3!}(1 - P_{12} - P_{23} - P_{13} + P_{12}P_{23} + P_{13}P_{23}), \tag{A.15}$$

where P_{ij} is the permutation operator for particles i and j. It is shown in detail in Appendix A.4 that the matrix elements of the antisymmetrizer can be expressed as [232]

$$_{12}\langle n\mathcal{N}\alpha|\hat{\mathcal{A}}|n'\mathcal{N}'\alpha'\rangle_{12} = \frac{1}{3} \times {}_{12}\langle n\mathcal{N}\alpha|n'\mathcal{N}'\alpha'\rangle_{12} \tag{A.16}$$

$$- \frac{2}{3}\delta_{NN'} \sum_{L,S} \hat{s}\hat{s}'\hat{t}\hat{t}'\hat{j}\hat{\mathcal{J}}\hat{j}'\hat{\mathcal{J}}'\hat{L}^2\hat{S}^2(-1)^L \begin{Bmatrix} \ell & s & j \\ \mathcal{L} & \frac{1}{2} & \mathcal{J} \\ L & S & J \end{Bmatrix} \begin{Bmatrix} \ell' & s' & j' \\ \mathcal{L}' & \frac{1}{2} & \mathcal{J}' \\ L & S & J \end{Bmatrix}$$

$$\times \begin{Bmatrix} \frac{1}{2} & \frac{1}{2} & s \\ \frac{1}{2} & S & s' \end{Bmatrix} \begin{Bmatrix} \frac{1}{2} & \frac{1}{2} & t \\ \frac{1}{2} & T & t' \end{Bmatrix} \times \langle n\mathcal{N}(\ell\mathcal{L}) : L|\mathcal{N}'n'(\mathcal{L}'\ell') : L\rangle^T_{1/d}\,. \tag{A.17}$$

We use the notation $N \equiv 2n + \ell + 2\mathcal{N} + \mathcal{L}$ for both the primed and unprimed quantum numbers, and assume $J = J'$ and $T = T'$. The last bracket is called a Moshinsky bracket [256], and the relation between different conventions is derived in Appendix A.4.

The antisymmetrization can be done separately for sets of constant (N, J, T), since the antisymmetrization operator is diagonal in these quantum numbers. Fully antisymmetric states are the eigenstates with eigenvalue one and are labeled as

$$|NJT, \gamma\rangle = \sum_{n,\mathcal{N},\alpha \,:\, \substack{2n+\ell+ \\ 2\mathcal{N}+\mathcal{L}=N}} {}_{12}\langle n\mathcal{N}\alpha|NJT, \gamma\rangle\, |n\mathcal{N}\alpha\rangle_{12}\,, \tag{A.18}$$

where $\gamma = 0, 1, 2, ...$ enumerates states which share quantum numbers (N, J, T). The complete set of fully antisymmetric basis states for a specific spin, parity, and isospin (J^Π, T) up to the basis truncation $N_{\max}$ is obtained as

$$\{\,|\Gamma\rangle\,\} \equiv \bigcup_{N \le N_{\max}} \{\,|NJT, \gamma\rangle\,\}. \tag{A.19}$$

Expressing the Hamiltonian in the fully antisymmetric basis

We will now express the intrinsic Hamiltonian in Eq. (A.5) in the fully antisymmetric basis Eq. (A.19), i.e.,

$$\langle\Gamma|H_{\rm int}|\Gamma'\rangle\,. \tag{A.20}$$

Let us start with the kinetic energy. Using properties of the permutation operators together with the antisymmetry of the states $|\Gamma\rangle$, the kinetic energy can be expressed as

$$\begin{aligned}\langle\Gamma|T_{\rm int}|\Gamma'\rangle &= \langle\Gamma|\frac{1}{3}\frac{1}{2m_N}(\boldsymbol{p}_{12}^2+\boldsymbol{p}_{13}^2+\boldsymbol{p}_{23}^2)|\Gamma'\rangle \\ &= \frac{1}{3}\frac{1}{2m_N}\langle\Gamma|(\boldsymbol{p}_{12}^2+P_{23}\boldsymbol{p}_{12}^2P_{23}+P_{12}P_{13}\boldsymbol{p}_{12}^2P_{13}P_{12})|\Gamma'\rangle \\ &= \frac{1}{2m_N}\langle\Gamma|\boldsymbol{p}_{12}^2|\Gamma'\rangle = \frac{1}{m_N}\langle\Gamma|\boldsymbol{\eta}_1^2|\Gamma'\rangle\,. \end{aligned}\tag{A.21}$$

The notation $\boldsymbol{p}_{ij}\equiv\boldsymbol{p}_i-\boldsymbol{p}_j$ is used to simplify expressions. The final matrix element can be evaluated by inserting a complete set of $\{|n\mathcal{N}\alpha\rangle_{12}\}$ states and using the relation [257]

$$\begin{aligned}&{}_{12}\langle n\mathcal{N}\alpha|\boldsymbol{\eta}_1^2|n'\mathcal{N}'\alpha'\rangle_{12} \\ &= \delta_{\mathcal{N}\mathcal{N}'}\delta_{\mathcal{L}\mathcal{L}'}\delta_{\mathcal{J}\mathcal{J}'}\delta_{ss'}\delta_{jj'}\delta_{tt'}\int_0^\infty d\eta_1\ \eta_1^2\ \tilde{R}_{n\ell}(\eta_1;b)\eta_1^2\tilde{R}_{n'\ell'}(\eta_1;b) \\ &= \delta_{\mathcal{N}\mathcal{N}'}\delta_{\mathcal{L}\mathcal{L}'}\delta_{\mathcal{J}\mathcal{J}'}\delta_{ss'}\delta_{jj'}\delta_{tt'}\frac{1}{b^2}\delta_{\ell\ell'}\Big(\delta_{n(n'+1)}\sqrt{(n'+1)(n'+\ell'+\frac{3}{2})} \\ &+ \delta_{nn'}(2n'+\ell'+\frac{3}{2})+\delta_{n(n'-1)}\sqrt{n'(n'+\ell'+\frac{1}{2})}\Big).\end{aligned}\tag{A.22}$$

We define

$$\tilde{R}_{n\ell}(p;b) = \sqrt{\frac{2}{\pi}}\int_0^\infty dr\ r^2R_{n\ell}(r;b)j_\ell(pr) \tag{A.23}$$

$$= (-1)^n\sqrt{\frac{2(n!)b^3}{\Gamma(n+l+\frac{3}{2})}}(pb)^\ell e^{-\frac{1}{2}(pb)^2}L_n^{\ell+1/2}((pb)^2), \tag{A.24}$$

where $L_n^\alpha(x)$ denotes the generalized Laguerre polynomials.

We move on to evaluate the two-nucleon potential in the fully antisymmetric basis. Analogously to Eq. (A.21), we exploit the complete antisymmetry of the basis states to write

$$\langle\Gamma|\sum_{i<j=1}^{3}V_{ij}|\Gamma'\rangle = 3\,\langle\Gamma|V_{12}|\Gamma'\rangle\,, \tag{A.25}$$

and it thus suffices to evaluate $\langle\Gamma|V_{12}|\Gamma'\rangle$. This is again done by inserting a complete set of $\{|n\mathcal{N}\alpha\rangle_{12}\}$ states which reduces the computation to evaluating

$$ {}_{12}\langle n\mathcal{N}\alpha|V_{12}|n'\mathcal{N}'\alpha'\rangle_{12} = \delta_{\mathcal{N}\mathcal{N}'}\delta_{\mathcal{L}\mathcal{L}'}\delta_{\mathcal{J}\mathcal{J}'}\delta_{jj'}\delta_{ss'}\delta_{tt'}\,\langle n\ell sjt|\,V_{12}\,|n'\ell' sjt\rangle\,. \tag{A.26}$$

The computation of the matrix elements $\langle n\ell sjt|\,V_{12}\,|n'\ell' sjt\rangle$, using the isospin formalism in Ref. [258], is explained in detail in Appendix A.5.

A.2 Numerical implementation

This section describes the main parts of the `py-ncsm` code, in which the NCSM for ^{3}H is implemented in `python`. The code has two key dependencies:

- `wigxjpf` — Open-source code for computing Clebsch-Gordan coefficients as well as Wigner 6j and 9j symbols [259].
- `gmosh` — Routine that computes Moshinsky brackets [260] (included in `py-ncsm`).

Constructing the fully antisymmetric basis

The first step in an NCSM computation is to generate a set of basis states. We introduce a shorthand notation for the set of partially antisymmetric states $\{|n\mathcal{N}\alpha\rangle_{12}\} \equiv \{|\alpha\rangle\}_{\alpha=1}^{N_\alpha}$, where the index α now simply enumerates the states for a given $N_{\max}$. The fully antisymmetric states up to a given $N_{\max}$ is similarly denoted $\{|\Gamma\rangle\}_{\Gamma=1}^{N_\Gamma}$, see Eq. (A.19). The states $\{|\alpha\rangle\}_{\alpha=1}^{N_\alpha}$ are straightforward to construct by simply iterating over the allowed set of quantum numbers $(nlsjt\mathcal{N}\mathcal{L}\mathcal{J}JT)$, considering the various spin couplings. The basis dimensions N_α and N_Γ for triton at various $N_{\max}$ are presented in Table A.1. It can be observed that the basis dimensions grow rapidly, which is the main hurdle for going to large values of $N_{\max}$.

Table A.1: Basis dimensions for the partially antisymmetric (N_α) and the fully antisymmetric (N_Γ) states for different $N_{\max}$ for $\left(J^\Pi = \frac{1}{2}^+,\, T = \frac{1}{2}\right)$.

$N_{\max}$	N_α	N_Γ
0	2	1
10	322	108
20	1892	632
30	5712	1906
40	12782	4263

The fully antisymmetric states are constructed by computing eigenvectors of $\hat{\mathcal{A}}$ expressed in the partially antisymmetric basis as

$$\sum_{\alpha'} \langle \alpha | \hat{\mathcal{A}} | \alpha' \rangle \langle \alpha' | s \rangle = \lambda \langle \alpha | s \rangle . \tag{A.27}$$

All eigenvectors $|s\rangle$ with $\lambda = 1$ are collected as columns in an $N_\alpha \times N_\Gamma$ matrix $\boldsymbol{S}$, form which the set of fully antisymmetric states $\{|\Gamma\rangle\}_{\Gamma=1}^{N_\Gamma}$ are obtained through

$$|\Gamma\rangle = \sum_\alpha \langle \alpha | \Gamma \rangle |\alpha\rangle = \sum_\alpha \boldsymbol{S}_{\alpha\Gamma} |\alpha\rangle . \tag{A.28}$$

When the size of the matrices grows, the problem of finding eigenvalues and eigenvectors becomes increasingly numerically challenging. In practice, one must define a tolerance for how close an eigenvalue must be to unity to be classified as such. An absolute tolerance of 10^{-5} is found to be big enough up to $N_{\max} = 40$.

The basis information is contained in $\{|\alpha\rangle\}_{\alpha=1}^{N_\alpha}$, $\{|\Gamma\rangle\}_{\Gamma=1}^{N_\Gamma}$, and $\boldsymbol{S}$, which can be computed once for a given $N_{\max}$ and stored to disk. Having the simple basis relation in Eq. (A.28) now makes it easy to use the partially antisymmetric basis to make computations, and subsequently transform to the fully antisymmetric basis. For the Hamiltonian, this is simply done as

$$\begin{aligned} \boldsymbol{H}_{\Gamma\Gamma'} &\equiv \langle \Gamma | H_{\text{int}} | \Gamma' \rangle = \sum_{\alpha,\alpha'} \langle \Gamma | \alpha \rangle \langle \alpha | H_{\text{int}} | \alpha' \rangle \langle \alpha' | \Gamma' \rangle \\ &= \sum_{\alpha,\alpha'} (\boldsymbol{S}^\dagger)_{\Gamma\alpha} \boldsymbol{H}_{\alpha\alpha'} \boldsymbol{S}_{\alpha'\Gamma'} . \end{aligned} \tag{A.29}$$

Since $N_\Gamma < N_\alpha$, $\boldsymbol{S}$ describes a change of basis that is only invertible on the subspace spanned by the completely antisymmetric states, i.e., $\boldsymbol{S}$ describes both a change of basis and a projection operation.

Computing the Hamiltonian matrix

The Hamiltonian is computed in the partially antisymmetric basis $\{|n\mathcal{N}\alpha\rangle_{12}\}$ using Eqs. (A.22) and (A.26). The input that is needed for the computation is the potential matrix elements

$$\begin{aligned} &\langle n\ell sjtm_t | V_{12} | n'\ell' sjtm_t \rangle \\ &= \int_0^\infty dp' p'^2 \int_0^\infty dp p^2 \tilde{R}_{n\ell}(p; \sqrt{2}b) \tilde{R}_{n'\ell'}(p'; \sqrt{2}b) \langle p\ell sjtm_t | V_{12} | p'\ell' sjtm_t \rangle , \end{aligned} \tag{A.30}$$

where $p = \frac{1}{2}|\boldsymbol{p}_1 - \boldsymbol{p}_2|$. See Appendix A.5 for additional details. These integrals are computed numerically using Gauss-Legendre quadrature by introducing a

momentum grid with corresponding weights $\{(p^{(i)}, w^{(i)})\}_{i=1}^{N_p}$. Two types of grids are considered, one on the interval $[0, 2500]$ MeV and one on a numerically infinite interval, $[0, \infty)$, where the latter is constructed by transforming the finite grid by a change of variable [161]. The finite interval works even though the integration domain is infinite, since the regulated potential vanishes for large momenta. These two grids will henceforth be referred to as the *finite* and *infinite*, respectively. The discretized integral reads

$$\begin{aligned}
&\int_0^\infty dp' p'^2 \int_0^\infty dp p^2 \tilde{R}_{n\ell}(p; \sqrt{2}b) \tilde{R}_{n'\ell'}(p'; \sqrt{2}b) \langle p\ell s j t m_t | V_{12} | p'\ell' s j t m_t \rangle \\
&= \sum_{i,j=1}^{N_p} w^{(i)} w^{(j)} (p^{(i)})^2 (p^{(j)})^2 \tilde{R}_{n\ell}(p^{(j)}; \sqrt{2}b) \tilde{R}_{n'\ell'}(p^{(i)}; \sqrt{2}b) \\
&\times \langle p^{(j)} \ell s j t m_t | V_{12} | p^{(i)} \ell' s j t m_t \rangle \,. \qquad \text{(A.31)}
\end{aligned}$$

The code reads the matrix elements in Eq. (A.30) from a provided text file of the form:

```
<possible meta data>
DATA:
n   l   np  lp  s   j   mt  ME
0   0   0   0   0   0   -1  -7.966724483064686
0   0   1   0   0   0   -1  -2.652044568838252
0   0   2   0   0   0   -1  2.89434840507413
0   0   3   0   0   0   -1  7.911560485250315
...
```

where the matrix element (ME) is given in MeV. Note that $m_t = -1$ is used for pp states. The generation of interaction files is implemented in `nn-mwpc`. Finally, the kinetic energy is added and the basis transformation in Eq. (A.29) is applied to get the matrix elements in the fully antisymmetric basis

$$\boldsymbol{H}_{\Gamma\Gamma'} = \langle \Gamma | H_{\text{int}} | \Gamma' \rangle \,. \qquad \text{(A.32)}$$

Diagonalizing the Hamiltonian for ^{3}H — a minimal working example

This section will briefly describe how the code `py-ncsm` is used to perform a full diagonalization of the ^{3}H Hamiltonian. The first step is to compute the set of basis states for a given $N_{\max}$. This is done by running

```
py-ncsm/src/states $ python compute_save_basis.py --NMAX=0,2,4
```

which will generate files containing the bases and the transformation matrix. The triton channel $\left(J^\Pi = \frac{1}{2}^+, T = \frac{1}{2}\right)$ is pre-selected in the

`compute_save_basis.py` file but can be changed to any channel. When the basis states are generated, one has to construct an input file. Several example input files are provided, e.g.,
`py-ncsm/example_inout_files/in_small.txt`:

```
[settings]
nmax_arr         = [0,2,4,10,20]
hbar_omega       = 24    # hbar_omega in MeV.
isospin_sym      = False
fast_comp        = False # Not implemented
dim_lanczos      = 2000
interaction_file = interactions/
idaho_n3lo_nmax_40_hw_24_Np_80_finite.txt
output_file      = example-inout-files/out_small.txt
```

The code that computes and diagonalizes the ^{3}H Hamiltonian is executed by running

```
py-ncsm $ python run-py-ncsm.py example-inout-files/in_small.txt
```

A more complete user guide is provided in the `README` file in the code repository.

Perturbative ground-state energy computations

Perturbative ground-state energy computations with the Rayleigh-Schrödinger (Eqs. (5.8) to (5.10)), and FD (Eq. (5.18)) approaches are implemented in `py-ncsm/pert-calc/`. With the machinery to compute matrix elements in the fully antisymmetric basis (see Eq. (A.29)), it is straightforward to implement the matrix operations needed for the perturbative computations. Examples and more information are provided in the `README` files in the code repository.

A.3 Benchmark computations

The implementation in `py-ncsm` is validated by performing computations with the Idaho-N3LO potential from Ref. [27]. Table A.2 shows computed ground-state energies for different $N_{\max}$ compared to a similar code used as a reference [260]. An agreement to at least 4 significant digits (which is the precision provided by the other code) is observed for $N_{\max} \leq 40$. The good agreement with the reference code strongly indicates that the implementation of `py-ncsm` gives correct results. However, to assess the numerical stability, it is appropriate to do several convergence studies concerning the parameters that control the approximations that are introduced in the computations. The convergence of the ground-state energy as a function of $N_{\max}$, ω, and N_p will now be investigated.

Table A.2: Ground-state energies for ^{3}H for different $N_{\max}$ using the Idaho-N3LO interaction [27] and the isospin formalism in Ref. [258]. HO frequency $\omega = 24$ MeV and an infinite grid with $N_p = 110$ were used. The computations are compared to a similar code [260]. The last column shows the dimension of the Hamiltonian (N_Γ).

$N_{\max}$	E_g (MeV) [260]	E_g (MeV) (`py-ncsm`)	N_Γ
0	12.165	12.165	1
10	−5.053	−5.053	108
20	−7.773	−7.773	632
30	−7.849	−7.849	1906
32	−7.850	−7.850	2280
34	−7.851	−7.851	2700
36	−7.852	−7.852	3169
38	−7.852	−7.852	3689
40	−7.852	−7.852	4263

The parameters $N_{\max}$ and ω control the HO basis, whereas N_p controls the accuracy to which the potential matrix elements are computed in Eq. (A.31). Figure A.1 shows the ^{3}H ground-state energy as a function of N_p employing both a finite and infinite Gauss-Legendre grid. It is observed that a higher number of discretization points is needed for converging computations for larger values of $N_{\max}$. This is not surprising, since basis functions with higher n and ℓ exhibit an increasing oscillatory behavior. It can also be observed that the finite grid is more efficient, requiring fewer discretization points to achieve the same accuracy. Regardless of the grid we employ, N_p needs to be chosen sufficiently high such that the ground-state energy is converged for all values of $N_{\max}$ that are considered. It is observed that the ground-state energy is lower for computations that are not converged in N_p.

We move on to study how the ground-state energy depends on the basis parameters $N_{\max}$ and ω, which control the size and shape of the basis, respectively. From here on, we will use an infinite grid with $N_p = 100$ to compute potential matrix elements if nothing else is stated. This is sufficient for $N_{\max} \leq 30$. In the left panel of Fig. A.2, the ground-state energy of ^{3}H is shown as a function of $N_{\max}$ for different values of ω. It is observed that the ground-state energy converges for increasing $N_{\max}$, and that the converged result still has an underbinding of approximately 0.5 MeV compared to the experimental value. A trend of less ω dependence as $N_{\max}$ increases can be observed. This is further illustrated in the right panel of Fig. A.2, where the ground-state energy is shown as a function of ω. The ground-state energy for a given $N_{\max}$ shows a parabolic behavior, where the dependence on ω decreases when $N_{\max}$ increases. This is reasonable since the result should be less sensitive to the value of ω (which only controls the shape of the basis functions) when the size of the basis is increased,

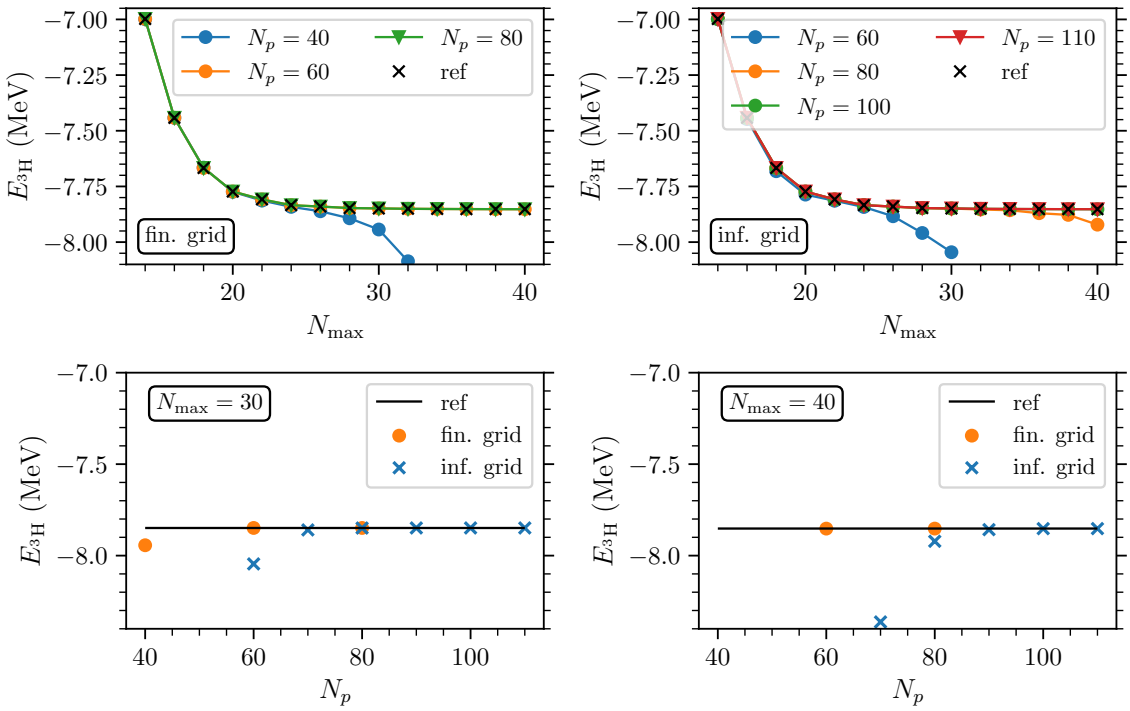

Figure A.1: The two top panels show the convergence of the ^{3}H ground-state energy as a function of $N_{\max}$ for different N_p with a finite (infinite) Gauss-Legendre grid in the left (right) panel. HO frequency $\omega = 24$ MeV is employed in all computations. The two lower panels show the ground-state energy as a function of N_p for both the finite and infinite grid, for $N_{\max} = 30$ ($N_{\max} = 40$) in the left (right) panel, respectively. The reference computations [260] are shown in black, see Table A.2.

and the dependence should vanish in the limit when $N_{\max} \to \infty$. Since the problem is variational, the best approximation to the ground-state energy for a given $N_{\max}$ is when taking the value of ω that minimizes the ground-state energy. This is the reason why $\omega = 24$ MeV has been chosen for many of the computations.

A.4 Constructing the fully antisymmetric basis

Computing matrix elements of the antisymmetrizer

Fully antisymmetric states can be constructed from the partially antisymmetric states in Eq. (A.14) by computing eigenvectors of the three-particle antisymmetrizer

$$\hat{\mathcal{A}} = \frac{1}{3!}(1 - P_{12} - P_{23} - P_{13} + P_{12}P_{23} + P_{13}P_{23}), \tag{A.33}$$

where P_{ij} is the permutation operator for particles i and j. Antisymmetric states are the eigenstates of $\hat{\mathcal{A}}$ with eigenvalue one. Acting with permutation

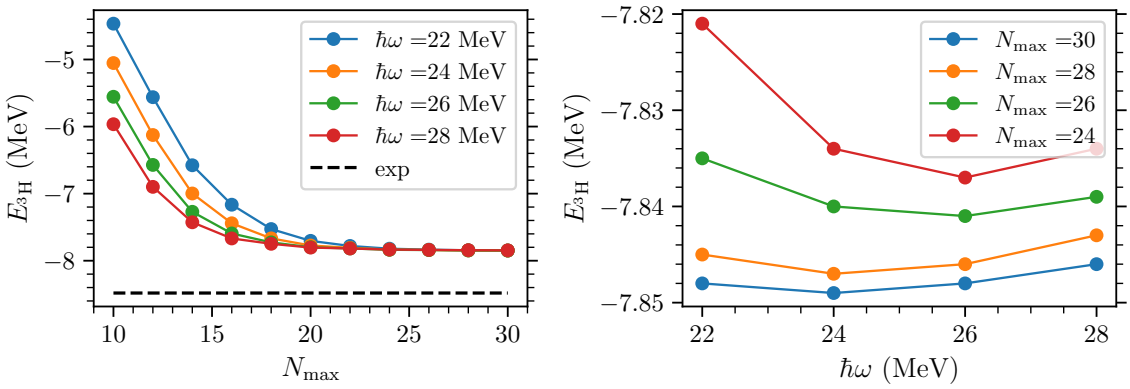

Figure A.2: ^{3}H ground-state energies computed using different $N_{\max}$ and ω. The left panel shows the ground-state energy as a function of $N_{\max}$ for $\omega = 22, \ldots, 28$ MeV together with the experimental ground-state energy. In the right panel, the ground-state energy as a function of ω is shown for different $N_{\max}$.

operators on the partially antisymmetric basis states gives

$$P_{13}\,|n\mathcal{N}\alpha\rangle_{12} = |n\mathcal{N}\alpha\rangle_{32}\,, \quad P_{23}\,|n\mathcal{N}\alpha\rangle_{12} = |n\mathcal{N}\alpha\rangle_{13}\,, \quad P_{12}\,|n\mathcal{N}\alpha\rangle_{12} = -\,|n\mathcal{N}\alpha\rangle_{12}\,.$$

By using the properties $P_{ij}^2 = 1$ and $P_{ij}P_{il}P_{ij} = P_{jl}$ we can express matrix elements of $\hat{\mathcal{A}}$ as

$$\begin{aligned}
&{}_{12}\langle n\mathcal{N}\alpha|\hat{\mathcal{A}}|n'\mathcal{N}'\alpha'\rangle_{12} \\
&= \frac{1}{6}\,{}_{12}\langle n\mathcal{N}\alpha|1 - P_{12} - P_{23} - P_{13} + P_{12}P_{23} + P_{13}P_{23}|n'\mathcal{N}'\alpha'\rangle_{12} \\
&= \frac{1}{6}\,{}_{12}\langle n\mathcal{N}\alpha|2 - P_{23} - P_{12}P_{23}P_{12} + P_{12}P_{23} + P_{13}P_{13}P_{21}P_{13}|n'\mathcal{N}'\alpha'\rangle_{12} \\
&= \frac{1}{6}\,{}_{12}\langle n\mathcal{N}\alpha|2 - P_{23} - P_{23} - P_{23} - P_{23}|n'\mathcal{N}'\alpha'\rangle_{12} \\
&= \frac{1}{3}\,{}_{12}\langle n\mathcal{N}\alpha|1 - 2P_{23}|n'\mathcal{N}'\alpha'\rangle_{12} \\
&= \frac{1}{3}\,{}_{12}\langle n\mathcal{N}\alpha|n'\mathcal{N}'\alpha'\rangle_{12} - \frac{2}{3}\,{}_{12}\langle n\mathcal{N}\alpha|n'\mathcal{N}'\alpha'\rangle_{13}\,.
\end{aligned} \tag{A.34}$$

Thus, the non-trivial matrix element we need to evaluate is ${}_{12}\langle n\mathcal{N}\alpha|n'\mathcal{N}'\alpha'\rangle_{13}$.

Using Eq. (A.13) we recouple spin and orbital angular momentum and get

$$
\begin{aligned}
&{}_{12}\langle n\mathcal{N}\alpha|n'\mathcal{N}'\alpha'\rangle_{13} = {}_{12}\langle n\mathcal{N}(\ell s)j(\mathcal{L}\frac{1}{2})\mathcal{J};(j\mathcal{J})Jm_J| \otimes {}_{12}\langle (t\frac{1}{2})Tm_T| \\
&|n'\mathcal{N}'(\ell's')j'(\mathcal{L}'\frac{1}{2})\mathcal{J}';(j'\mathcal{J}')Jm_J\rangle_{13} \otimes |(t'\frac{1}{2})T'm_{T'}\rangle_{13} \\
&= \sum_{L,S}\sum_{L',S'} \hat{j}\hat{\mathcal{J}}\hat{L}\hat{S} \begin{Bmatrix} \ell & s & j \\ \mathcal{L} & \frac{1}{2} & \mathcal{J} \\ L & S & J \end{Bmatrix} \hat{j}'\hat{\mathcal{J}}'\hat{L}'\hat{S}' \begin{Bmatrix} \ell' & s' & j' \\ \mathcal{L}' & \frac{1}{2} & \mathcal{J}' \\ L' & S' & J \end{Bmatrix} \\
&\times {}_{12}\langle n\mathcal{N}\ (\ell\mathcal{L})L(s\frac{1}{2})S;(LS)Jm_J| \otimes {}_{12}\langle (t\frac{1}{2})Tm_T| \\
&|n'\mathcal{N}'\ (\ell'\mathcal{L}')L'(s'\frac{1}{2})S';(L'S')Jm_J\rangle_{13} \otimes |(t'\frac{1}{2})T'm_{T'}\rangle_{13}\,. \qquad \text{(A.35)}
\end{aligned}
$$

We further uncouple orbital and spin angular momentum using Eq. (A.12) and get

$$
\begin{aligned}
&{}_{12}\langle n\mathcal{N}\ (\ell\mathcal{L})L(s\frac{1}{2})S;(LS)Jm_J| \otimes {}_{12}\langle (t\frac{1}{2})Tm_T| \\
&|n'\mathcal{N}'\ (\ell'\mathcal{L}')L'(s'\frac{1}{2})S';(L'S')Jm_J\rangle_{13} \otimes |(t'\frac{1}{2})T'm_{T'}\rangle_{13} \\
&= \sum_{m_L,m_S}\sum_{m_{L'},m_{S'}} C^{Jm_J}_{Lm_L,Sm_S}C^{Jm_J}_{L'm_{L'},S'm_{S'}} \\
&\times {}_{12}\langle n\mathcal{N}(\ell\mathcal{L})Lm_L| \otimes {}_{12}\langle (s\frac{1}{2})Sm_S| \otimes {}_{12}\langle (t\frac{1}{2})Tm_T| \\
&|n'\mathcal{N}'(\ell'\mathcal{L}')L'm_{L'}\rangle_{13} \otimes |(s'\frac{1}{2})S'm_{S'}\rangle_{13} \otimes |(t'\frac{1}{2})T'm_{T'}\rangle_{13} \\
&= \sum_{m_L,m_S}\sum_{m_{L'},m_{S'}} C^{Jm_J}_{Lm_L,Sm_S}C^{Jm_J}_{L'm_{L'},S'm_{S'}}\,{}_{12}\langle n\mathcal{N}(\ell\mathcal{L})Lm_L|n'\mathcal{N}'(\ell'\mathcal{L}')L'm_{L'}\rangle_{13} \\
&\times {}_{12}\langle (s\frac{1}{2})Sm_S|(s'\frac{1}{2})S'm_{S'}\rangle_{13}\,{}_{12}\langle (t\frac{1}{2})Tm_T|(t'\frac{1}{2})T'm_{T'}\rangle_{13}\,. \qquad \text{(A.36)}
\end{aligned}
$$

The spin and isospin brackets can be expressed using the relation [261]

$$
\begin{aligned}
&\langle[(j_1j_2)j_{12}j_3]jm|[(j_1j_3)j_{13}j_2]j'm'\rangle \\
&= \delta_{jj'}\delta_{mm'}(-1)^{(j_2+j_3+j_{12}+j_{13})}\hat{j}_{12}\hat{j}_{13} \begin{Bmatrix} j_2 & j_1 & j_{12} \\ j_3 & j & j_{13} \end{Bmatrix}. \qquad \text{(A.37)}
\end{aligned}
$$

For the spin we find

$$
{}_{12}\langle (s\frac{1}{2})Sm_S|(s'\frac{1}{2})S'm_S\rangle_{13} = \delta_{SS'}\delta_{m_Sm_{S'}}(-1)^{(1+s+s')}\hat{s}\hat{s}' \begin{Bmatrix} \frac{1}{2} & \frac{1}{2} & s \\ \frac{1}{2} & S & s' \end{Bmatrix}. \qquad \text{(A.38)}
$$

An analogous relation holds for the isospin. We put this into Eq. (A.35) and obtain

$$
\begin{aligned}
{}_{12}\langle n\mathcal{N}\alpha|n'\mathcal{N}'\alpha'\rangle_{13} &= \sum_{L,S} \hat{j}\hat{\mathcal{J}}\hat{L}\hat{S} \begin{Bmatrix} \ell & s & j \\ \mathcal{L} & \frac{1}{2} & \mathcal{J} \\ L & S & J \end{Bmatrix} \hat{j}'\hat{\mathcal{J}}'\hat{L}\hat{S} \begin{Bmatrix} \ell' & s' & j' \\ \mathcal{L}' & \frac{1}{2} & \mathcal{J}' \\ L & S & J \end{Bmatrix} \\
&\times (-1)^{s+s'}\hat{s}\hat{s}' \begin{Bmatrix} \frac{1}{2} & \frac{1}{2} & s \\ \frac{1}{2} & S & s' \end{Bmatrix} \times (-1)^{t+t'}\hat{t}\hat{t}' \begin{Bmatrix} \frac{1}{2} & \frac{1}{2} & t \\ \frac{1}{2} & T & t' \end{Bmatrix} \delta_{TT'}\delta_{m_T m_{T'}} \\
&\times {}_{12}\langle n\mathcal{N}(\ell\mathcal{L})L|n'\mathcal{N}'(\ell'\mathcal{L}')L\rangle_{13} \,. \qquad \text{(A.39)}
\end{aligned}
$$

Using that the last bracket is zero unless $N \equiv 2n + \ell + 2\mathcal{N} + \mathcal{L} = 2n' + \ell' + 2\mathcal{N}' + \mathcal{L}' \equiv N'$, we can finally write the relation as

$$
\begin{aligned}
&{}_{12}\langle n\ell sjt, \mathcal{N}\mathcal{L}\mathcal{J}; JT|n'\ell's'j't', \mathcal{N}'\mathcal{L}'\mathcal{J}'; JT\rangle_{13} \\
&= \delta_{NN'} \sum_{L,S} \hat{s}\hat{s}'\hat{t}\hat{t}'\hat{j}\hat{\mathcal{J}}\hat{j}'\hat{\mathcal{J}}'\hat{L}^2\hat{S}^2(-1)^{(s+s'+t+t')} \begin{Bmatrix} \ell & s & j \\ \mathcal{L} & \frac{1}{2} & \mathcal{J} \\ L & S & J \end{Bmatrix} \begin{Bmatrix} \ell' & s' & j' \\ \mathcal{L}' & \frac{1}{2} & \mathcal{J}' \\ L & S & J \end{Bmatrix} \\
&\times \begin{Bmatrix} \frac{1}{2} & \frac{1}{2} & s \\ \frac{1}{2} & S & s' \end{Bmatrix} \begin{Bmatrix} \frac{1}{2} & \frac{1}{2} & t \\ \frac{1}{2} & T & t' \end{Bmatrix} \times {}_{12}\langle n\mathcal{N}(\ell\mathcal{L})L|n'\mathcal{N}'(\ell'\mathcal{L}')L\rangle_{13} \,. \qquad \text{(A.40)}
\end{aligned}
$$

The sum over L and S is taken with respect to the constraints:

$$
\begin{aligned}
&|\ell - \mathcal{L}| \le L \le |\ell + \mathcal{L}|, \quad |\ell' - \mathcal{L}'| \le L \le |\ell' + \mathcal{L}'|, \\
&|s - \frac{1}{2}| \le S \le |s + \frac{1}{2}|, \quad |s' - \frac{1}{2}| \le S \le |s' + \frac{1}{2}|, \\
&|J - S| \le L \le |J + S|. \qquad \text{(A.41)}
\end{aligned}
$$

The antisymmetrization can be done separately for blocks (N, J, T), since the antisymmetrization operator conserves these quantum numbers. Diagonalizing each block separately is less numerically costly.

Transformation to Kamuntavičius HO bracket

The final step is to express the HO bracket in Eq. (A.40),

$$
{}_{12}\langle n\mathcal{N}(\ell\mathcal{L})L|n'\mathcal{N}'(\ell'\mathcal{L}')L\rangle_{13} \,, \qquad \text{(A.42)}
$$

in terms of the HO bracket

$$
\langle n\mathcal{N}(\ell\mathcal{L}) : L|n'\mathcal{N}'(\ell'\mathcal{L}') : L\rangle_d \,, \qquad \text{(A.43)}
$$

as defined in [262]. The convention for the HO bracket in Eq. (A.43) will be referred to as the K-bracket. The K-bracket is defined for variables related

with the transformation matrix

$$\begin{pmatrix} \boldsymbol{R} \\ \boldsymbol{r} \end{pmatrix} = \mathcal{T} \begin{pmatrix} \boldsymbol{r}_1 \\ \boldsymbol{r}_2 \end{pmatrix}, \quad \mathcal{T} = \begin{pmatrix} \sqrt{\frac{d}{1+d}} & \sqrt{\frac{1}{1+d}} \\ \sqrt{\frac{1}{1+d}} & -\sqrt{\frac{d}{1+d}}. \end{pmatrix}. \tag{A.44}$$

In our notation, the quantum numbers correspond to the coordinates $\boldsymbol{R}(\ell'), \boldsymbol{r}(\mathcal{L}')$ and $\boldsymbol{r}_1(\ell), \boldsymbol{r}_2(\mathcal{L})$. The coordinate transformation of Jacobi coordinates when exchanging $(2 \leftrightarrow 3)$ can be shown to be

$$\begin{pmatrix} \boldsymbol{\xi}_1' \\ \boldsymbol{\xi}_2' \end{pmatrix} = \mathcal{T}' \begin{pmatrix} \boldsymbol{\xi}_1 \\ \boldsymbol{\xi}_2 \end{pmatrix}, \quad \mathcal{T}' = \begin{pmatrix} \frac{1}{2} & \frac{\sqrt{3}}{2} \\ \frac{\sqrt{3}}{2} & -\frac{1}{2} \end{pmatrix}. \tag{A.45}$$

Since $\mathcal{T}' = \mathcal{T}$ if $d = 1/3$, the sought-after relation reads

$${}_{12}\langle n\mathcal{N}(\ell\mathcal{L})L|n'\mathcal{N}'(\ell'\mathcal{L}')L\rangle_{13} = \langle n\mathcal{N}(\ell\mathcal{L}) : L|n'\mathcal{N}'(\ell'\mathcal{L}') : L\rangle_{1/3}\,. \tag{A.46}$$

Transformation to Trlifaj HO bracket

We can also use the convention in [263] for the HO bracket, which we will indicate by a T superscript. This convention is used in the code implementation and the coordinate transformation reads

$$\begin{pmatrix} \boldsymbol{R} \\ \boldsymbol{r} \end{pmatrix} = \mathcal{T} \begin{pmatrix} \boldsymbol{r}_1 \\ \boldsymbol{r}_2 \end{pmatrix}, \quad \tilde{\mathcal{T}} = \begin{pmatrix} \sqrt{\frac{d}{1+d}} & -\sqrt{\frac{1}{1+d}} \\ \sqrt{\frac{1}{1+d}} & \sqrt{\frac{d}{1+d}} \end{pmatrix}, \quad \tilde{\mathcal{T}}^{-1} = \begin{pmatrix} \sqrt{\frac{d}{1+d}} & \sqrt{\frac{1}{1+d}} \\ -\sqrt{\frac{1}{1+d}} & \sqrt{\frac{d}{1+d}} \end{pmatrix}, \tag{A.47}$$

which defines the corresponding HO bracket as

$$\langle n'\mathcal{N}'(\ell'\mathcal{L}') : L|n\mathcal{N}(\ell\mathcal{L}) : L\rangle_d^T\,. \tag{A.48}$$

The quantum numbers correspond to the coordinates as $\boldsymbol{R}(\ell')$, $\boldsymbol{r}(\mathcal{L}')$, $\boldsymbol{r}_1(\ell)$ and $\boldsymbol{r}_2(\mathcal{L})$. We will refer to this bracket as the T-bracket. We note that $\tilde{\mathcal{T}} \neq \tilde{\mathcal{T}}^{-1}$ which means that the T-bracket is not symmetric in general, i.e.,

$$\langle n'\mathcal{N}'(\ell'\mathcal{L}') : L|n\mathcal{N}(\ell\mathcal{L}) : L\rangle_d^T \neq \langle n\mathcal{N}(\ell\mathcal{L}) : L|n'\mathcal{N}'(\ell'\mathcal{L}') : L\rangle_d^T\,. \tag{A.49}$$

We can relate the T-bracket to the K-bracket by observing that the coordinate transformation $\boldsymbol{r}_2 \to -\boldsymbol{r}_2$ in Eq. (A.47) gives the same transformation matrix as in Eq. (A.44), namely

$$\begin{pmatrix} \boldsymbol{R} \\ \boldsymbol{r} \end{pmatrix} = \begin{pmatrix} \sqrt{\frac{d}{1+d}} & \sqrt{\frac{1}{1+d}} \\ \sqrt{\frac{1}{1+d}} & -\sqrt{\frac{d}{1+d}} \end{pmatrix} \begin{pmatrix} \boldsymbol{r}_1 \\ -\boldsymbol{r}_2 \end{pmatrix}. \tag{A.50}$$

This means that the K-bracket can be written in terms of the T-bracket as

$$\begin{aligned}\langle n\mathcal{N}(\ell L):L|n'\mathcal{N}'(\ell' L'):L\rangle_d &= \langle n'\mathcal{N}'(\ell'\mathcal{L}'):L|n\mathcal{N}(\ell\mathcal{L}):L\rangle_d \\ &= (-1)^{\mathcal{L}}\,\langle n'\mathcal{N}'(\ell'\mathcal{L}'):L|n\mathcal{N}(\ell\mathcal{L}):L\rangle_d^T\,. \end{aligned} \tag{A.51}$$

In the first equality, we use that the linear transformation in Eq. (A.44) is its own inverse, and in the second equality we employ the coordinate transformation on $\boldsymbol{r}_2$. To get the T-bracket in the form of Ref. [264], we want to compute C and d' in the transformation

$$\langle n'\mathcal{N}'(\ell'\mathcal{L}'):L|n\mathcal{N}(\ell\mathcal{L}):L\rangle_d^T = C\,\langle n\mathcal{N}(\ell\mathcal{L}):L|\mathcal{N}'n'(\mathcal{L}'\ell'):L\rangle_{d'}^T\,. \tag{A.52}$$

On the right-hand side, the bracket is inverted, and the oscillators on the primed side are coupled in the reverse order. We start with the T-transformation in Eq. (A.47) and make the following manipulations

$$\begin{aligned}
\begin{pmatrix}\boldsymbol{R}\\ \boldsymbol{r}\end{pmatrix} &= \begin{pmatrix}\sqrt{\frac{d}{1+d}} & -\sqrt{\frac{1}{1+d}}\\ \sqrt{\frac{1}{1+d}} & \sqrt{\frac{d}{1+d}}\end{pmatrix}\begin{pmatrix}\boldsymbol{r}_1\\ \boldsymbol{r}_2\end{pmatrix}\\
\begin{pmatrix}\boldsymbol{r}_1\\ \boldsymbol{r}_2\end{pmatrix} &= \begin{pmatrix}\sqrt{\frac{d}{1+d}} & \sqrt{\frac{1}{1+d}}\\ -\sqrt{\frac{1}{1+d}} & \sqrt{\frac{d}{1+d}}\end{pmatrix}\begin{pmatrix}\boldsymbol{R}\\ \boldsymbol{r}\end{pmatrix}\\
\begin{pmatrix}\boldsymbol{r}_1\\ \boldsymbol{r}_2\end{pmatrix} &= \begin{pmatrix}\sqrt{\frac{1}{1+d}} & \sqrt{\frac{d}{1+d}}\\ \sqrt{\frac{d}{1+d}} & -\sqrt{\frac{1}{1+d}}\end{pmatrix}\begin{pmatrix}\boldsymbol{r}\\ \boldsymbol{R}\end{pmatrix} \quad (\text{take } d\to 1/d)\\
\begin{pmatrix}\boldsymbol{r}_1\\ \boldsymbol{r}_2\end{pmatrix} &= \begin{pmatrix}\sqrt{\frac{d}{1+d}} & \sqrt{\frac{1}{1+d}}\\ \sqrt{\frac{1}{1+d}} & -\sqrt{\frac{d}{1+d}}\end{pmatrix}\begin{pmatrix}\boldsymbol{r}\\ \boldsymbol{R}\end{pmatrix}\\
\begin{pmatrix}\boldsymbol{r}_1\\ \boldsymbol{r}_2\end{pmatrix} &= \begin{pmatrix}\sqrt{\frac{d}{1+d}} & -\sqrt{\frac{1}{1+d}}\\ \sqrt{\frac{1}{1+d}} & \sqrt{\frac{d}{1+d}}\end{pmatrix}\begin{pmatrix}\boldsymbol{r}\\ -\boldsymbol{R}\end{pmatrix}.
\end{aligned} \tag{A.53}$$

This shows that the transformation of $(\boldsymbol{r}_1,\boldsymbol{r}_2)\to(\boldsymbol{R},\boldsymbol{r})$ with (d) have the same bracket as the transformation $(\boldsymbol{r},-\boldsymbol{R})\to(\boldsymbol{r}_1,\boldsymbol{r}_2)$ with $1/d$. Using the well-known properties of harmonic oscillator states:

$$\phi_{n\ell m_\ell}(-\boldsymbol{r}) = (-1)^\ell \phi_{n\ell m_\ell}(\boldsymbol{r}), \tag{A.54}$$

$$|n\ell\mathcal{N}\mathcal{L}:L\rangle = (-1)^{\ell+\mathcal{L}-L}\,|\mathcal{N}\mathcal{L}n\ell:L\rangle\,, \tag{A.55}$$

we obtain

$$\begin{aligned}&\langle n'\mathcal{N}'\Big[\ell'(\boldsymbol{R})\mathcal{L}'(\boldsymbol{r})\Big]:L|n\mathcal{N}\Big[\ell(\boldsymbol{r}_1)\mathcal{L}(\boldsymbol{r}_2)\Big]:L\rangle_d^T\\ &= (-1)^{\ell'+\ell'+\mathcal{L}'-L}\,\langle n\mathcal{N}\Big[\ell(\boldsymbol{r}_1)\mathcal{L}(\boldsymbol{r}_2)\Big]:L|\mathcal{N}'n'\Big[\mathcal{L}'(\boldsymbol{r})\ell'(-\boldsymbol{R})\Big]:L\rangle_{1/d}^T\,.\end{aligned} \tag{A.56}$$

In the last step we use the transformation property that we showed for the corresponding variables $(\boldsymbol{r}, -\boldsymbol{R}) \to (\boldsymbol{r}_1, \boldsymbol{r}_2)$ with $1/d$. The full transformation can finally be written as

$$\begin{aligned}
&\langle n\mathcal{N}(\ell L) : L | n'\mathcal{N}'(\ell' L') : L \rangle_d \\
&= (-1)^{\mathcal{L}'+\mathcal{L}-L} \langle n\mathcal{N}(\ell\mathcal{L}) : L | \mathcal{N}' n'(\mathcal{L}'\ell') : L \rangle^T_{1/d} \\
&= (-1)^{\ell'+\ell-L} \langle n\mathcal{N}(\ell\mathcal{L}) : L | \mathcal{N}' n'(\mathcal{L}'\ell') : L \rangle^T_{1/d} \,. \qquad \text{(A.57)}
\end{aligned}$$

In the last equality, we use that $(-1)^{\ell+\mathcal{L}} = (-1)^{\ell'+\mathcal{L}'}$, which follows from conservation of energy. We can now use this T-bracket in Eq. (A.40) to write

$$\begin{aligned}
&{}_{12}\langle n\ell sjt, \mathcal{N}\mathcal{L}\mathcal{J}; JT | n'\ell' s' j' t', \mathcal{N}'\mathcal{L}'\mathcal{J}'; JT \rangle_{13} \\
&= \delta_{NN'} \sum_{L,S} \hat{s}\hat{s}'\hat{t}\hat{t}'\hat{j}\hat{\mathcal{J}}\hat{j}'\hat{\mathcal{J}}'\hat{L}^2\hat{S}^2 (-1)^L \begin{Bmatrix} \ell & s & j \\ \mathcal{L} & \frac{1}{2} & \mathcal{J} \\ L & S & J \end{Bmatrix} \begin{Bmatrix} \ell' & s' & j' \\ \mathcal{L}' & \frac{1}{2} & \mathcal{J}' \\ L & S & J \end{Bmatrix} \\
&\times \begin{Bmatrix} \frac{1}{2} & \frac{1}{2} & s \\ \frac{1}{2} & S & s' \end{Bmatrix} \begin{Bmatrix} \frac{1}{2} & \frac{1}{2} & t \\ \frac{1}{2} & T & t' \end{Bmatrix} \times \langle n\mathcal{N}(\ell\mathcal{L}) : L | \mathcal{N}' n'(\mathcal{L}'\ell') : L \rangle^T_{1/d} \,. \qquad \text{(A.58)}
\end{aligned}$$

This expression and convention for the HO bracket is the same as in [232]. Note that the function `gmosh` in the code takes $D = 1/d$ as the argument, hence the argument should still be $D = 1/3$ [265].

By repeating an analogous calculation for another change of variables, one can show that the following identity holds for T-brackets

$$\langle \mathcal{N} n(\mathcal{L}\ell) : L | n'\mathcal{N}'(\ell'\mathcal{L}') : L \rangle^T_d = (-1)^{\ell'+\mathcal{L}} \langle n\mathcal{N}(\ell\mathcal{L}) : L | \mathcal{N}' n'(\mathcal{L}'\ell') : L \rangle^T_d \,. \qquad \text{(A.59)}$$

A.5 Expressing the Hamiltonian in the fully antisymmetric basis

In this section, we will look at the computation of the matrix elements in Eq. (A.26) in detail. We want to evaluate the matrix element ($\tau = \tau' = 1/2$)

$$
\begin{aligned}
&{}_{12}\langle n\mathcal{N}\alpha|V_{12}|n'\mathcal{N}'\alpha'\rangle_{12} = {}_{12}\left\langle n\ell sjt, \mathcal{N}\mathcal{L}\mathcal{J}; JT\right| V_{12} \left|n'\ell' s' j' t', \mathcal{N}'\mathcal{L}'\mathcal{J}'; JT\right\rangle_{12} \\
&= \sum_{m_j,m_\mathcal{J},m_{j'},m_{\mathcal{J}'}} \sum_{m_t,m_\tau,m_{t'},m_{\tau'}} C^{Jm_J}_{jm_j,\mathcal{J}m_\mathcal{J}} C^{Jm_J}_{j'm_{j'},\mathcal{J}'m_{\mathcal{J}'}} C^{Tm_T}_{tm_t,\tau m_\tau} C^{Tm_T}_{t'm_{t'},\tau' m_{\tau'}} \\
&\times \langle n\ell sjtm_t| \otimes \langle \mathcal{N}\mathcal{L}\mathcal{J}m_\mathcal{J}\tau m_\tau| V_{12} \left|n'\ell' s' j' t' m_{t'}\right\rangle \otimes \left|\mathcal{N}'\mathcal{L}'\mathcal{J}' m_{\mathcal{J}'}\tau' m_{\tau'}\right\rangle \\
&= \sum_{m_j,m_\mathcal{J},m_{j'},m_{\mathcal{J}'}} \sum_{m_t,m_\tau,m_{t'},m_{\tau'}} C^{Jm_J}_{jm_j,\mathcal{J}m_\mathcal{J}} C^{Jm_J}_{j'm_{j'},\mathcal{J}'m_{\mathcal{J}'}} C^{Tm_T}_{tm_t,\tau m_\tau} C^{Tm_T}_{t'm_{t'},\tau' m_{\tau'}} \\
&\times \langle n\ell sjtm_t| V_{12} \left|n'\ell' s' j' t' m_{t'}\right\rangle \left\langle \mathcal{N}\mathcal{L}\mathcal{J}m_\mathcal{J}\tau m_\tau|\mathcal{N}'\mathcal{L}'\mathcal{J}' m_{\mathcal{J}'}\tau' m_{\tau'}\right\rangle \\
&= \delta_{\mathcal{N}\mathcal{N}'}\delta_{\mathcal{L}\mathcal{L}'}\delta_{\mathcal{J}\mathcal{J}'} \sum_{m_j,m_\mathcal{J},m_{j'}} \sum_{m_t,m_\tau,m_{t'}} C^{Jm_J}_{jm_j,\mathcal{J}m_\mathcal{J}} C^{Jm_J}_{j'm_{j'},\mathcal{J}m_\mathcal{J}} C^{Tm_T}_{tm_t,\tau m_\tau} C^{Tm_T}_{t'm_{t'},\tau m_\tau} \\
&\times \langle n\ell sjtm_t| V_{12} \left|n'\ell' s' j' t' m_{t'}\right\rangle \\
&= \delta_{\mathcal{N}\mathcal{N}'}\delta_{\mathcal{L}\mathcal{L}'}\delta_{\mathcal{J}\mathcal{J}'}\delta_{jj'}\delta_{ss'}\delta_{tt'} \sum_{m_j,m_\mathcal{J},m_t,m_\tau} C^{Jm_J}_{jm_j,\mathcal{J}m_\mathcal{J}} C^{Jm_J}_{jm_j,\mathcal{J}m_\mathcal{J}} C^{Tm_T}_{tm_t,\tau m_\tau} C^{Tm_T}_{tm_t,\tau m_\tau} \\
&\times \langle n\ell sjtm_t| V_{12} \left|n'\ell' sjtm_t\right\rangle = (\square).
\end{aligned}
\tag{A.60}
$$

By using the completeness relations of the Clebsch-Gordan coefficients, and the fact that the potential matrix elements are independent of m_j (not explicitly written out) one obtains

$$
\begin{aligned}
(\square) &= \delta_{\mathcal{N}\mathcal{N}'}\delta_{\mathcal{L}\mathcal{L}'}\delta_{\mathcal{J}\mathcal{J}'}\delta_{jj'}\delta_{ss'}\delta_{tt'} && \text{(A.61)} \\
&\times \sum_{m_t,m_\tau} C^{Tm_T}_{tm_t,\tau m_\tau} C^{Tm_T}_{tm_t,\tau m_\tau} \langle n\ell sjtm_t| V_{12} \left|n'\ell' sjtm_t\right\rangle = (*). && \text{(A.62)}
\end{aligned}
$$

If the interaction also is independent of m_t, one finally arrives at

$$
(*) = \delta_{\mathcal{N}\mathcal{N}'}\delta_{\mathcal{L}\mathcal{L}'}\delta_{\mathcal{J}\mathcal{J}'}\delta_{jj'}\delta_{ss'}\delta_{tt'} \left\langle n\ell sjt\right| V_{12} \left|n'\ell' sjt\right\rangle . \tag{A.63}
$$

By employing the formalism in Ref. [258], we can now construct the effective isospin-symmetric potential $\langle n\ell sjt| V_{12} |n'\ell' sjt\rangle$ for the triton state $(A, T, m_T) = (3, \frac{1}{2}, \frac{1}{2})$ as

$$
\begin{aligned}
&\langle n\ell sjt| V_{12} \left|n'\ell' sjt\right\rangle && \text{(A.64)} \\
&\equiv \begin{cases} \frac{1}{3} \langle n\ell sjtm_t| V_{12} \left|n'\ell' sjtm_t\right\rangle_{t=1,m_t=0} + \frac{2}{3} \langle n\ell sjtm_t| V_{12} \left|n'\ell' sjtm_t\right\rangle_{t=1,m_t=1} \\ \langle n\ell sjtm_t| V_{12} \left|n'\ell' sjtm_t\right\rangle_{t=0,m_t=0} \end{cases} .
\end{aligned}
$$

The next step is to relate $\langle n\ell sjtm_t|\, V_{12}\, |n'\ell' sjtm_t\rangle$ to $\langle p\ell sjtm_t|\, V_{12}\, |p'\ell' sjtm_t\rangle$, which is the conventional way to express potential matrix elements. Here, p denotes the modulus of the two-nucleon relative momentum

$$\boldsymbol{p} = \frac{1}{2}(\boldsymbol{p}_1 - \boldsymbol{p}_2). \tag{A.65}$$

Let

$$\boldsymbol{\eta}_1 = \sqrt{\frac{1}{2}}(\boldsymbol{p}_2 - \boldsymbol{p}_1) \tag{A.66}$$

denote the Jacobi momentum, and $\eta_1 = |\boldsymbol{\eta}_1|$. Note that $\boldsymbol{\eta}_1 = -\sqrt{2}\boldsymbol{p}$. We first compute the overlap

$$\begin{aligned}
&\langle n\ell m_\ell|\eta_1\ell' m_{\ell'}\rangle = \int_0^\infty d\boldsymbol{r}\, \langle n\ell m_\ell|\boldsymbol{r}\rangle\, \langle \boldsymbol{r}|\eta_1\ell' m_{\ell'}\rangle \\
&= \int_0^\infty d\hat{r} \int_0^\infty dr\; r^2 R_{n\ell}(r;b) Y^*_{\ell m_\ell}(\hat{\boldsymbol{r}}) \sqrt{\frac{2}{\pi}} i^{\ell'}\, j_{\ell'}(\eta_1 r) Y_{\ell' m_{\ell'}}(\hat{\boldsymbol{r}}) \qquad \text{(A.67)} \\
&= \int_0^\infty dr\; r^2 R_{n\ell}(r;b) \sqrt{\frac{2}{\pi}} i^{\ell} j_{\ell}(\eta_1 r) = \delta_{\ell\ell'}\delta_{m_\ell m_{\ell'}} \sqrt{\frac{2}{\pi}} i^{\ell} \int_0^\infty dr\; r^2 R_{n\ell}(r;b) j_{\ell}(\eta_1 r).
\end{aligned}$$

Using this result we compute

$$\begin{aligned}
&\langle n\ell sjtm_t|\, V_{12}\, |n'\ell' s' jtm_t\rangle = \sum_{m_\ell m_{\ell'} m_s m_{s'}} C^{jm_j}_{\ell m_\ell, s m_s} C^{jm_j}_{\ell' m_{\ell'}, s' m_{s'}} \\
&\sum_{lml'm'} \int_0^\infty d\eta_1' \eta_1'^2 \int_0^\infty d\eta_1 \eta_1^2 \big[\, \langle n\ell m_\ell|\eta_1 lm\rangle\, \langle \eta_1 lm| \otimes \langle sm_s| \otimes \langle tm_t|\,\big] V_{12} \\
&\big[\, |\eta_1' l'm'\rangle\, \langle \eta_1' l'm'|n'\ell' m_{\ell'}\rangle \otimes |s' m_{s'}\rangle \otimes |tm_t\rangle\,\big] \\
&= \sum_{m_\ell m_{\ell'} m_s m_{s'}} C^{jm_j}_{\ell m_\ell, s m_s} C^{jm_j}_{\ell' m_{\ell'}, s' m_{s'}} \int_0^\infty d\eta_1' \eta_1'^2 \int_0^\infty d\eta_1 \eta_1^2 \\
&\times \Big[\Big\{ \sqrt{\frac{2}{\pi}} i^{\ell} \int_0^\infty dr\; r^2 R_{n\ell}(r;b) j_{\ell}(\eta_1 r) \Big\}\, \langle \eta_1 \ell m_\ell| \otimes \langle sm_s| \otimes \langle tm_t| \,\Big] V_{12} \\
&\Big[\, |\eta_1' \ell' m_{\ell'}\rangle \Big\{ \sqrt{\frac{2}{\pi}} i^{-\ell'} \int_0^\infty dr\; r^2 R_{n\ell'}(r;b) j_{\ell'}(\eta_1' r) \Big\} \otimes |s' m_{s'}\rangle \otimes |tm_t\rangle \,\Big] \\
&= \int_0^\infty d\eta_1' \eta_1'^2 \int_0^\infty d\eta_1 \eta_1^2 \Big\{ \sqrt{\frac{2}{\pi}} i^{\ell} \int_0^\infty dr r^2 R_{n\ell}(r;b) j_{\ell}(\eta_1 r) \Big\} \\
&\times \Big\{ \sqrt{\frac{2}{\pi}} i^{-\ell'} \int_0^\infty dr r^2 R_{n\ell'}(r;b) j_{\ell'}(\eta_1' r) \Big\}\, \langle \eta_1 \ell sjtm_t|V_{12}|\eta_1' \ell' sjtm_t\rangle\, \delta_{ss'}. \qquad \text{(A.68)}
\end{aligned}$$

We have defined

$$\tilde{R}_{n\ell}(\eta_1;b) = \sqrt{\frac{2}{\pi}} \int_0^\infty dr\; r^2 R_{n\ell}(r;b) j_{\ell}(\eta_1 r), \tag{A.69}$$

and thus obtain

$$\begin{aligned}&\langle n\ell sjtm_t|\, V_{12}\, |n'\ell' s' jtm_t\rangle \\ &= i^{\ell-\ell'} \int_0^\infty d\eta_1' \eta_1'^2 \int_0^\infty d\eta_1 \eta_1^2 \tilde{R}_{n\ell}(\eta_1; b) \tilde{R}_{n'\ell'}(\eta_1'; b)\, \langle \eta_1 \ell sjtm_t | V_{12} | \eta_1' \ell' sjtm_t\rangle\,.\end{aligned} \tag{A.70}$$

The last complication to attack is that the Jacobi momentum and two-nucleon relative momentum are not defined in the same way. We change the integration variable in Eq. (A.70) to the relative momentum, whose modulus is related to the Jacobi momentum as $p\sqrt{2} = \eta_1$, to get

$$\begin{aligned}&\int_0^\infty d\eta_1' \eta_1'^2 \int_0^\infty d\eta_1 \eta_1^2 \tilde{R}_{n\ell}(\eta_1; b) \tilde{R}_{n'\ell'}(\eta_1'; b)\, \langle \eta_1 \ell sjtm_t | V_{12} | \eta_1' \ell' sjtm_t\rangle \\ &= \sqrt{2}^6 \int_0^\infty dp' p'^2 \int_0^\infty dp p^2 \tilde{R}_{n\ell}(p\sqrt{2}; b) \tilde{R}_{n'\ell'}(p'\sqrt{2}; b) \frac{\langle p\ell sjtm_t | V_{12} | p'\ell' sjtm_t\rangle}{\sqrt{2}^3} \\ &= \sqrt{2}^6 \int_0^\infty dp' p'^2 \int_0^\infty dp p^2 \tilde{R}_{n\ell}(p\sqrt{2}; b) \tilde{R}_{n'\ell'}(p'\sqrt{2}; b) \frac{\langle p\ell sjtm_t | V_{12} | p'\ell' sjtm_t\rangle}{\sqrt{2}^3} \\ &= \sqrt{2}^6 \int_0^\infty dp' p'^2 \int_0^\infty dp p^2 \frac{1}{\sqrt{2}^3} \tilde{R}_{n\ell}(p; \sqrt{2}b) \tilde{R}_{n'\ell'}(p'; \sqrt{2}b) \frac{\langle p\ell sjtm_t | V_{12} | p'\ell' sjtm_t\rangle}{\sqrt{2}^3} \\ &= \int_0^\infty dp' p'^2 \int_0^\infty dp p^2 \tilde{R}_{n\ell}(p; \sqrt{2}b) \tilde{R}_{n'\ell'}(p'; \sqrt{2}b)\, \langle p\ell sjtm_t | V_{12} | p'\ell' sjtm_t\rangle\,.\end{aligned} \tag{A.71}$$

The fact that there is a sign difference between the two momenta is not an issue, since all forces we deal with conserve parity, i.e., $\langle \boldsymbol{p}|V|\boldsymbol{p}'\rangle = \langle -\boldsymbol{p}|V|-\boldsymbol{p}'\rangle$. The rescaling of the potential matrix elements can be derived by examining

$$\langle \boldsymbol{p}_1, \boldsymbol{p}_2 | V_{12} | \boldsymbol{p}_1', \boldsymbol{p}_2'\rangle \tag{A.72}$$

in both sets of relative coordinates, where the scale factor $\sqrt{2}^3$ appears.

In the convention that we use for the potential matrix elements, an extra factor of $i^{\ell-\ell'}$ is included, and thus the final relation reads

$$\begin{aligned}&\langle n\ell sjtm_t|\, V_{12}\, |n'\ell' s' jtm_t\rangle \\ &= \int_0^\infty dp' p'^2 \int_0^\infty dp p^2 \tilde{R}_{n\ell}(p; \sqrt{2}b) \tilde{R}_{n'\ell'}(p'; \sqrt{2}b)\, \langle p\ell sjtm_t | V_{12} | p'\ell' sjtm_t\rangle\,.\end{aligned} \tag{A.73}$$